

Dynamical Criticality and Griffiths Phases in Models of Large Connectomes

Géza Ódor, Shengfeng Deng, Istvan Papp, EK-MFA, Budapest
Gustavo Deco Barcelona UPF, Jeffrey Kelling Dresden HZDR

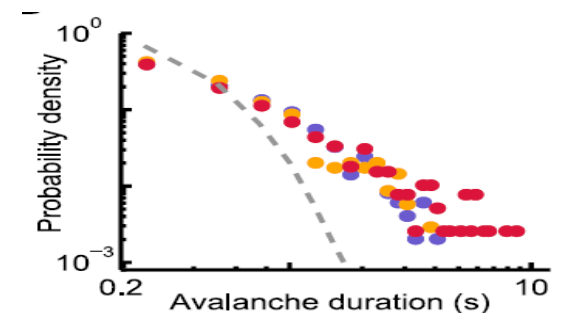


Dynamical Criticality and Griffiths Phases in Models of Large Connectomes

Géza Ódor, Shengfeng Deng, Istvan Papp, EK-MFA, Budapest
Gustavo Deco Barcelona UPF, Jeffrey Kelling Dresden HZDR



Theoretical research and experiments suggest that the brain operates at or near a **critical state** between sustained activity and an inactive phase, exhibiting optimal computational properties (see: *Beggs & Plenz J. Neurosci. 2003; Chialvo Nat. Phys. 2010; Haimovici et al. PRL 2013*)



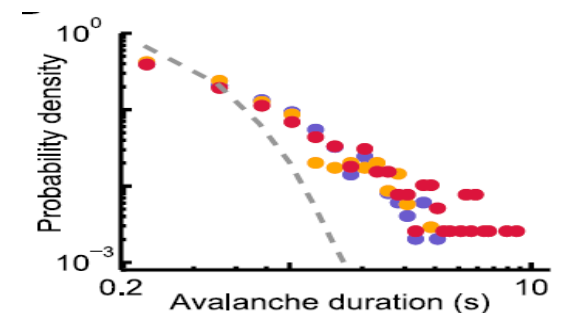
Dynamical Criticality and Griffiths Phases in Models of Large Connectomes

Géza Ódor, Shengfeng Deng, Istvan Papp, EK-MFA, Budapest
Gustavo Deco Barcelona UPF, Jeffrey Kelling Dresden HZDR



Theoretical research and experiments suggest that the brain operates at or near a **critical state** between sustained activity and an inactive phase, exhibiting optimal computational properties (see: *Beggs & Plenz J. Neurosci. 2003; Chialvo Nat. Phys. 2010; Haimovici et al. PRL 2013*)

Neurons exhibit oscillatory behavior



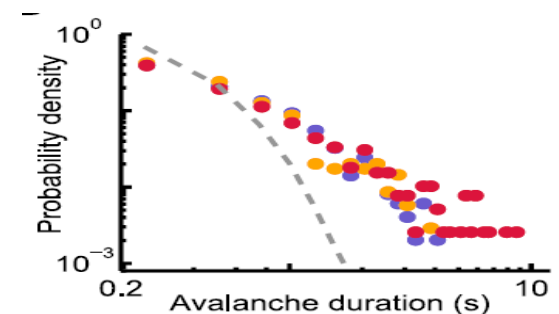
Dynamical Criticality and Griffiths Phases in Models of Large Connectomes

Géza Ódor, Shengfeng Deng, Istvan Papp, EK-MFA, Budapest
Gustavo Deco Barcelona UPF, Jeffrey Kelling Dresden HZDR



Theoretical research and experiments suggest that the brain operates at or near a **critical state** between sustained activity and an inactive phase, exhibiting optimal computational properties (see: *Beggs & Plenz J. Neurosci. 2003; Chialvo Nat. Phys. 2010; Haimovici et al. PRL 2013*)

Neurons exhibit oscillatory behavior
Quasistatic inhomogeneity causes dynamical criticality in Griffiths phases



Dynamical Criticality and Griffiths Phases in Models of Large Connectomes

Géza Ódor, Shengfeng Deng, Istvan Papp, EK-MFA, Budapest
Gustavo Deco Barcelona UPF, Jeffrey Kelling Dresden HZDR

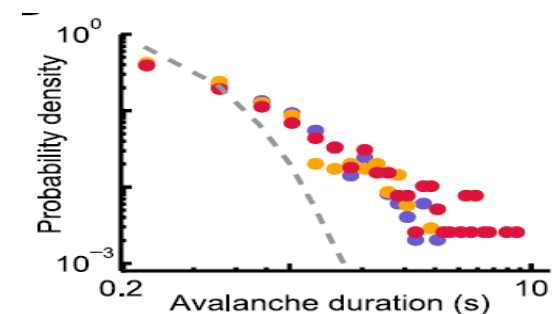


Theoretical research and experiments suggest that the brain operates at or near a **critical state** between sustained activity and an inactive phase, exhibiting optimal computational properties (see: *Beggs & Plenz J. Neurosci. 2003; Chialvo Nat. Phys. 2010; Haimovici et al. PRL 2013*)

Neurons exhibit oscillatory behavior

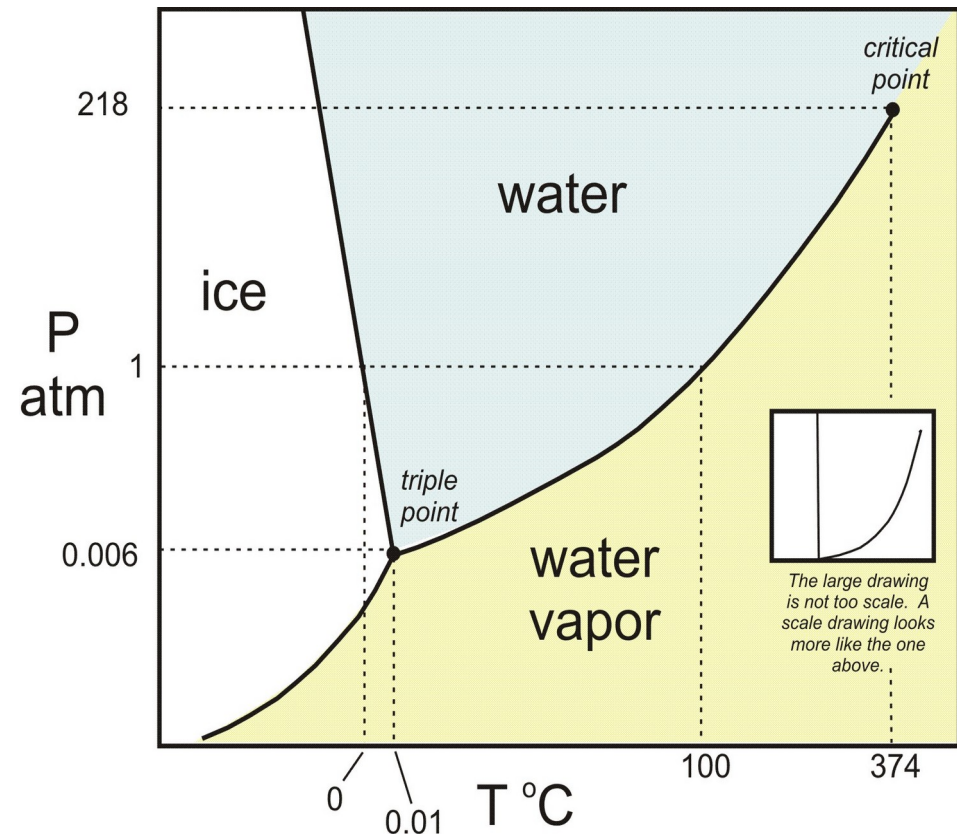
Quasistatic inhomogeneity causes dynamical criticality in Griffiths phases

→ Edge of Synchronization and Griffiths phase in brain models ?

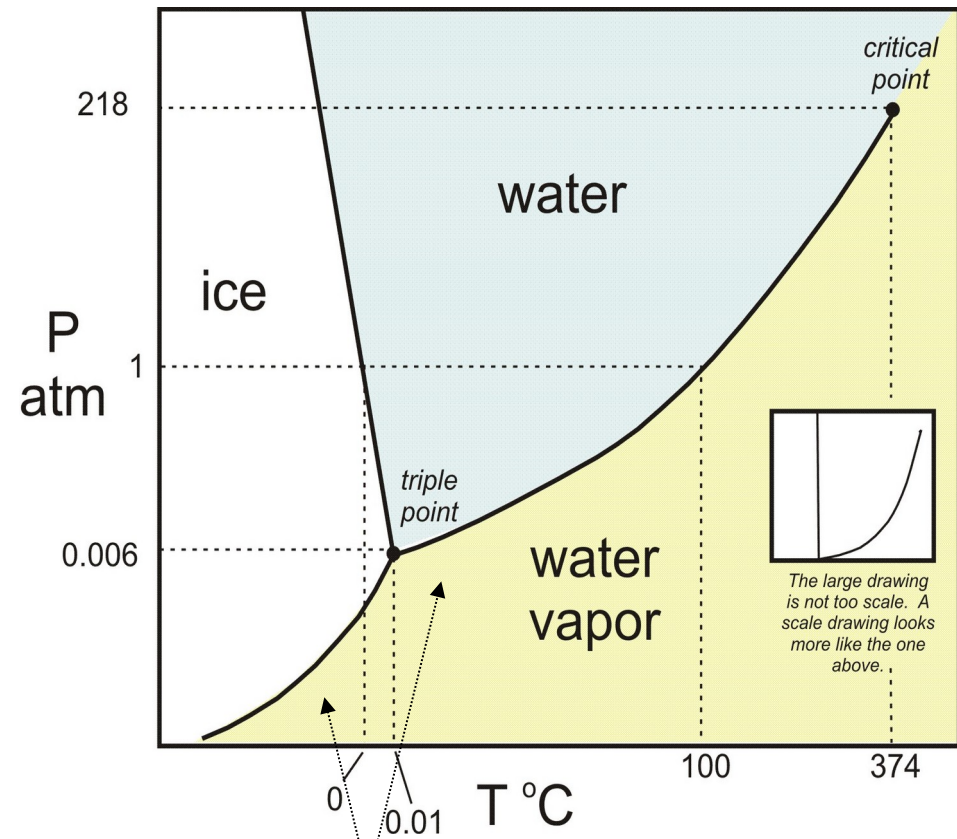


Phase transitions and criticality

Phase transitions and criticality



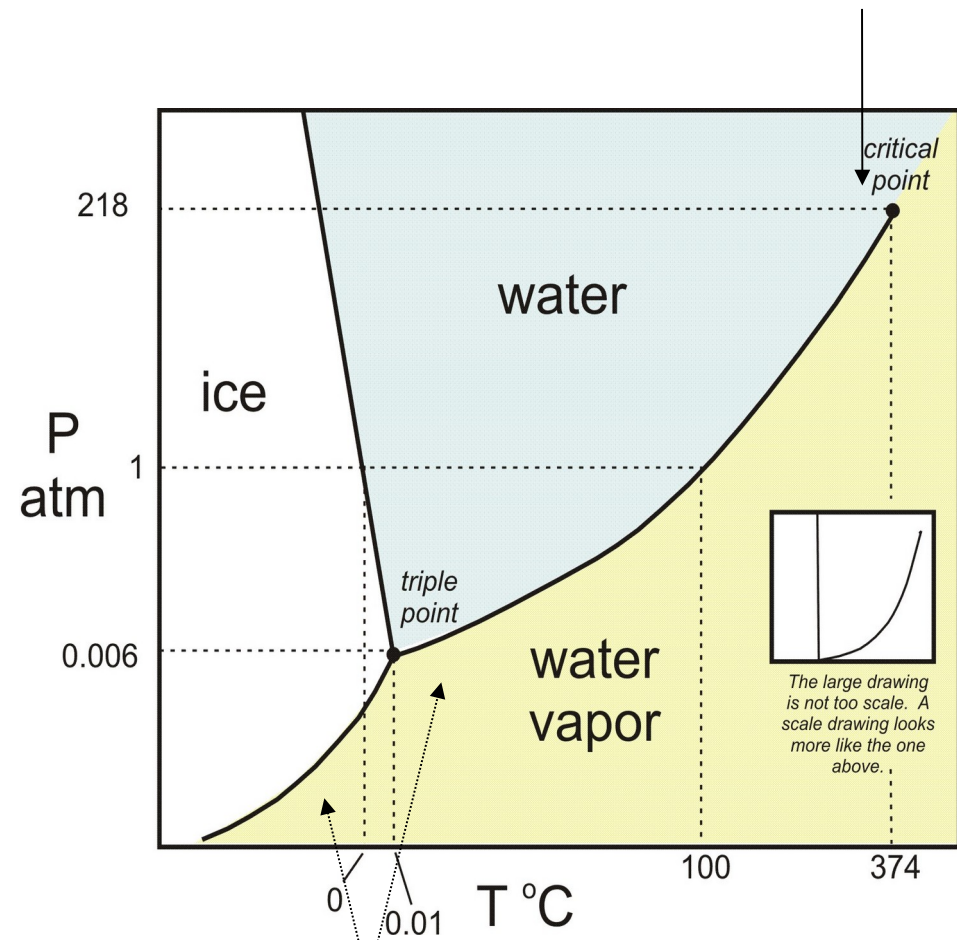
Phase transitions and criticality



First order transitions

Phase transitions and criticality

Second order, continuous transition

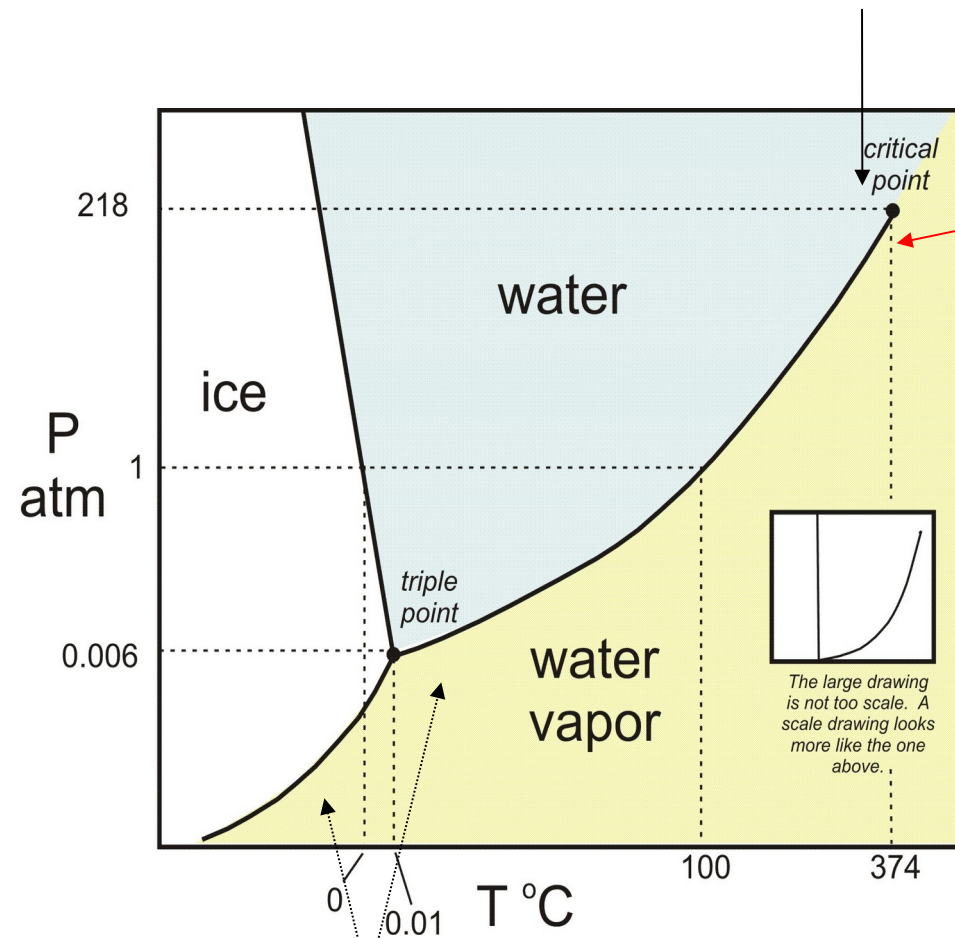


First order transitions

Phase transitions and criticality

Second order, continuous transition

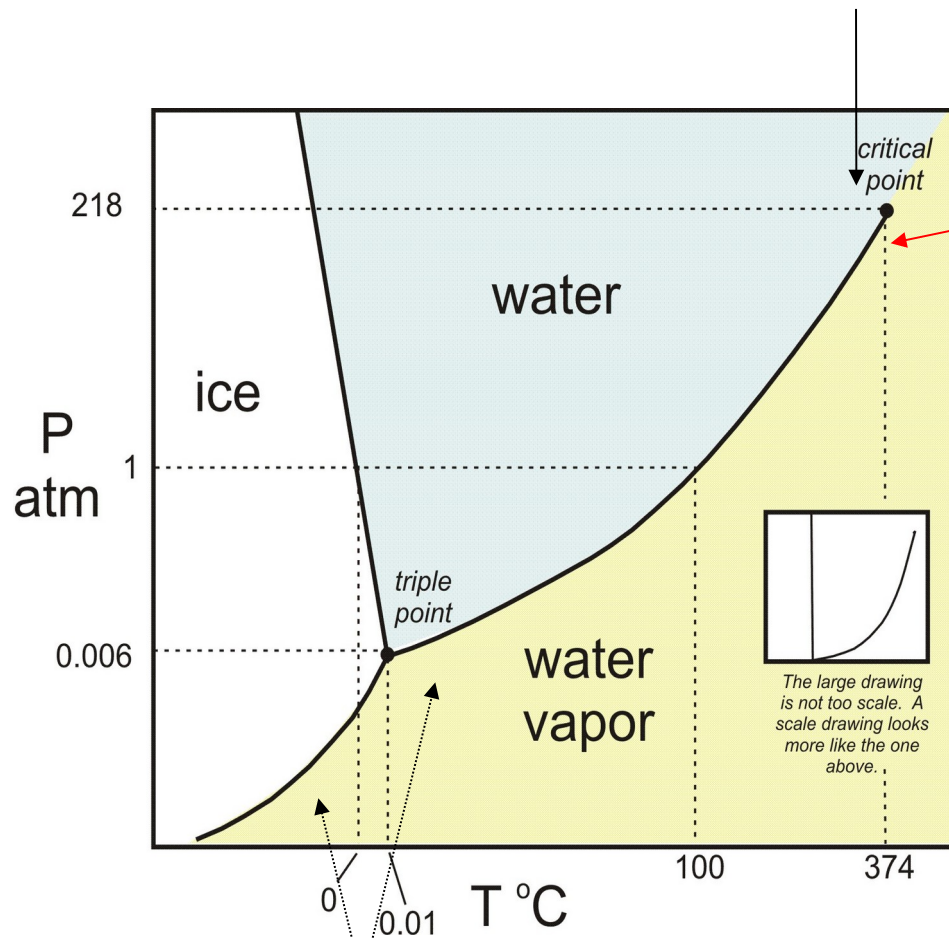
At the critical point:
Strong fluctuations



First order transitions

Phase transitions and criticality

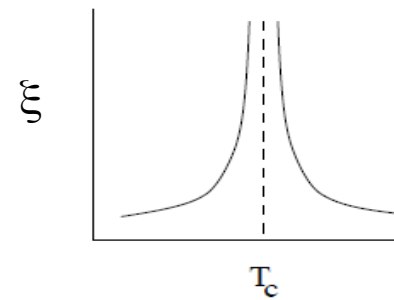
Second order, continuous transition



At the critical point:

Strong fluctuations

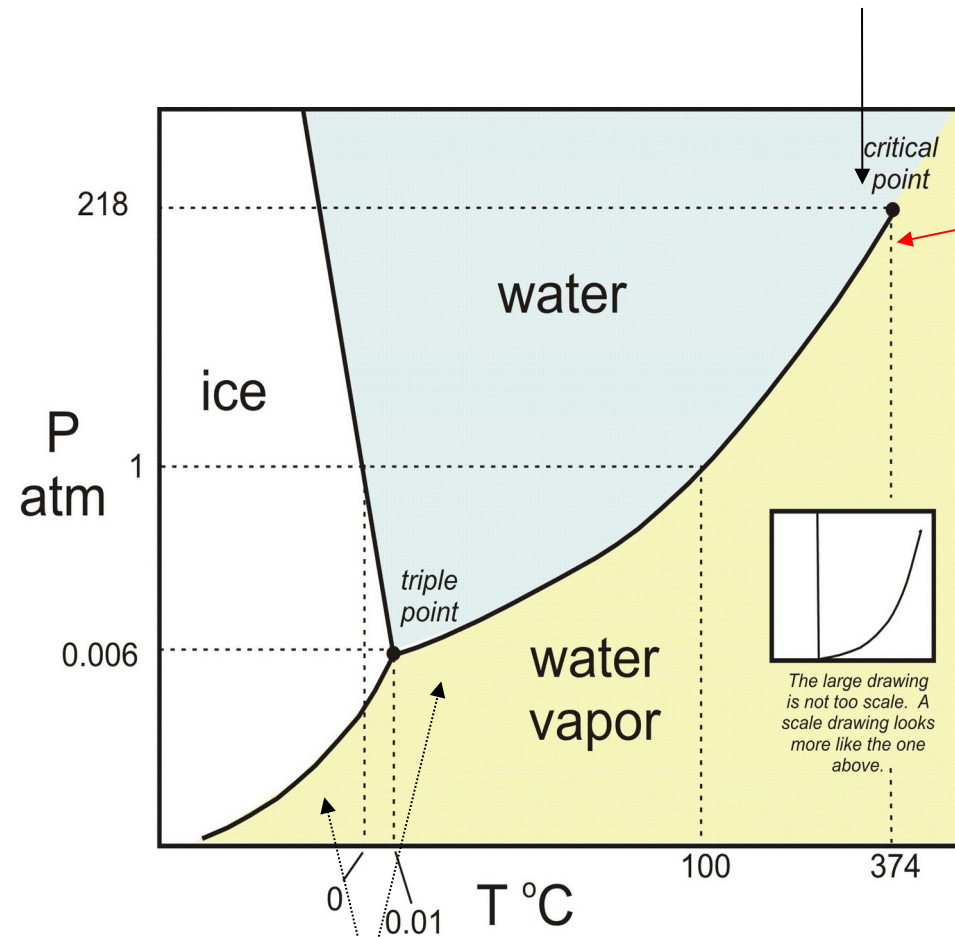
Diverging correlations:



First order transitions

Phase transitions and criticality

Second order, continuous transition

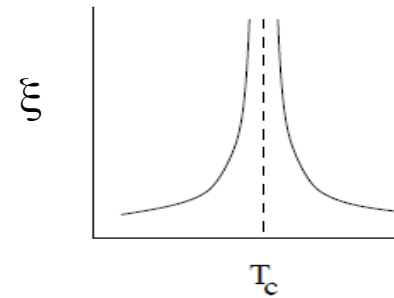


First order transitions

At the critical point:

Strong fluctuations

Diverging correlations:

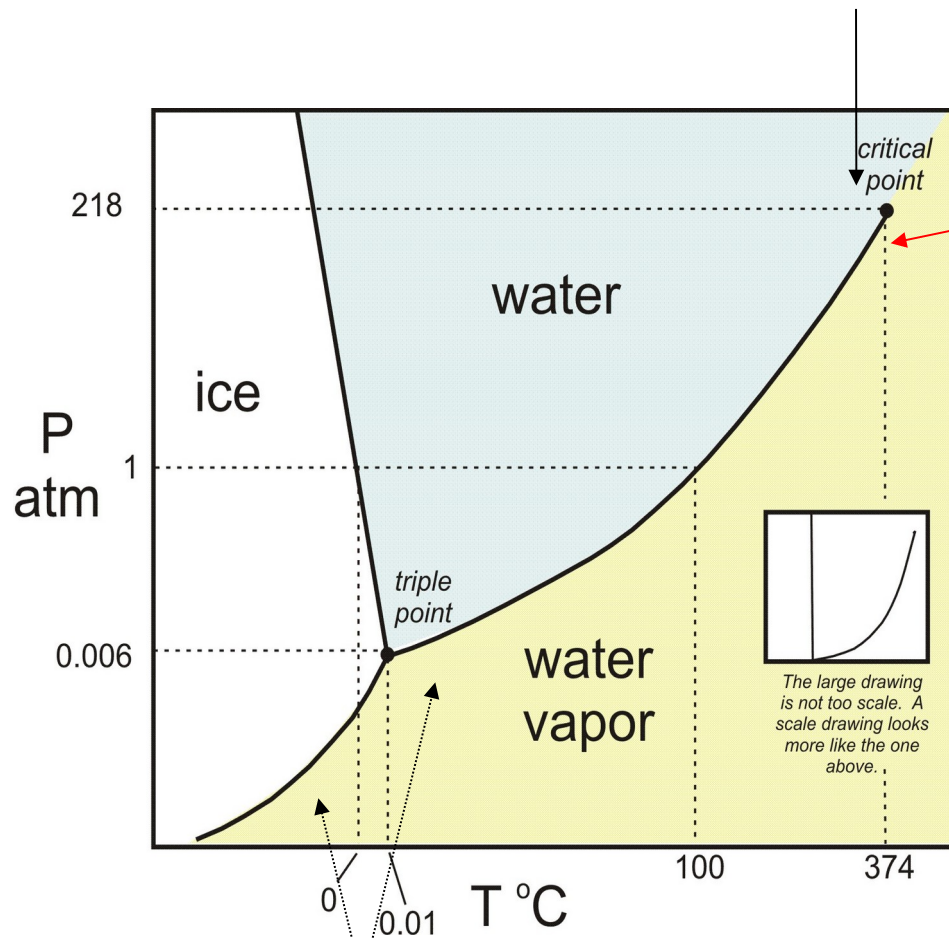


Rescaling invariance
(scale-free behavior):

$$r \rightarrow br, \quad F(r, t, \dots) \rightarrow a^x F(br, b^z t, \dots)$$

Phase transitions and criticality

Second order, continuous transition



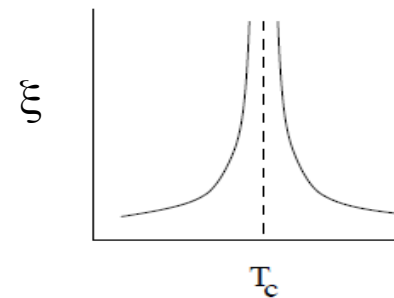
First order transitions

$$C_{\pm} = \frac{\partial E}{\partial T} \propto |t|^{\alpha_{\pm}}$$

At the critical point:

Strong fluctuations

Diverging correlations:



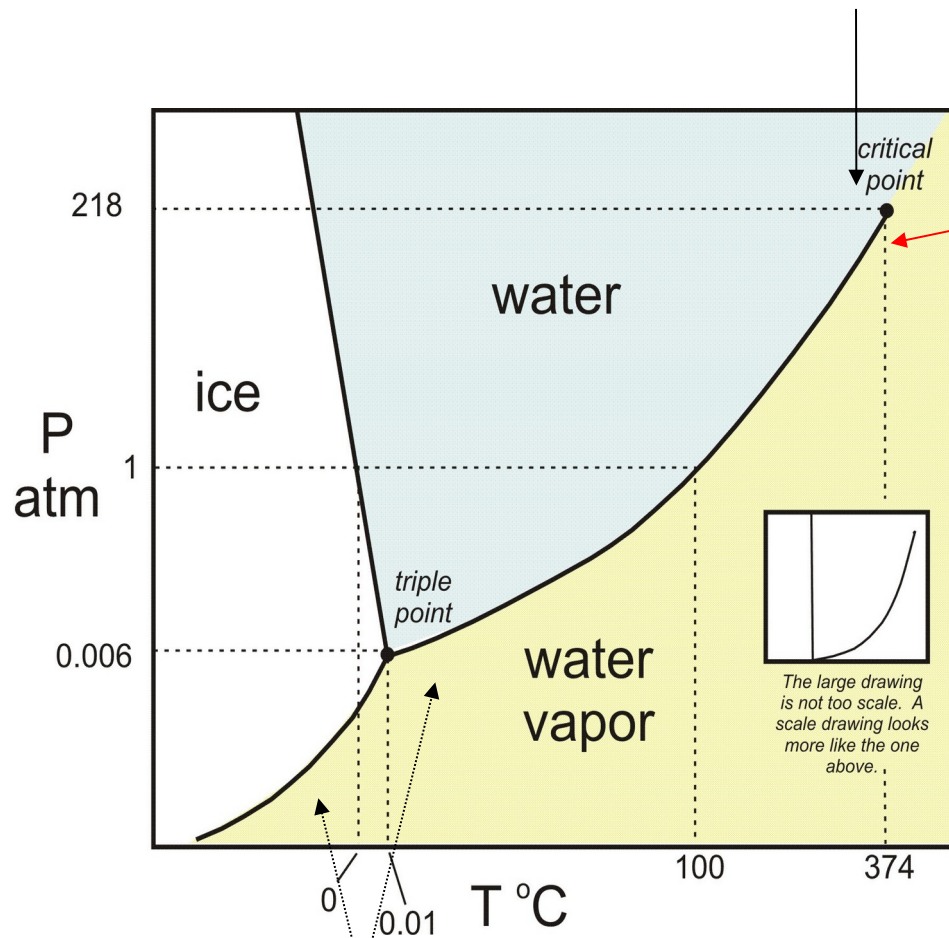
Rescaling invariance
(scale-free behavior):

$$r \rightarrow br, \quad F(r, t, \dots) \rightarrow a^x F(br, b^z t, \dots)$$

Power-laws: i.e. specific heat:

Phase transitions and criticality

Second order, continuous transition



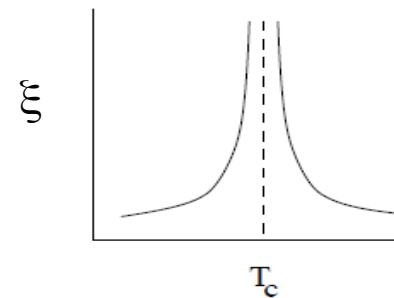
First order transitions

$$C_{\pm} = \frac{\partial E}{\partial T} \propto |t|^{\alpha_{\pm}}$$

At the critical point:

Strong fluctuations

Diverging correlations:



Rescaling invariance
(scale-free behavior):

$$r \rightarrow br, \quad F(r, t, \dots) \rightarrow a^x F(br, b^z t, \dots)$$

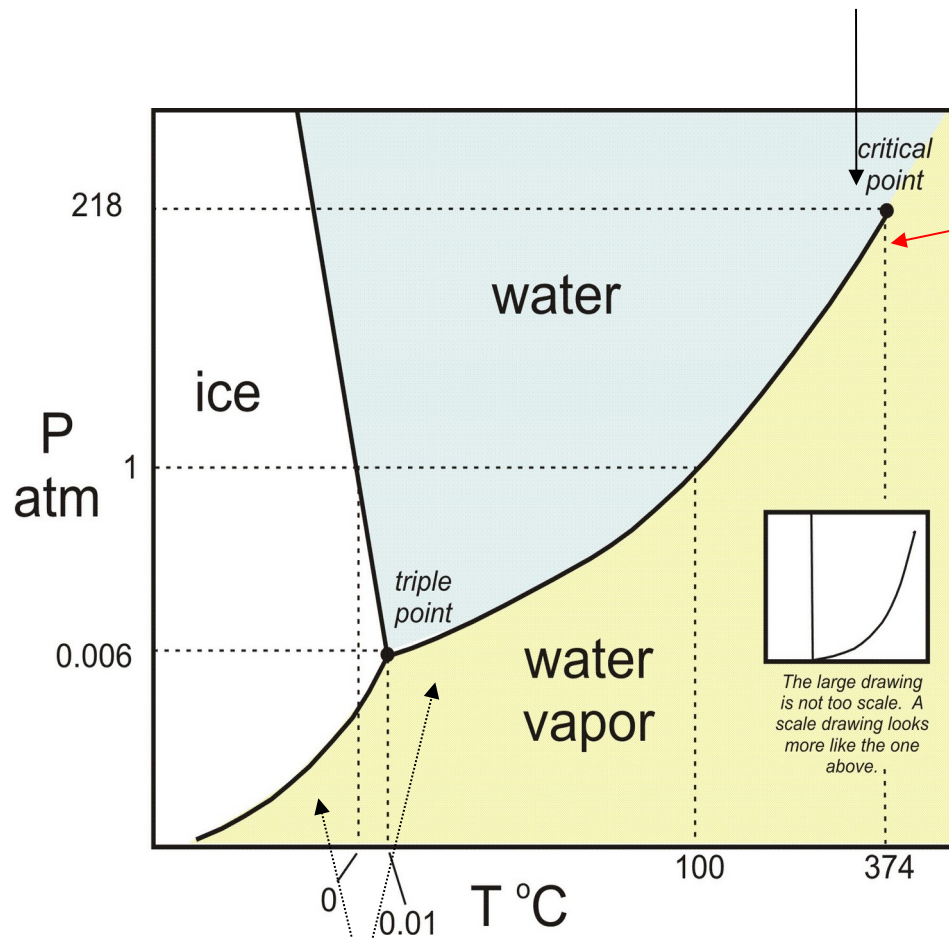
Power-laws: i.e. specific heat:

$$\chi_{\pm}(T, H \rightarrow 0^+) = \left. \frac{\partial m}{\partial H} \right|_{H=0^+} \propto |t|^{-\gamma_{\pm}}$$

susceptibility, autocorrelation ...

Phase transitions and criticality

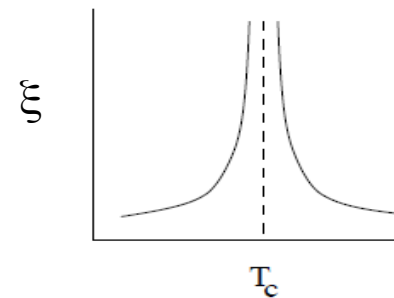
Second order, continuous transition



At the critical point:

Strong fluctuations

Diverging correlations:



Rescaling invariance
(scale-free behavior):

$$r \rightarrow br, \quad F(r, t, \dots) \rightarrow a^x F(br, b^z t, \dots)$$

Power-laws: i.e. specific heat:

$$C_{\pm} = \frac{\partial E}{\partial T} \propto |t|^{\alpha_{\pm}}$$

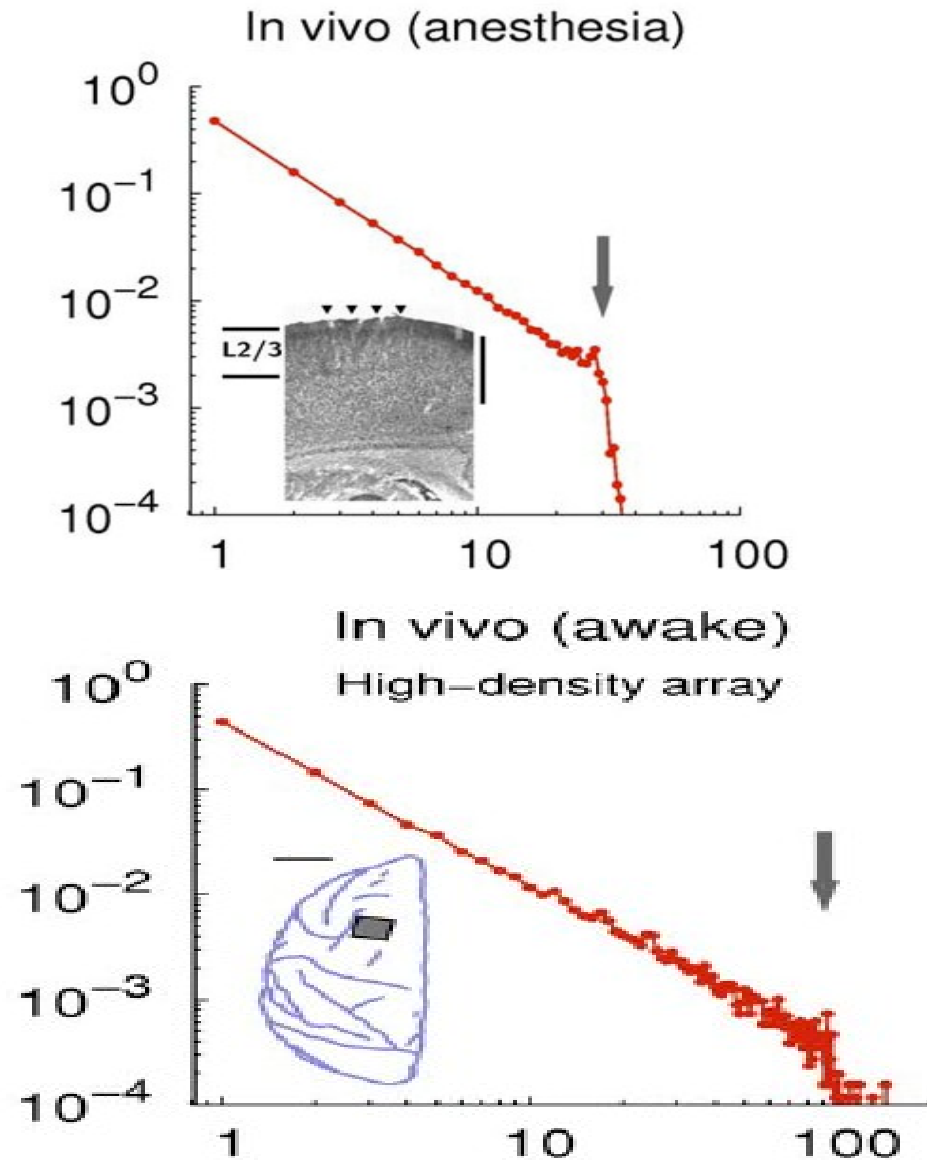
$$\chi_{\pm}(T, H \rightarrow 0^+) = \left. \frac{\partial m}{\partial H} \right|_{H=0^+} \propto |t|^{-\gamma_{\pm}}$$

susceptibility, autocorrelation ...

First order transitions

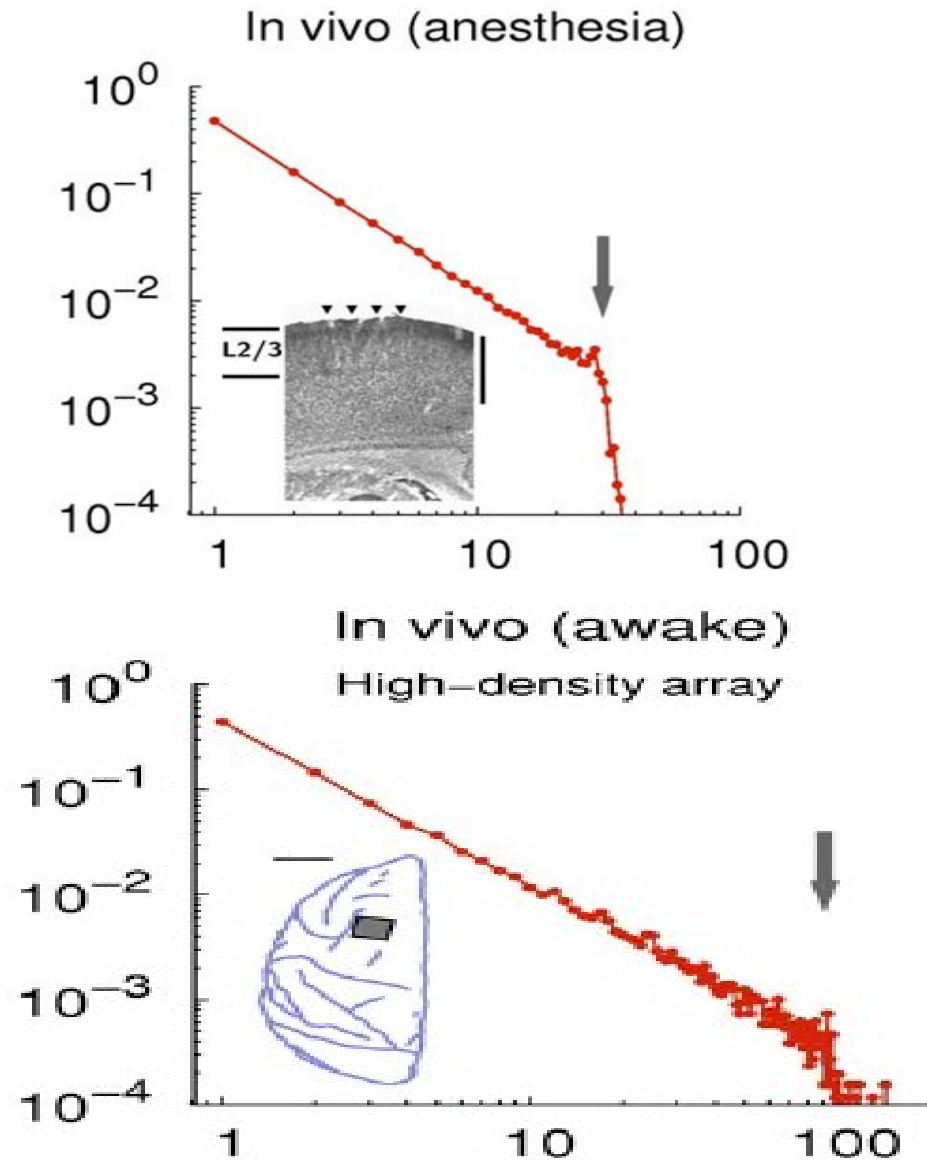
Universality!
Mean-field for $d \rightarrow \infty$

Brain experiments suggest near critical behavior



Brain experiments suggest near critical behavior

Electrode LFP experiments
Since Beggs and Plenz 2003
For humans and animals



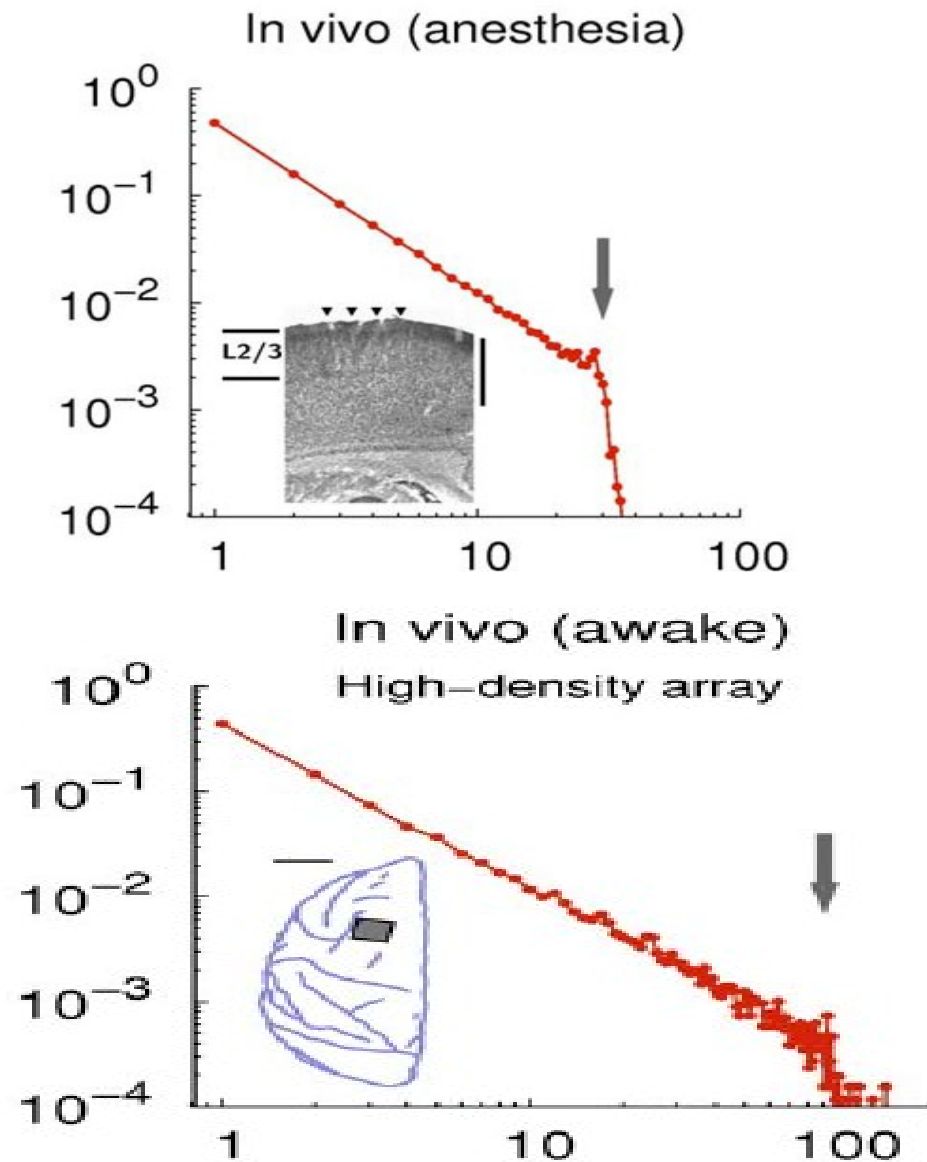
Brain experiments suggest near critical behavior

Electrode LFP experiments

Since Beggs and Plenz 2003

For humans and animals

In vitro, for balanced
excitatory/inhibitory states



Brain experiments suggest near critical behavior

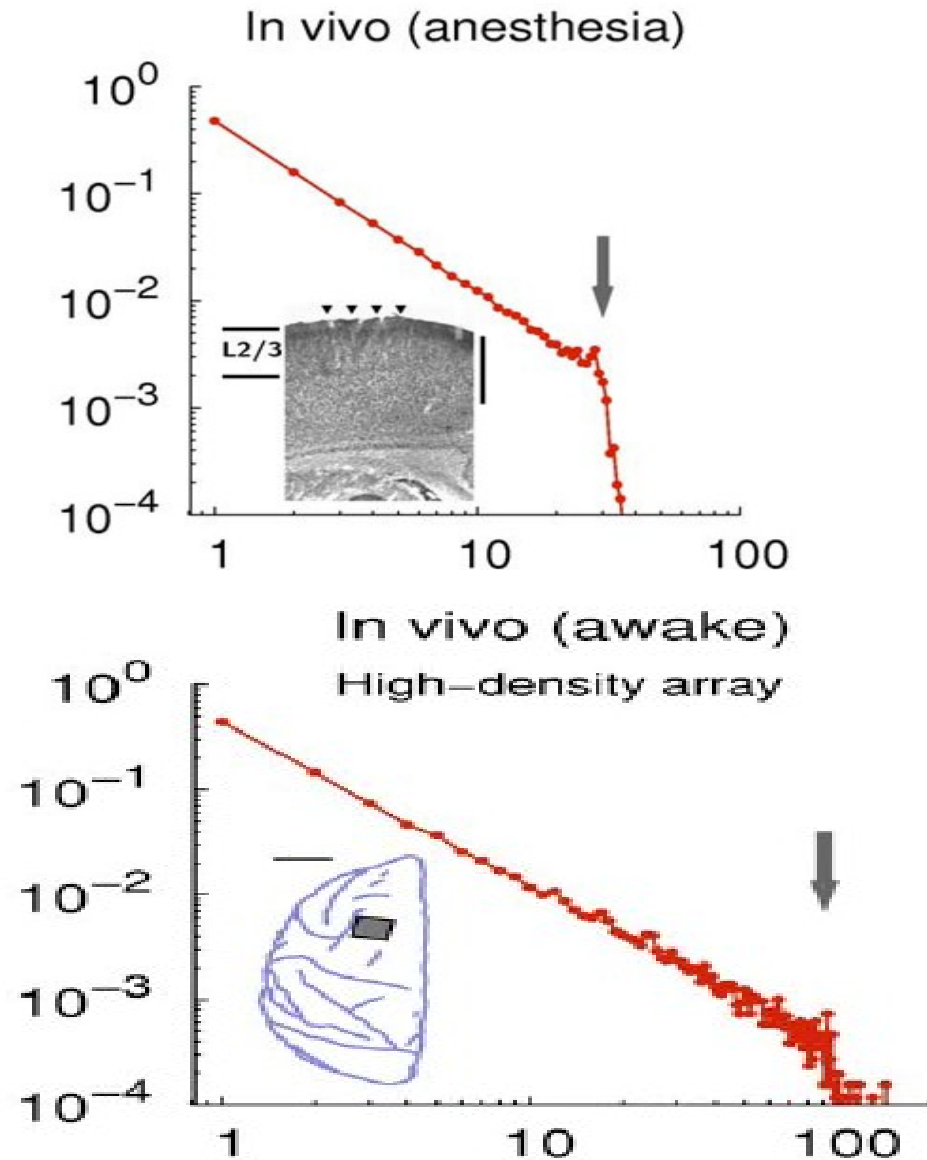
Electrode LFP experiments

Since Beggs and Plenz 2003

For humans and animals

In vitro, for balanced
excitatory/inhibitory states

Other experiments: fMRI, BOLD,



Brain experiments suggest near critical behavior

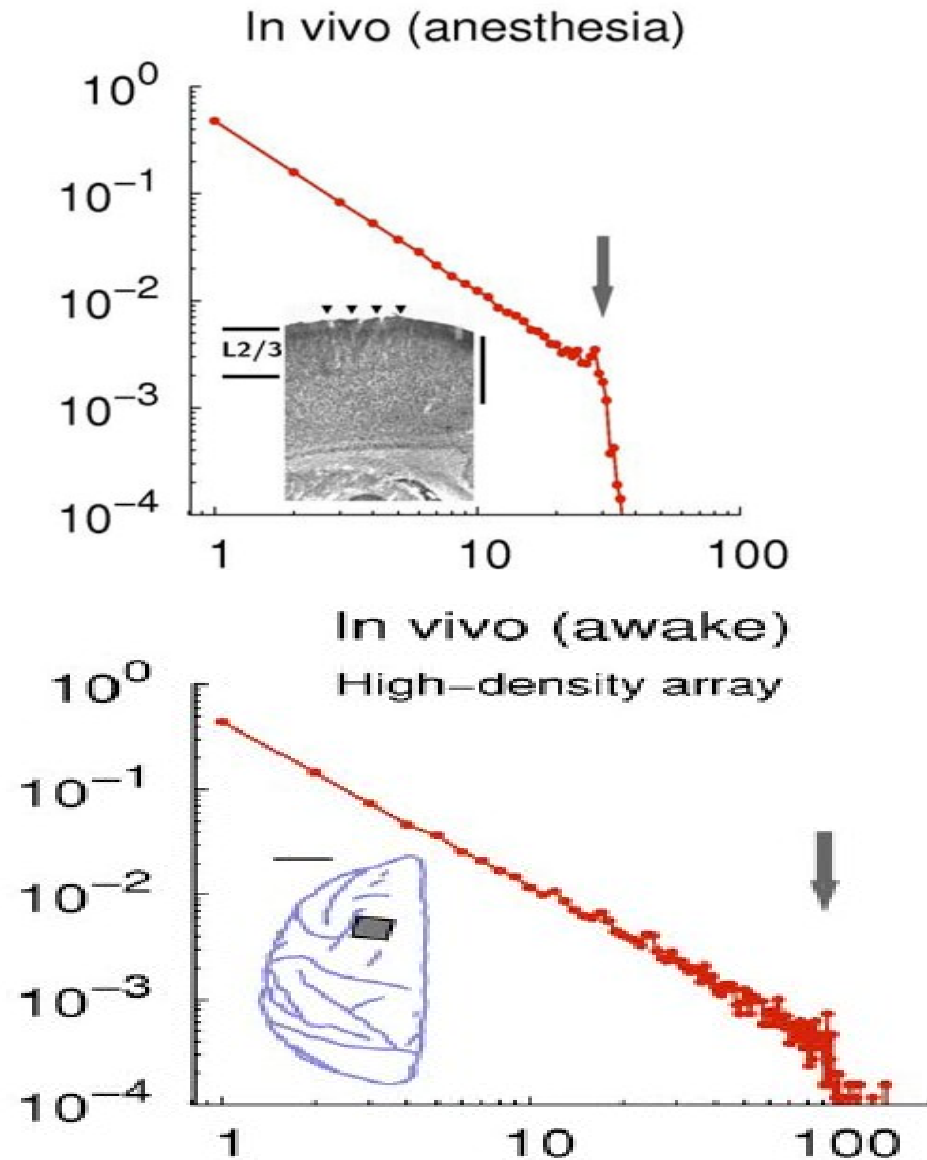
Electrode LFP experiments

Since Beggs and Plenz 2003

For humans and animals

In vitro, for balanced
excitatory/inhibitory states

Other experiments: fMRI, BOLD,
Voltage imaging, calcium imaging,
MEG, EEG, **Long-Range Temporal
Correlations (LRTC)**.



Brain experiments suggest near critical behavior

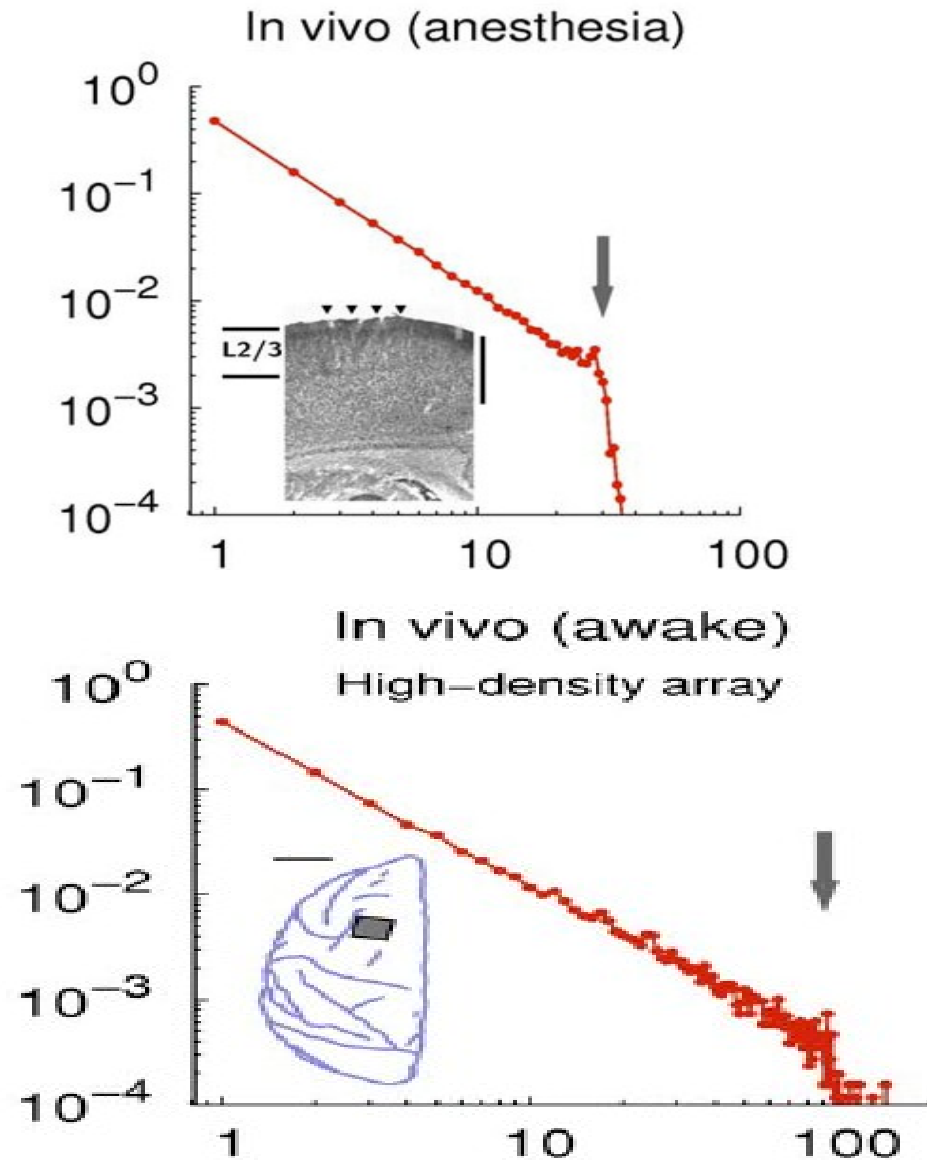
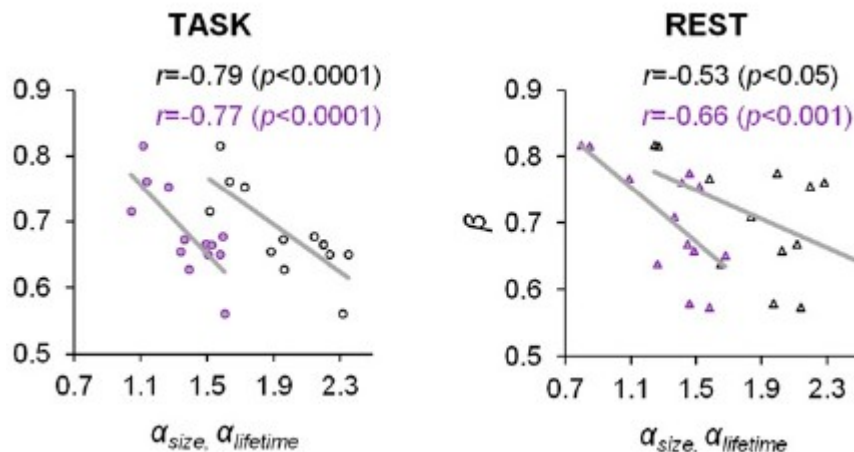
Electrode LFP experiments

Since Beggs and Plenz 2003

For humans and animals

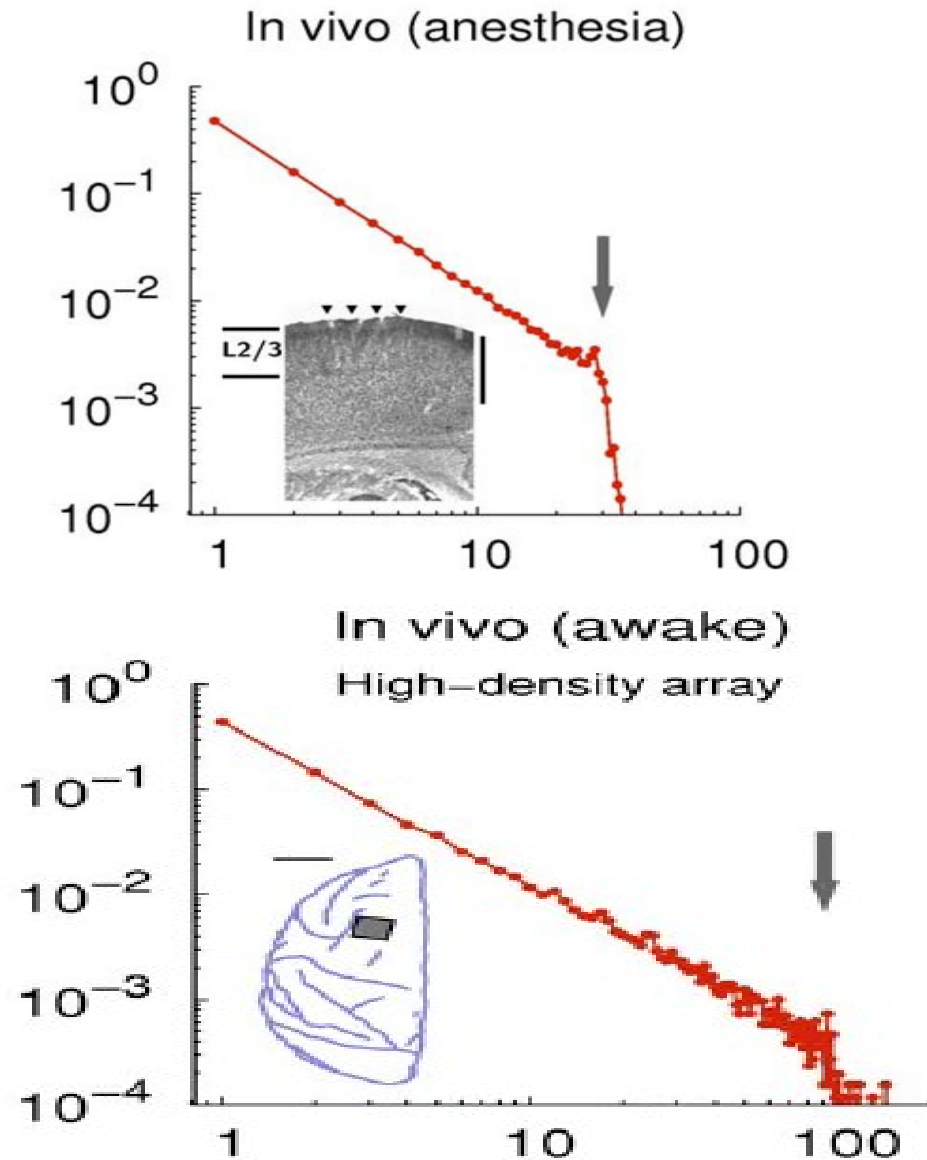
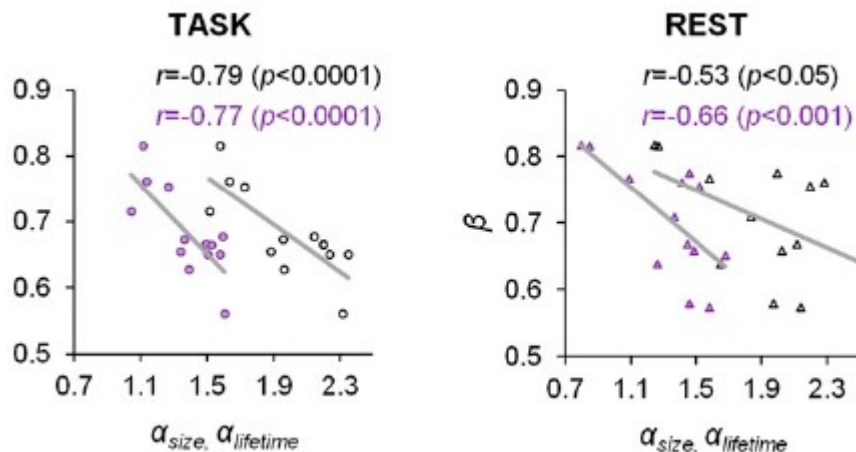
In vitro, for balanced
excitatory/inhibitory states

Other experiments: fMRI, BOLD,
Voltage imaging, calcium imaging,
MEG, EEG, **Long-Range Temporal
Correlations (LRTC)**.



Brain experiments suggest near critical behavior

Electrode LFP experiments
 Since Beggs and Plenz 2003
 For humans and animals
 In vitro, for balanced
 excitatory/inhibitory states
 Other experiments: fMRI, BOLD,
 Voltage imaging, calcium imaging,
 MEG, EEG, **Long-Range Temporal**
Correlations (LRTC).



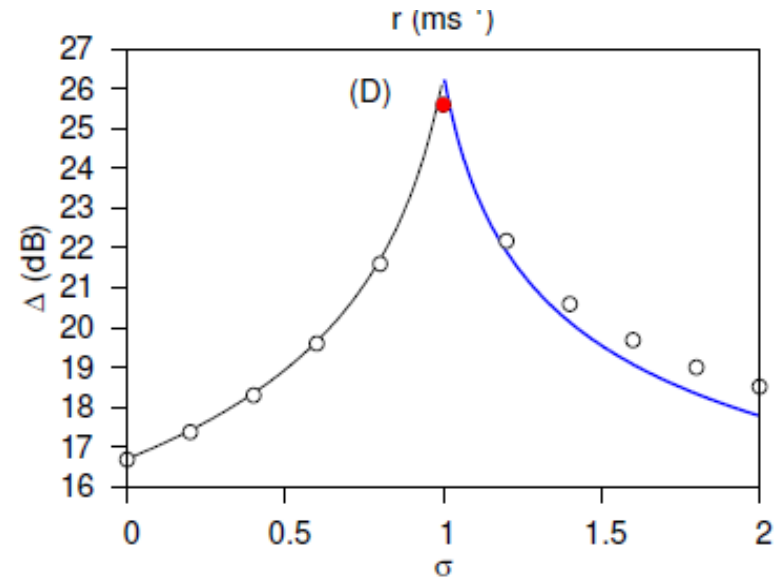
Nonuniversal critical exponents or
 Mean-field values : $\tau = 1.5$ $\tau_t = 2$?

Why would the brain be critical ?

Why would the brain be critical ?

Pros:

Diverging fluctuations →
High sensitivity to stimuli

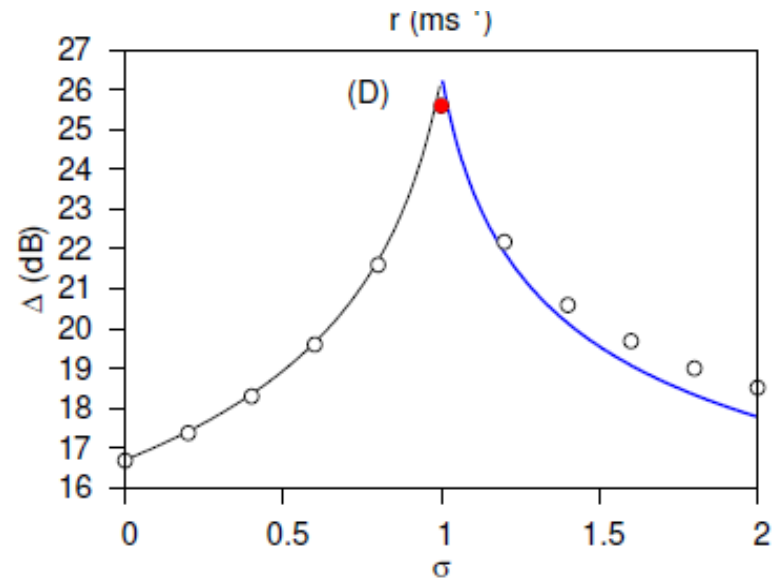


Why would the brain be critical ?

Pros:

Diverging fluctuations →
High sensitivity to stimuli

Diverging correlation functions →
Optimal transmission and
storage of information



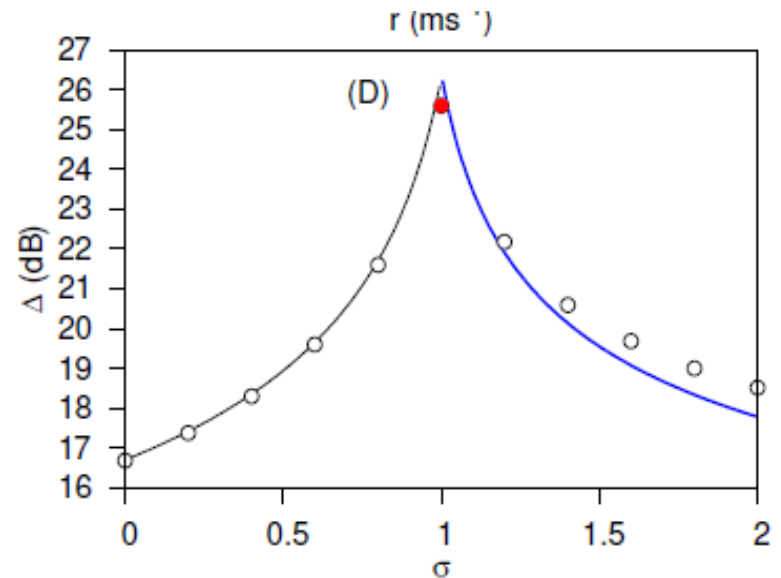
Why would the brain be critical ?

Pros:

Diverging fluctuations →
High sensitivity to stimuli

Diverging correlation functions →
Optimal transmission and
storage of information

Maximal information processing and computational
performance



Why would the brain be critical ?

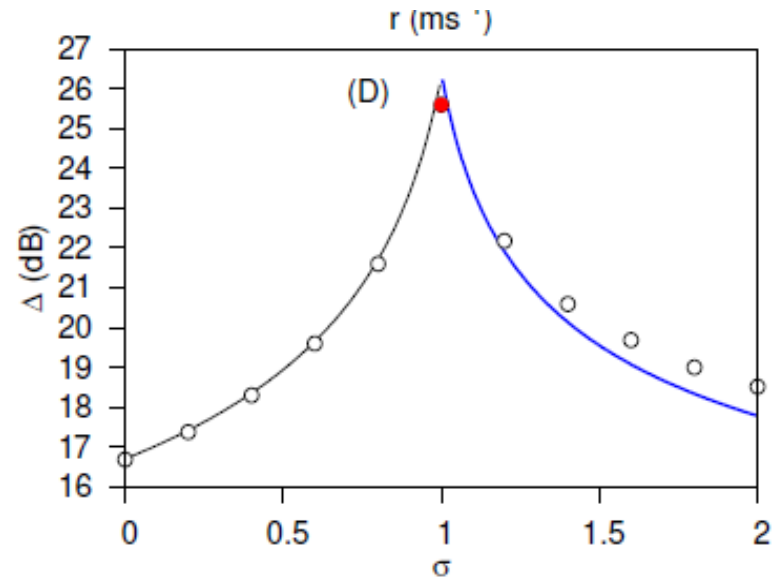
Pros:

Diverging fluctuations →
High sensitivity to stimuli

Diverging correlation functions →
Optimal transmission and
storage of information

Maximal information processing and computational performance

Cons: Tuning to critical point is needed
Danger of super-critical (epileptic) behavior



Why would the brain be critical ?

Pros:

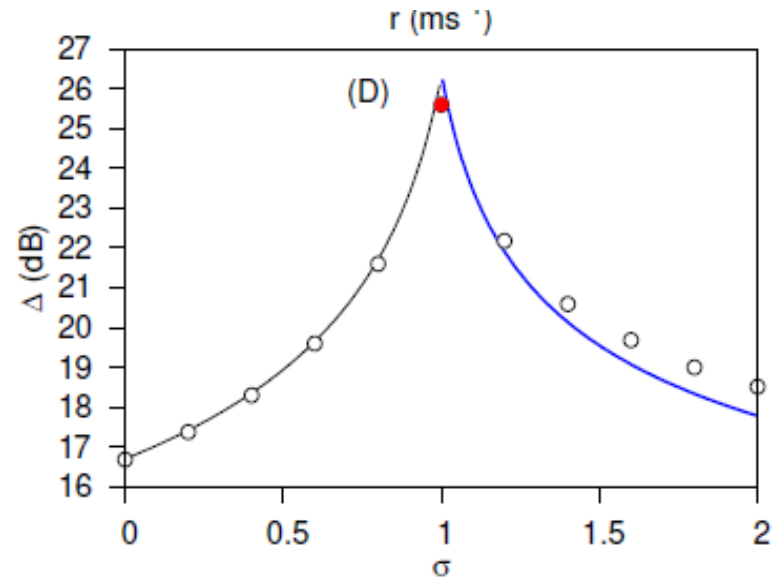
Diverging fluctuations →
High sensitivity to stimuli

Diverging correlation functions →
Optimal transmission and
storage of information

Maximal information processing and computational performance

Cons: Tuning to critical point is needed
Danger of super-critical (epileptic) behavior

Self-organization to criticality (SOC) ?



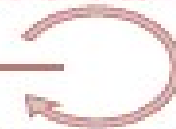
Explanations for tuning to criticality

(B)

No activity
Order
— Criticality
Disorder
High (chaotic) activity



Self-organized criticality



Fine tuning by feedback

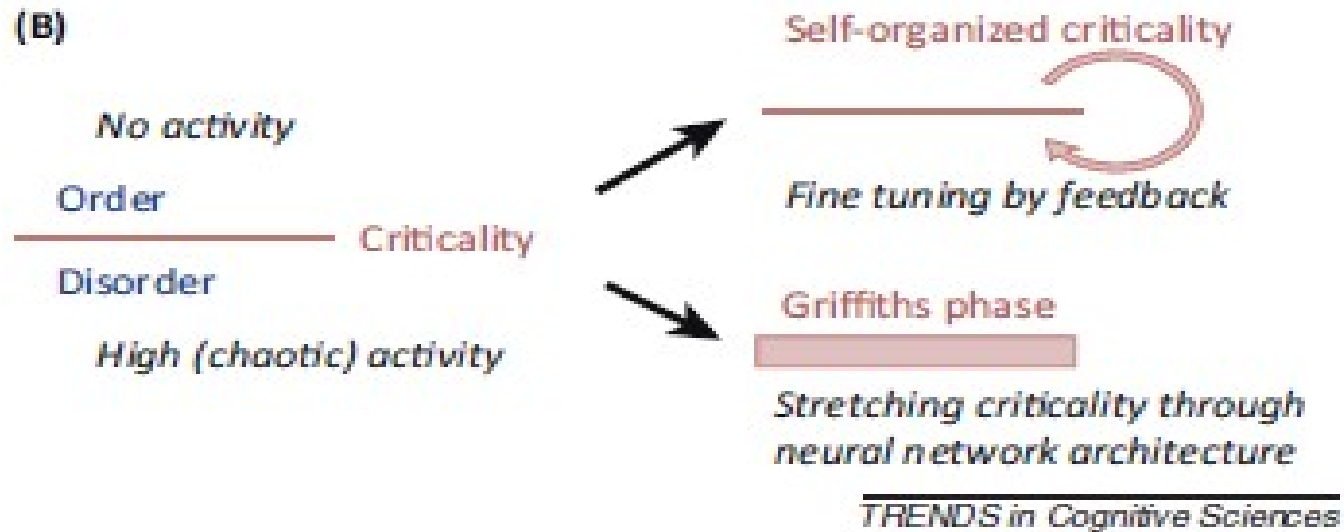
Griffiths phase



*Stretching criticality through
neural network architecture*

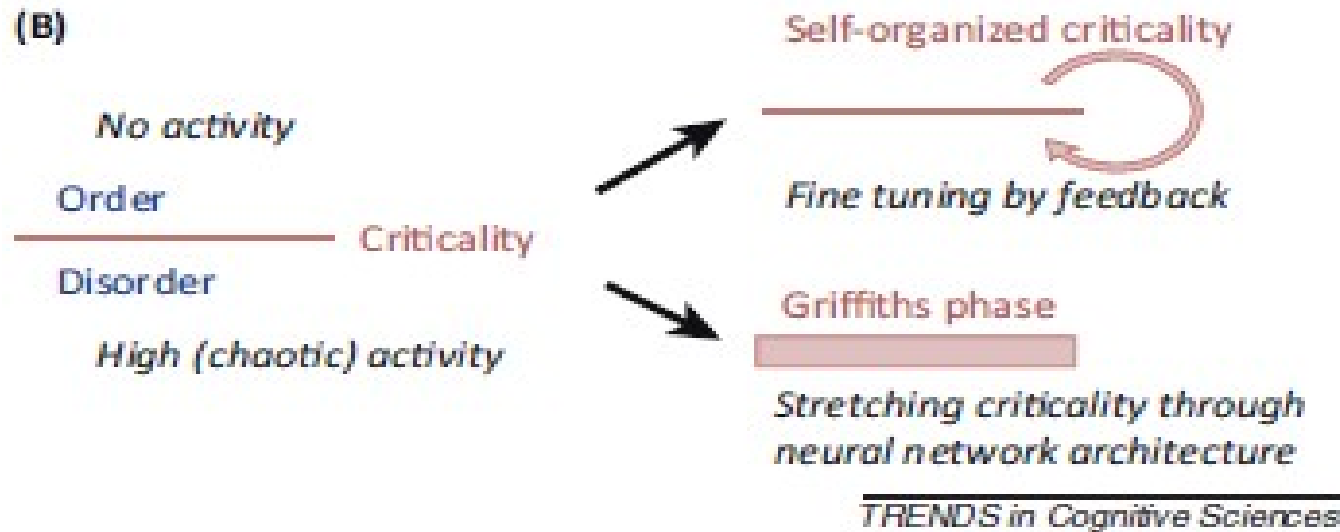
TRENDS in Cognitive Sciences

Explanations for tuning to criticality



SOC ↔ GP do not exclude each other

Explanations for tuning to criticality



SOC ↔ GP do not exclude each other

For SOC we need a responsible feedback mechanism,

GP can occur spontaneously in heterogeneous systems

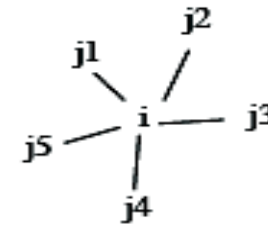
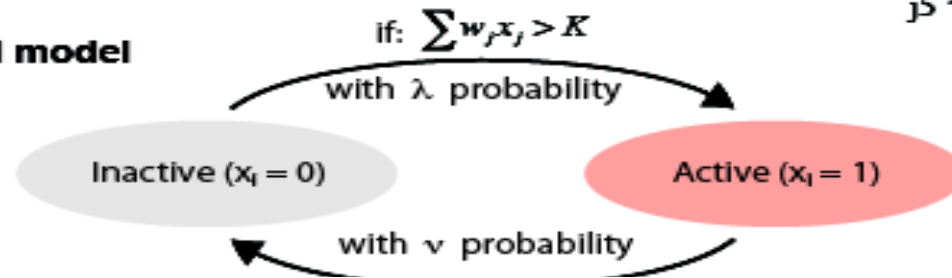
Discrete, stochastic threshold models on networks

λ

Discrete, stochastic threshold models on networks

For a node i with neighbors $\{j_1, j_2, \dots, j_k\}$

Threshold model

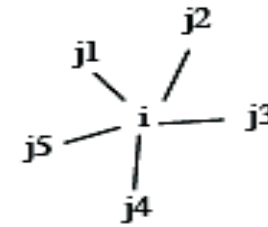
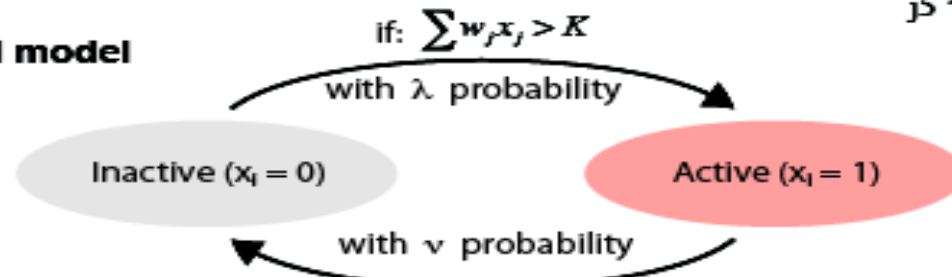


λ

Discrete, stochastic threshold models on networks

For a node i with neighbors $\{j_1, j_2, \dots, j_k\}$

Threshold model



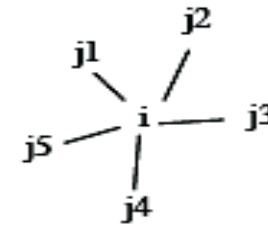
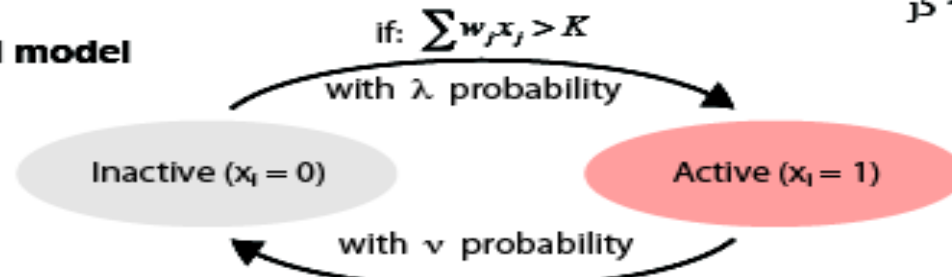
*Hastings model
Chialvo et al*

λ

Discrete, stochastic threshold models on networks

For a node i with neighbors $\{j_1, j_2, \dots, j_k\}$

Threshold model



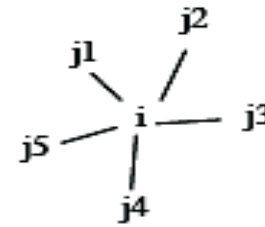
*Hastings model
Chialvo et al*

Order parameter : density of active sites (ρ)

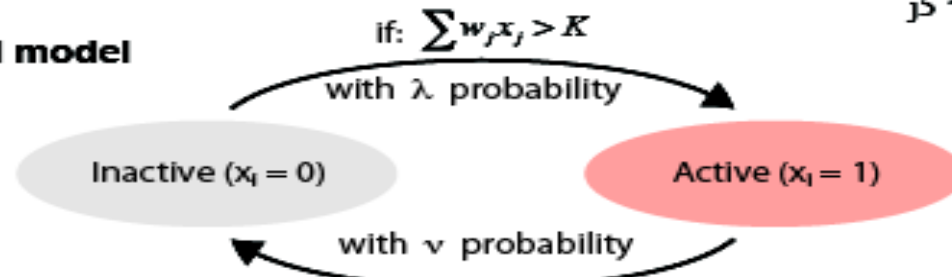
λ

Discrete, stochastic threshold models on networks

For a node i with neighbors $\{j_1, j_2, \dots, j_k\}$



Threshold model

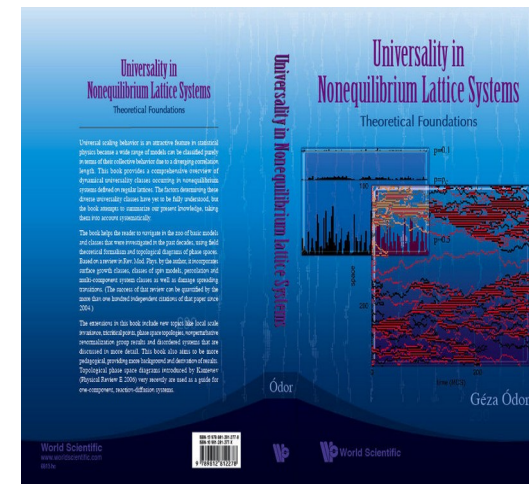


*Hastings model
Chialvo et al*

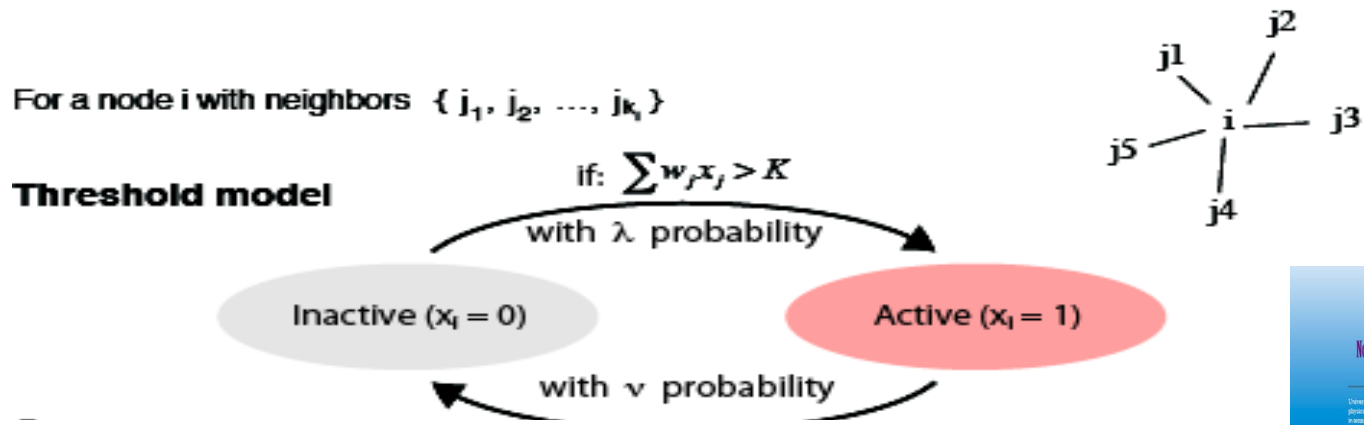
Order parameter : density of active sites (ρ)

Mean field for reaction diffusion systems : $mA \rightarrow (m+k)A, nA \rightarrow (n-l)A$

For $m > n$: first order phase transition see my book :



Discrete, stochastic threshold models on networks

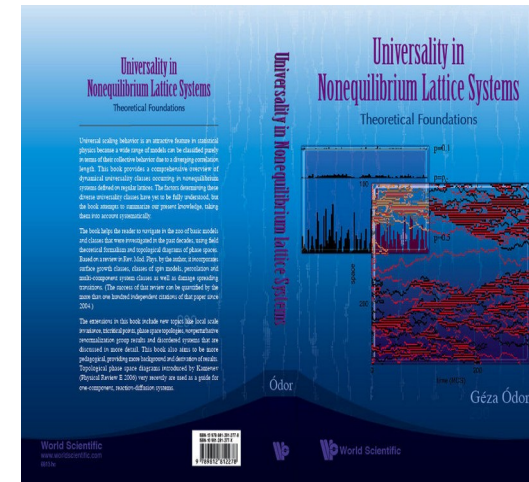


Order parameter : density of active sites (ρ)

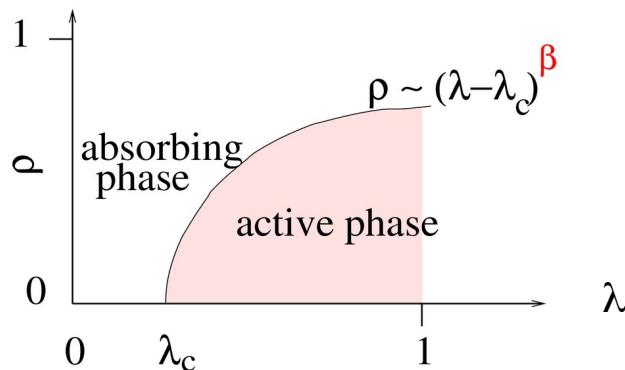
Hastings model
Chialvo et al

Mean field for reaction diffusion systems : $mA \rightarrow (m+k)A, nA \rightarrow (n-l)A$

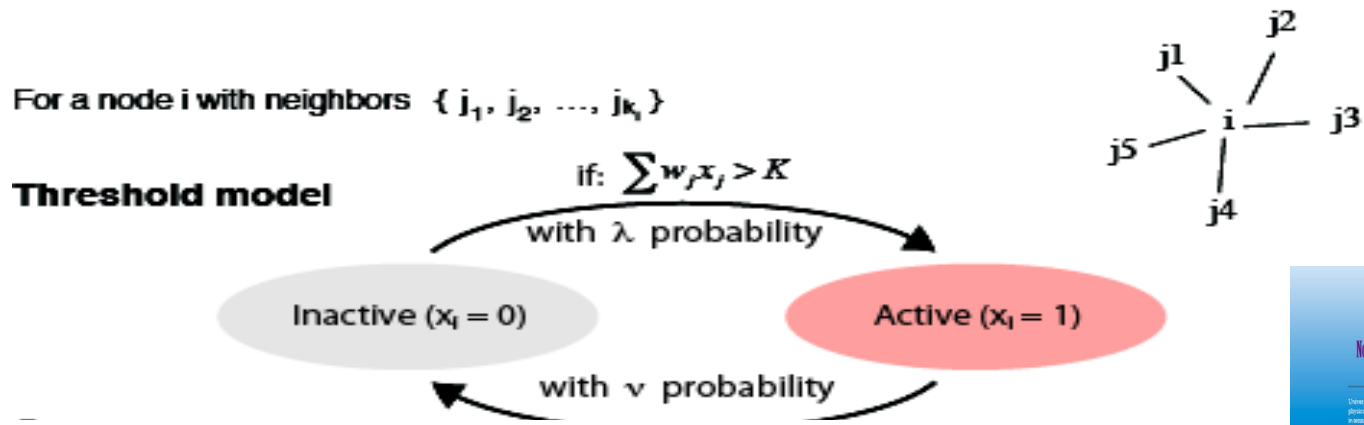
For $m > n$: first order phase transition see my book :



On low dimensional regular, Euclidean lattice: **DP** critical point : $\lambda_c > 0$ between inactive and active phases (**GÓ: PRE 67 (2003) 056114.**)



Discrete, stochastic threshold models on networks

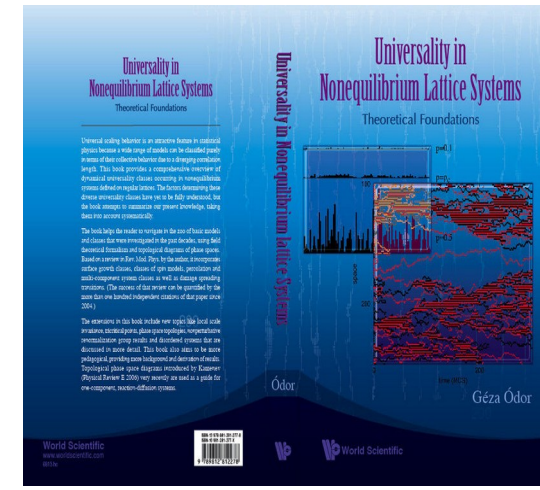


Order parameter : density of active sites (ρ)

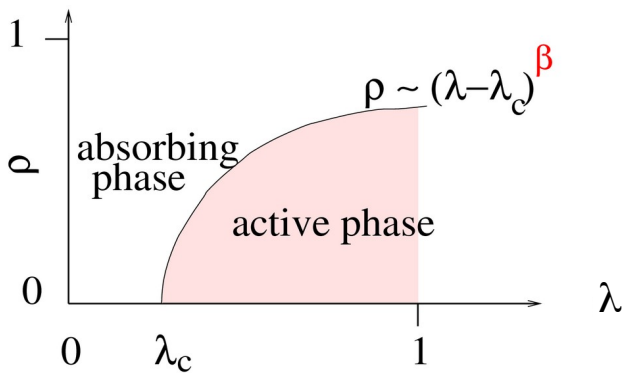
Hastings model
Chialvo et al

Mean field for reaction diffusion systems : $mA \rightarrow (m+k)A, nA \rightarrow (n-l)A$

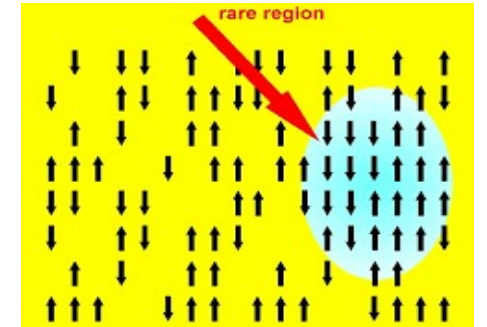
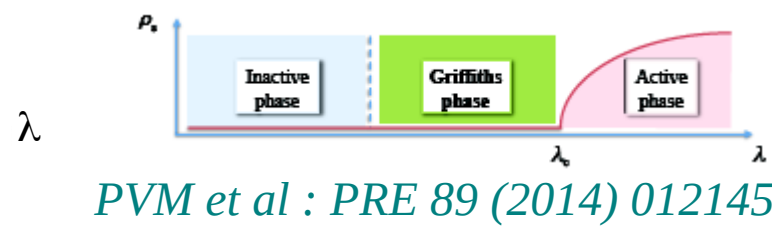
For $m > n$: first order phase transition see my book :



On low dimensional regular, Euclidean lattice: **DP** critical point : $\lambda_c > 0$ between inactive and active phases (*GÓ: PRE 67 (2003) 056114.*)



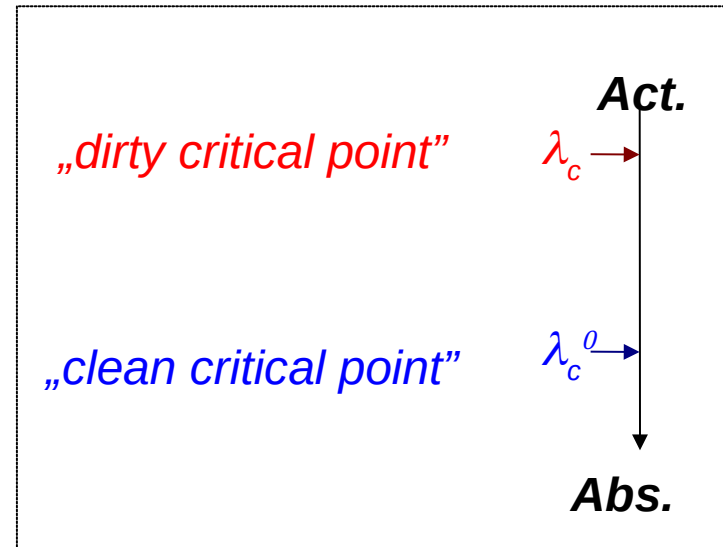
Quenched disorder : rounds phase transition, Griffiths phase:



Rare Region theory for **quench disordered CP**

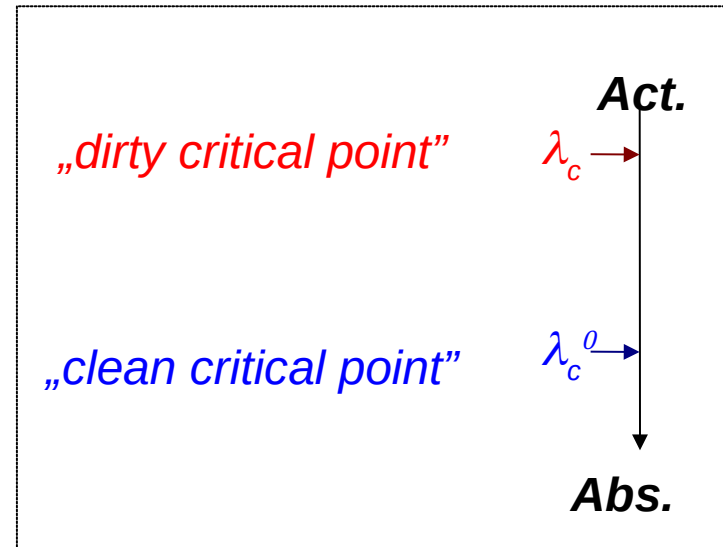
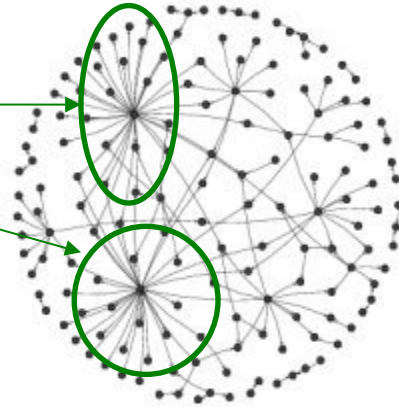
Rare Region theory for **quench disordered CP**

- Fixed (quenched) disorder/impurity
changes the local birth rate
 $\Rightarrow \lambda_c > \lambda_c^0$



Rare Region theory for **quench disordered CP**

- Fixed (quenched) disorder/impurity **changes the local birth rate**
 $\Rightarrow \lambda_c > \lambda_c^0$
- **Locally active**, but arbitrarily large
Rare Regions
in the inactive phase
due to the *inhomogeneities*



Rare Region theory for **quench disordered CP**

- Fixed (quenched) disorder/impurity

changes the local birth rate

$$\Rightarrow \lambda_c > \lambda_c^0$$

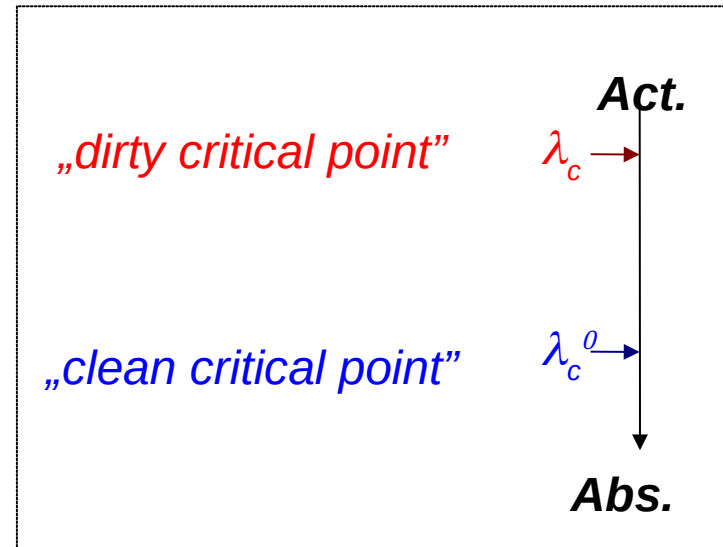
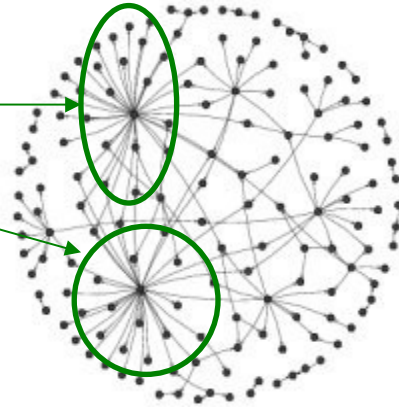
- **Locally active**, but arbitrarily large

Rare Regions

in the inactive phase
due to the **inhomogeneities**

- Probability of RR of size L_R :

$$w(L_R) \sim \exp(-c L_R)$$



Rare Region theory for **quench disordered CP**

- Fixed (quenched) disorder/impurity

changes the local birth rate

$$\Rightarrow \lambda_c > \lambda_c^0$$

- **Locally active**, but arbitrarily large

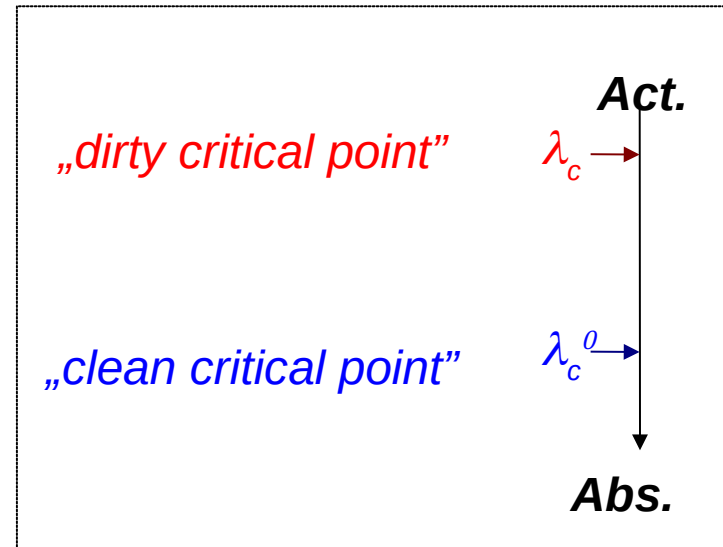
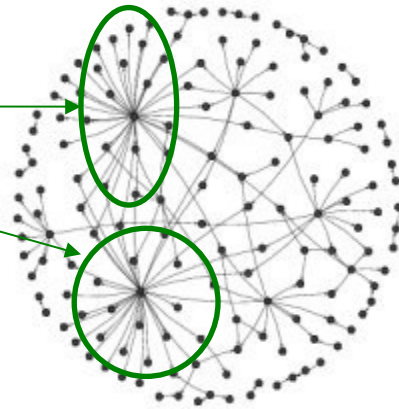
Rare Regions

in the inactive phase
due to the **inhomogeneities**

- Probability of RR of size L_R :

$$w(L_R) \sim \exp(-c L_R)$$

contribute to the density: $\rho(t) \sim \int dL_R L_R w(L_R) \exp[-t/\tau(L_R)]$



Rare Region theory for **quench disordered CP**

- Fixed (quenched) disorder/impurity

changes the local birth rate

$$\Rightarrow \lambda_c > \lambda_c^0$$

- **Locally active**, but arbitrarily large

Rare Regions

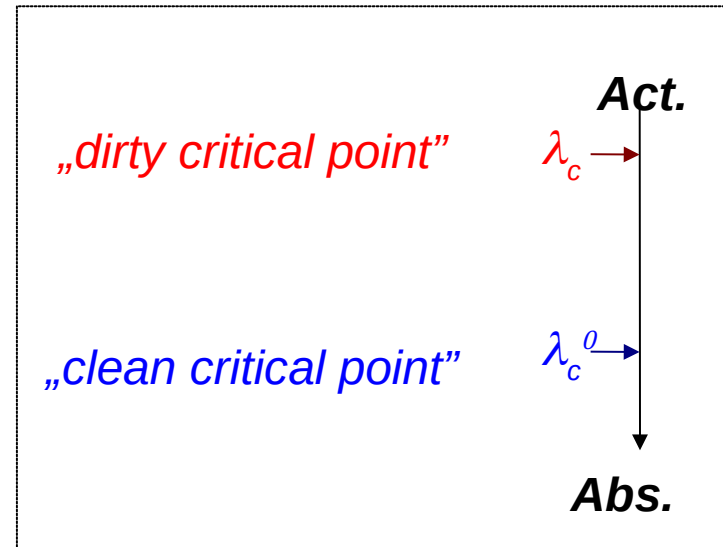
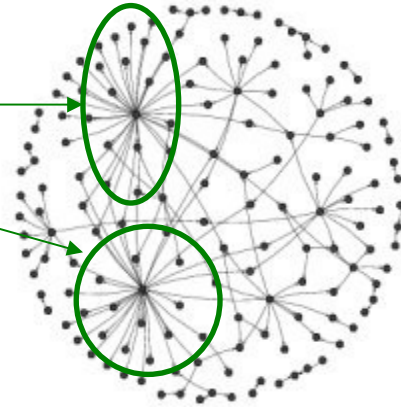
in the inactive phase
due to the **inhomogeneities**

- Probability of RR of size L_R :

$$w(L_R) \sim \exp(-c L_R)$$

contribute to the density: $\rho(t) \sim \int dL_R L_R w(L_R) \exp[-t/\tau(L_R)]$

- For $\lambda < \lambda_c^0$: conventional (exponentially fast) decay



Rare Region theory for **quench disordered CP**

- Fixed (quenched) disorder/impurity **changes the local birth rate**

$$\Rightarrow \lambda_c > \lambda_c^0$$

- **Locally active**, but arbitrarily large

Rare Regions

in the inactive phase due to the **inhomogeneities**

- Probability of RR of size L_R :

$$w(L_R) \sim \exp(-c L_R)$$

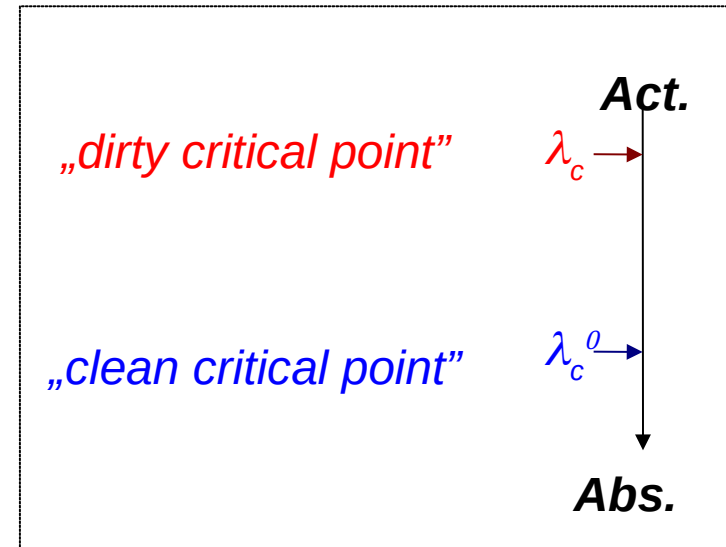
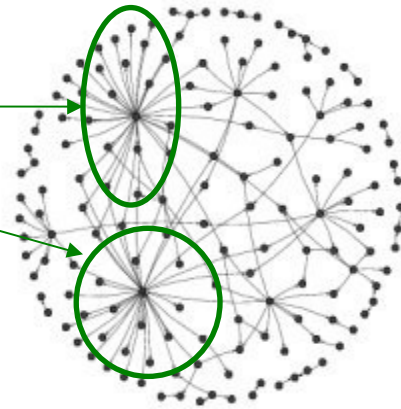
contribute to the density: $\rho(t) \sim \int dL_R L_R w(L_R) \exp[-t/\tau(L_R)]$

- For $\lambda < \lambda_c^0$: conventional (exponentially fast) decay

- At λ_c^0 the characteristic time scales as: $\tau(L_R) \sim L_R^z \Rightarrow$

$$\ln \rho(t) \sim t^{d/(d+z)}$$

saddle point analysis:
stretched exponential



Rare Region theory for **quench disordered CP**

- Fixed (quenched) disorder/impurity **changes the local birth rate**

$$\Rightarrow \lambda_c > \lambda_c^0$$

- **Locally active**, but arbitrarily large

Rare Regions

in the inactive phase due to the **inhomogeneities**

- Probability of RR of size L_R :

$$w(L_R) \sim \exp(-c L_R)$$

contribute to the density: $\rho(t) \sim \int dL_R L_R w(L_R) \exp[-t/\tau(L_R)]$

- For $\lambda < \lambda_c^0$: conventional (exponentially fast) decay

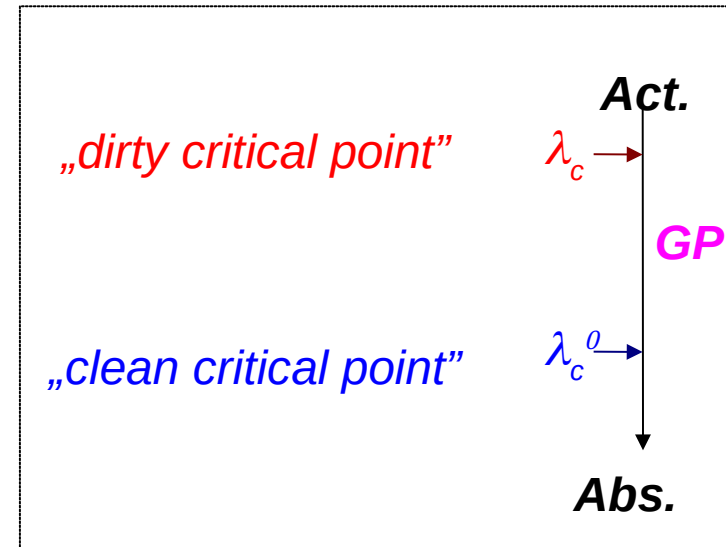
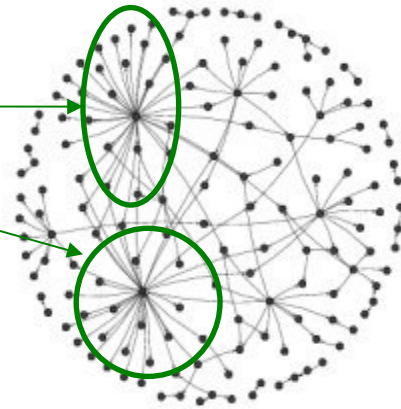
- At λ_c^0 the characteristic time scales as: $\tau(L_R) \sim L_R^z \Rightarrow$

$$\ln \rho(t) \sim t^{d/(d+z)}$$

- For $\lambda_c^0 < \lambda < \lambda_c$:

$$\tau(L_R) \sim \exp(b L_R):$$

saddle point analysis:
stretched exponential
Griffiths Phase



Rare Region theory for **quench disordered CP**

- Fixed (quenched) disorder/impurity **changes the local birth rate**

$$\Rightarrow \lambda_c > \lambda_c^0$$

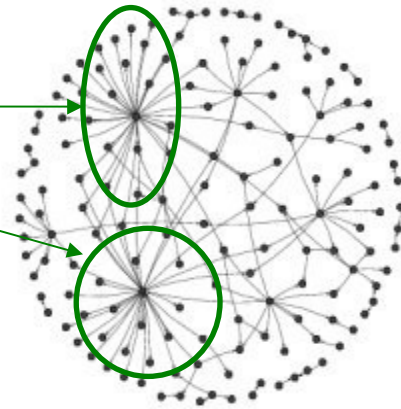
- **Locally active**, but arbitrarily large

Rare Regions

in the inactive phase due to the **inhomogeneities**

- Probability of RR of size L_R :

$$w(L_R) \sim \exp(-c L_R)$$



contribute to the density: $\rho(t) \sim \int dL_R L_R w(L_R) \exp[-t/\tau(L_R)]$

- For $\lambda < \lambda_c^0$: conventional (exponentially fast) decay

- At λ_c^0 the characteristic time scales as: $\tau(L_R) \sim L_R^z \Rightarrow$

$$\ln \rho(t) \sim t^{d/(d+z)}$$

- For $\lambda_c^0 < \lambda < \lambda_c$:

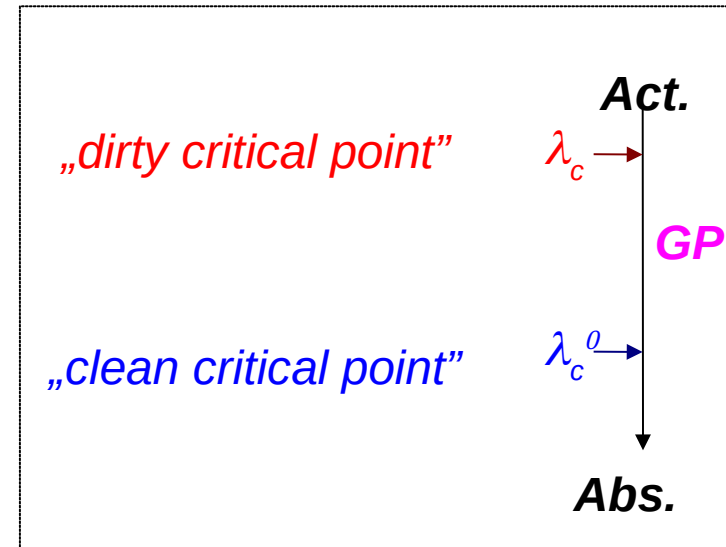
$$\tau(L_R) \sim \exp(b L_R):$$

$$\rho(t) \sim t^{-c/b}$$

saddle point analysis:
stretched exponential

Griffiths Phase

continuously changing exponents



Rare Region theory for **quench disordered CP**

- Fixed (quenched) disorder/impurity **changes the local birth rate**
 $\Rightarrow \lambda_c > \lambda_c^0$

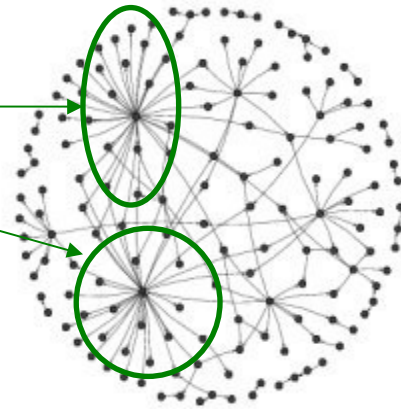
- **Locally active**, but arbitrarily large

Rare Regions

in the inactive phase due to the **inhomogeneities**

- Probability of RR of size L_R :

$$w(L_R) \sim \exp(-c L_R)$$



contribute to the density: $\rho(t) \sim \int dL_R L_R w(L_R) \exp[-t/\tau(L_R)]$

- For $\lambda < \lambda_c^0$: conventional (exponentially fast) decay

- At λ_c^0 the characteristic time scales as: $\tau(L_R) \sim L_R^z \Rightarrow$

$$\ln \rho(t) \sim t^{d/(d+z)}$$

saddle point analysis:
stretched exponential

- For $\lambda_c^0 < \lambda < \lambda_c$:

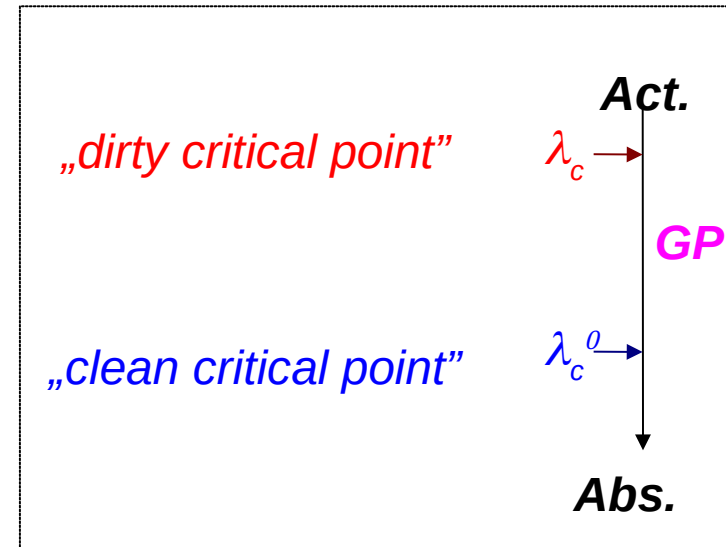
$$\tau(L_R) \sim \exp(b L_R):$$

Griffiths Phase

$$\rho(t) \sim t^{-c/b}$$

continuously changing exponents

- At λ_c : b may diverge $\rightarrow \rho(t) \sim \ln(t)^{-\alpha}$ **Infinite randomness fixed point scaling**



Rare Region theory for **quench disordered CP**

- Fixed (quenched) disorder/impurity **changes the local birth rate**
 $\Rightarrow \lambda_c > \lambda_c^0$

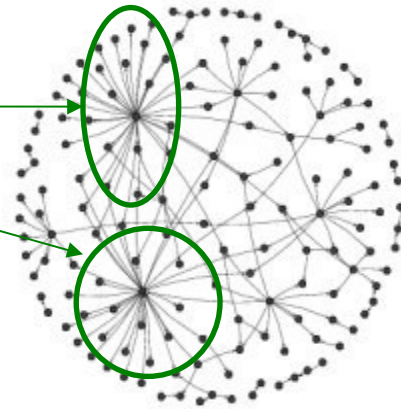
- **Locally active**, but arbitrarily large

Rare Regions

in the inactive phase due to the **inhomogeneities**

- Probability of RR of size L_R :

$$w(L_R) \sim \exp(-c L_R)$$



contribute to the density: $\rho(t) \sim \int dL_R L_R w(L_R) \exp[-t/\tau(L_R)]$

- For $\lambda < \lambda_c^0$: conventional (exponentially fast) decay

- At λ_c^0 the characteristic time scales as: $\tau(L_R) \sim L_R^z \Rightarrow$

$$\ln \rho(t) \sim t^{d/(d+z)}$$

saddle point analysis:
stretched exponential

- For $\lambda_c^0 < \lambda < \lambda_c$:

$$\tau(L_R) \sim \exp(b L_R):$$

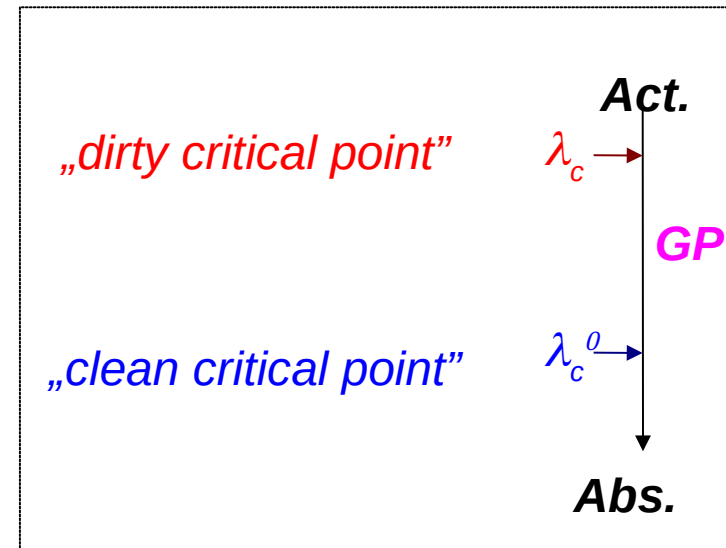
Griffiths Phase

$$\rho(t) \sim t^{-c/b}$$

continuously changing exponents

- At λ_c : b may diverge $\rightarrow \rho(t) \sim \ln(t)^{-\alpha}$ Infinite randomness fixed point scaling

- **GP: Dynamical (scaling) criticality + susceptibility diverges**



Rare Region theory for **quench disordered CP**

- Fixed (quenched) disorder/impurity

changes the local birth rate

$$\Rightarrow \lambda_c > \lambda_c^0$$

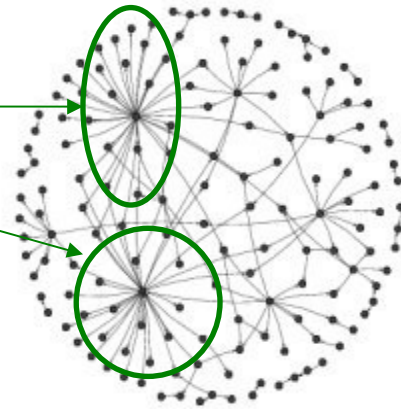
- **Locally active**, but arbitrarily large

Rare Regions

in the inactive phase due to the **inhomogeneities**

- Probability of RR of size L_R :

$$w(L_R) \sim \exp(-c L_R)$$



contribute to the density: $\rho(t) \sim \int dL_R L_R w(L_R) \exp[-t/\tau(L_R)]$

- For $\lambda < \lambda_c^0$: conventional (exponentially fast) decay

- At λ_c^0 the characteristic time scales as: $\tau(L_R) \sim L_R^z \Rightarrow$

$$\ln \rho(t) \sim t^{d/(d+z)}$$

saddle point analysis:
stretched exponential

- For $\lambda_c^0 < \lambda < \lambda_c$:

$$\tau(L_R) \sim \exp(b L_R):$$

Griffiths Phase

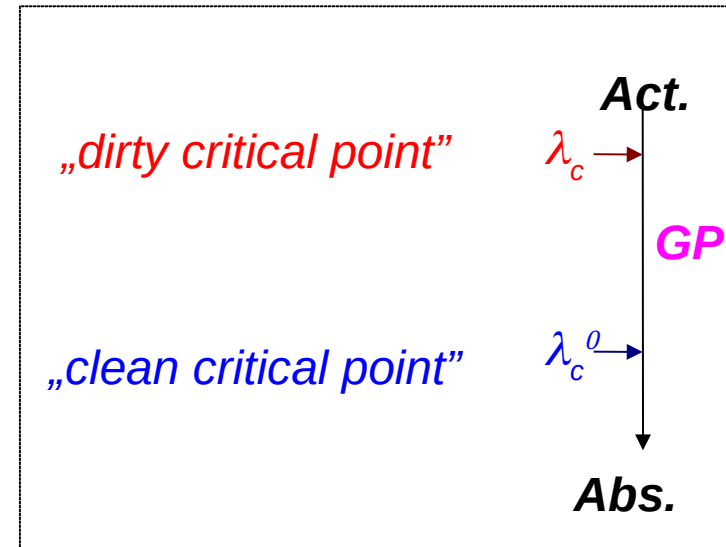
$$\rho(t) \sim t^{-c/b}$$

continuously changing exponents

- At λ_c : b may diverge $\rightarrow \rho(t) \sim \ln(t)^{-\alpha}$ Infinite randomness fixed point scaling

- **GP: Dynamical (scaling) criticality + susceptibility diverges**

GP can occur by pure topological disorder in finite dimensional systems



Hybrid Phase Transitions and GP in excitable (threshold) models

Hybrid Phase Transitions and GP in excitable (threshold) models

- Mean-field for threshold models

with activation :

$$\sum_j x_j w_{i,j} \geq K,$$

Hybrid Phase Transitions and GP in excitable (threshold) models

- Mean-field for threshold models

with activation :

$$\frac{d\rho}{dt} = \lambda\rho^2(1 - \rho) - v\rho, \quad \sum_j x_j w_{i,j} \geq K,$$

Hybrid Phase Transitions and GP in excitable (threshold) models

- Mean-field for threshold models

with activation :

$$\frac{d\rho}{dt} = \lambda\rho^2(1 - \rho) - v\rho, \quad \sum_j x_j w_{i,j} \geq K, \quad v = 1 - \lambda,$$

Hybrid Phase Transitions and GP in excitable (threshold) models

- Mean-field for threshold models

with activation :

$$\frac{d\rho}{dt} = \lambda\rho^2(1 - \rho) - v\rho, \quad \sum_j x_j w_{i,j} \geq K, \\ v = 1 - \lambda,$$

which can be solved as

$$\rho = \frac{\lambda \pm \sqrt{\lambda^2 - 4\lambda(1 - \lambda)}}{2\lambda}.$$

Hybrid Phase Transitions and GP in excitable (threshold) models

- Mean-field for threshold models

with activation :

$$\frac{d\rho}{dt} = \lambda\rho^2(1 - \rho) - v\rho, \quad \sum_j x_j w_{i,j} \geq K, \\ v = 1 - \lambda,$$

which can be solved as

$$\rho = \frac{\lambda \pm \sqrt{\lambda^2 - 4\lambda(1 - \lambda)}}{2\lambda}.$$

The solution is real and positive if

$$\lambda > \lambda_c = 4/5,$$

Hybrid Phase Transitions and GP in excitable (threshold) models

- Mean-field for threshold models

with activation :

$$\frac{d\rho}{dt} = \lambda\rho^2(1 - \rho) - v\rho, \quad \sum_j x_j w_{i,j} \geq K, \\ v = 1 - \lambda,$$

which can be solved as

$$\rho = \frac{\lambda \pm \sqrt{\lambda^2 - 4\lambda(1 - \lambda)}}{2\lambda}.$$

The solution is real and positive if

$$\lambda > \lambda_c = 4/5,$$

providing a threshold within a system of size N

$$\Lambda_c = \frac{8}{5(N - 1)(N - 2)}$$

and an order parameter for $\Lambda \rightarrow \Lambda_c^+$

$$\rho_c = 1/2.$$

Hybrid Phase Transitions and GP in excitable (threshold) models

- Mean-field for threshold models

with activation :

$$\frac{d\rho}{dt} = \lambda\rho^2(1 - \rho) - v\rho, \quad \sum_j x_j w_{i,j} \geq K, \\ v = 1 - \lambda,$$

which can be solved as

$$\rho = \frac{\lambda \pm \sqrt{\lambda^2 - 4\lambda(1 - \lambda)}}{2\lambda}.$$

The solution is real and positive if

$$\lambda > \lambda_c = 4/5,$$

providing a threshold within a system of size N

$$\Lambda_c = \frac{8}{5(N - 1)(N - 2)}$$

and an order parameter for $\Lambda \rightarrow \Lambda_c^+$

$$\rho_c = 1/2.$$

$$\rho(t) - \rho_c \sim t^{-1}.$$

Hybrid Phase Transitions and GP in excitable (threshold) models

- Mean-field for threshold models

with activation :

$$\frac{d\rho}{dt} = \lambda\rho^2(1 - \rho) - v\rho, \quad \sum_j x_j w_{i,j} \geq K, \\ v = 1 - \lambda,$$

which can be solved as

$$\rho = \frac{\lambda \pm \sqrt{\lambda^2 - 4\lambda(1 - \lambda)}}{2\lambda}.$$

The solution is real and positive if

$$\lambda > \lambda_c = 4/5,$$

providing a threshold within a system of size N

$$\Lambda_c = \frac{8}{5(N - 1)(N - 2)}$$

and an order parameter for $\Lambda \rightarrow \Lambda_c^+$

$$\rho_c = 1/2.$$

$$\rho(t) - \rho_c \sim t^{-1}, \quad (\rho - \rho_c) \propto (\lambda - \lambda_c)^{1/2}$$

Hybrid Phase Transitions and GP in excitable (threshold) models

- Mean-field for threshold models

with activation :

$$\frac{d\rho}{dt} = \lambda\rho^2(1 - \rho) - v\rho, \quad \sum_j x_j w_{i,j} \geq K, \quad v = 1 - \lambda,$$

which can be solved as

$$\rho = \frac{\lambda \pm \sqrt{\lambda^2 - 4\lambda(1 - \lambda)}}{2\lambda}.$$

The solution is real and positive if

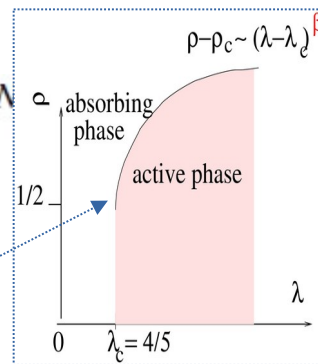
$$\lambda > \lambda_c = 4/5,$$

providing a threshold within a system of size N

$$\Lambda_c = \frac{8}{5(N - 1)(N - 2)}$$

and an order parameter for $\Lambda \rightarrow \Lambda_c^+$

$$\rho_c = 1/2.$$



$$\rho(t) - \rho_c \sim t^{-1}, \quad (\rho - \rho_c) \propto (\lambda - \lambda_c)^{1/2}$$

Hybrid Phase Transitions and GP in excitable (threshold) models

In heterogenous HMN models

- Mean-field for threshold models with activation :

$$\frac{d\rho}{dt} = \lambda\rho^2(1 - \rho) - v\rho, \quad \sum_j x_j w_{i,j} \geq K, \quad v = 1 - \lambda,$$

which can be solved as

$$\rho = \frac{\lambda \pm \sqrt{\lambda^2 - 4\lambda(1 - \lambda)}}{2\lambda}.$$

The solution is real and positive if

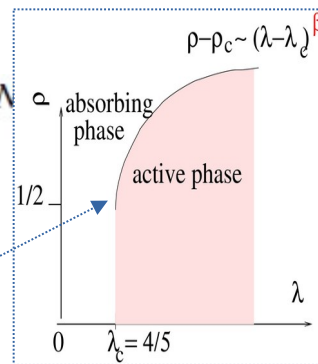
$$\lambda > \lambda_c = 4/5,$$

providing a threshold within a system of size N

$$\Lambda_c = \frac{8}{5(N - 1)(N - 2)}$$

and an order parameter for $\Lambda \rightarrow \Lambda_c^+$

$$\rho_c = 1/2.$$



$$\rho(t) - \rho_c \sim t^{-1}, \quad (\rho - \rho_c) \propto (\lambda - \lambda_c)^{1/2}$$

Hybrid Phase Transitions and GP in excitable (threshold) models

- Mean-field for threshold models with activation :

$$\frac{d\rho}{dt} = \lambda\rho^2(1 - \rho) - v\rho, \quad \sum_j x_j w_{i,j} \geq K, \quad v = 1 - \lambda,$$

which can be solved as

$$\rho = \frac{\lambda \pm \sqrt{\lambda^2 - 4\lambda(1 - \lambda)}}{2\lambda}.$$

The solution is real and positive if

$$\lambda > \lambda_c = 4/5,$$

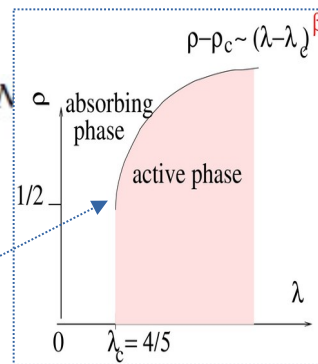
providing a threshold within a system of size N

$$\Lambda_c = \frac{8}{5(N - 1)(N - 2)}$$

and an order parameter for $\Lambda \rightarrow \Lambda_c^+$

$$\rho_c = 1/2.$$

$$\rho(t) - \rho_c \sim t^{-1}, \quad (\rho - \rho_c) \propto (\lambda - \lambda_c)^{1/2}$$



**In heterogenous HMN models
HPT + GP + Multistable states !**

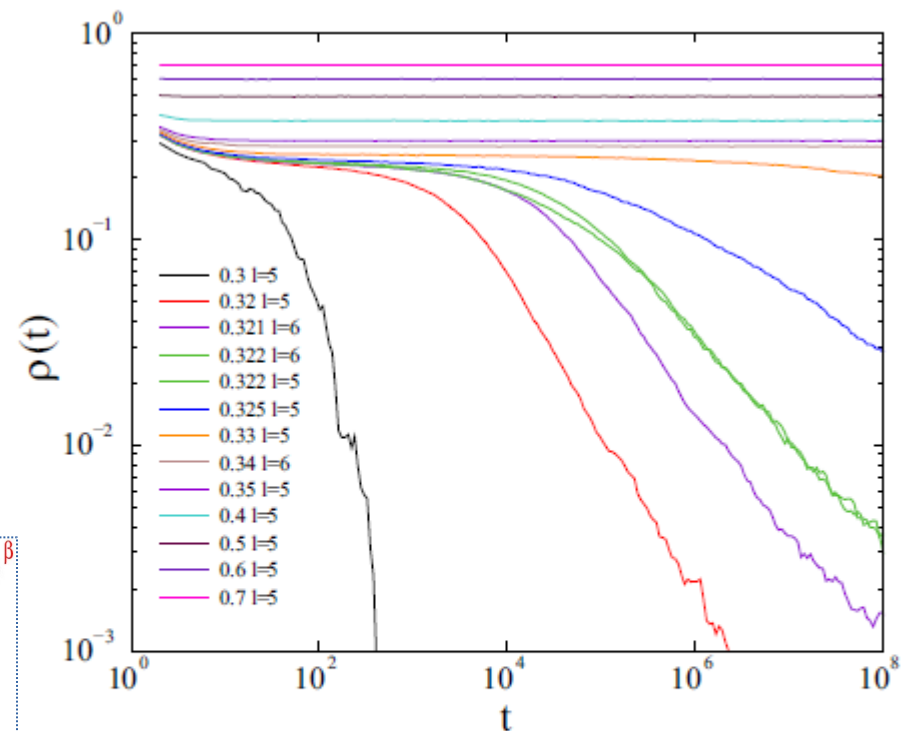


FIG. 9. Evolution of $\rho(t)$ for different λ in case of starting from fully active state in the excitatory model with levels: $l = 5, 6$. From bottom to top symbols: $\lambda = 0.30, 0.32, 0.321$ ($l = 6$), $0.322, 0.322$ ($l = 6$), $0.325, 0.33, 0.34$ ($l = 6$), $0.35, 0.4, 0.5, 0.6, 0.7$.

What do we know about structural brain networks ?

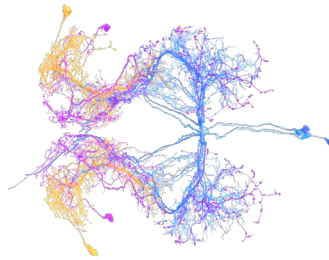
What do we know about structural brain networks ?

The largest precisely explored brain structural networks contains
 $N = 302$ neurons (C. Elegans), fruit-fly hemibrain: $N = 127,978$



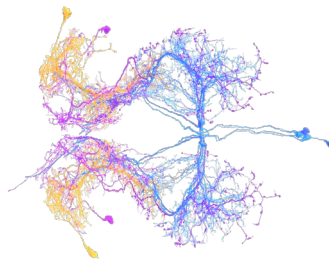
What do we know about structural brain networks ?

The largest precisely explored brain structural networks contains
 $N = 302$ neurons (C. Elegans), fruit-fly hemibrain: $N = 127,978$



What do we know about structural brain networks ?

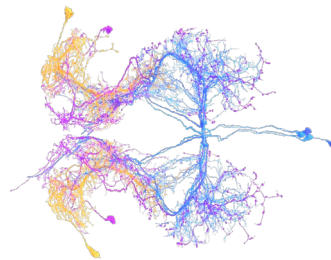
The largest precisely explored brain structural networks contains
 $N = 302$ neurons (C. Elegans), fruit-fly hemibrain: $N = 127,978$



Finite size cutoff of PLs !

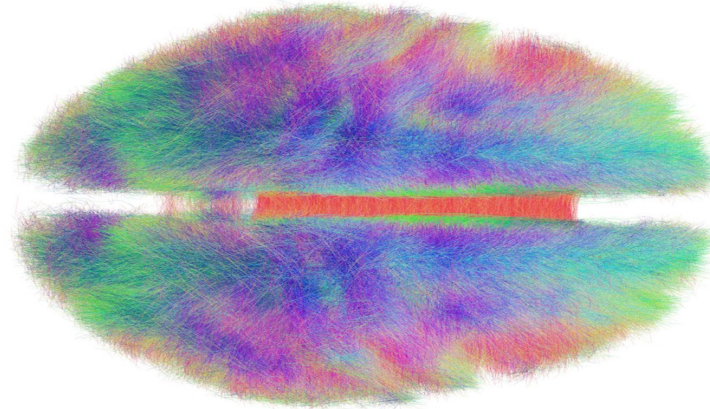
What do we know about structural brain networks ?

The largest precisely explored brain structural networks contains
 $N = 302$ neurons (C. Elegans), fruit-fly hemibrain: $N = 127,978$



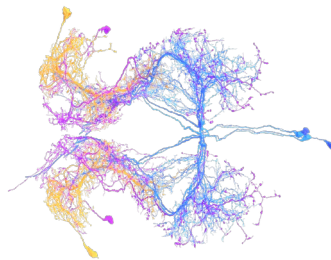
Finite size cutoff of PLs !

Connectomes, obtained by approximative methods like diffusion MRI
contain $N \approx 1.000.000$ nodes (voxels)



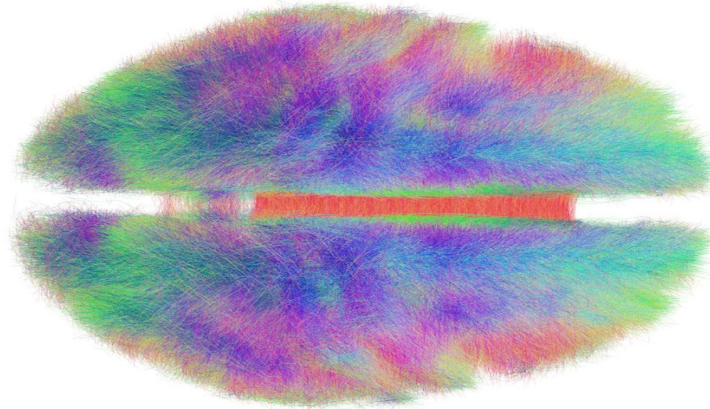
What do we know about structural brain networks ?

The largest precisely explored brain structural networks contains
 $N = 302$ neurons (C. Elegans), fruit-fly hemibrain: $N = 127,978$



Finite size cutoff of PLs !

Connectomes, obtained by approximative methods like diffusion MRI
contain $N \approx 1.000.000$ nodes (voxels)



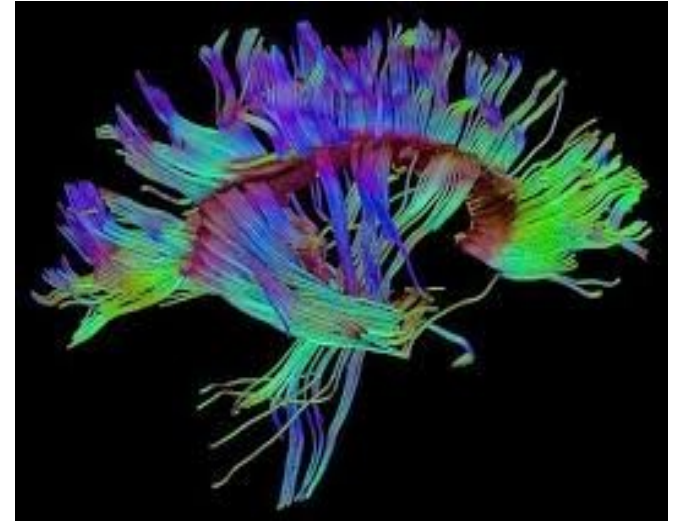
Unknown faithfulness, intensive research to automate image processing

Open Connectome Large Human graphs



Open Connectome Large Human graphs

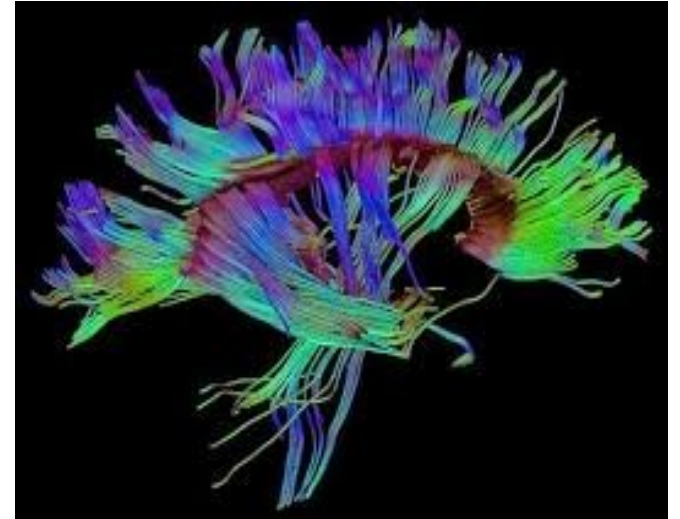
Diffusion and structural MRI images with
 1 mm^3 voxel resolution :
 $10^5 - 10^6$ nodes



Open Connectome Large Human graphs

Diffusion and structural MRI images with
 1 mm^3 voxel resolution :
 $10^5 - 10^6$ nodes

Hierarchical modular graphs



OPEN

The topology of large Open Connectome networks for the human brain

Received: 18 December 2015

Accepted: 12 May 2016

Published: 07 June 2016

Michael T. Gastner^{1,2} & Géza Ódor²

The structural human connectome (i.e. the network of fiber connections in the brain) can be analyzed at ever finer spatial resolution thanks to advances in neuroimaging. Here we analyze several large data sets for the human brain network made available by the Open Connectome Project. We apply statistical model selection to characterize the degree distributions of graphs containing up to $\approx 10^6$ nodes and $\approx 10^8$ edges. A three-parameter generalized Weibull (also known as a stretched exponential) distribution is a good fit to most of the observed degree distributions. For almost all networks, simple power laws cannot fit the data, but in some cases there is statistical support for power laws with an exponential cutoff. We also calculate the topological (graph) dimension D and the small-world coefficient σ of these networks. While σ suggests a small-world topology, we found that $D < 4$ showing that long-distance connections provide only a small correction to the topology of the embedding three-dimensional space.

OPEN

The topology of large Open Connectome networks for the human brain

Received: 18 December 2015

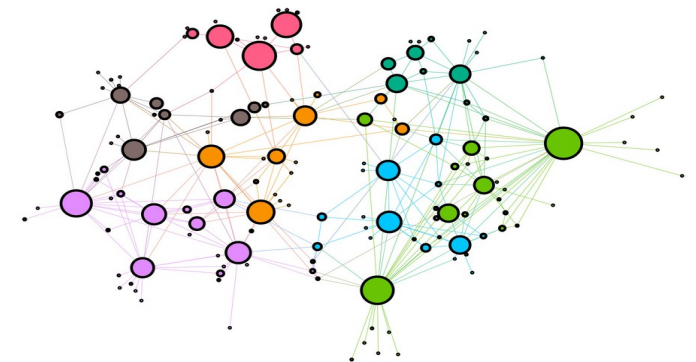
Accepted: 12 May 2016

Published: 07 June 2016

Michael T. Gastner^{1,2} & Géza Ódor²

The structural human connectome (i.e. the network of fiber connections in the brain) can be analyzed at ever finer spatial resolution thanks to advances in neuroimaging. Here we analyze several large data sets for the human brain network made available by the Open Connectome Project. We apply statistical model selection to characterize the degree distributions of graphs containing up to $\approx 10^6$ nodes and $\approx 10^8$ edges. A three-parameter generalized Weibull (also known as a stretched exponential) distribution is a good fit to most of the observed degree distributions. For almost all networks, simple power laws cannot fit the data, but in some cases there is statistical support for power laws with an exponential cutoff. We also calculate the topological (graph) dimension D and the small-world coefficient σ of these networks. While σ suggests a small-world topology, we found that $D < 4$ showing that long-distance connections provide only a small correction to the topology of the embedding three-dimensional space.

Small world, still finite dimensional,
non-scale free,
universal modular graphs



Threshold model simulations on an OCP graph

Threshold model simulations on an OCP graph

KKI-18 graph: 836733 nodes, 4×10^7 weighted, undirected edges

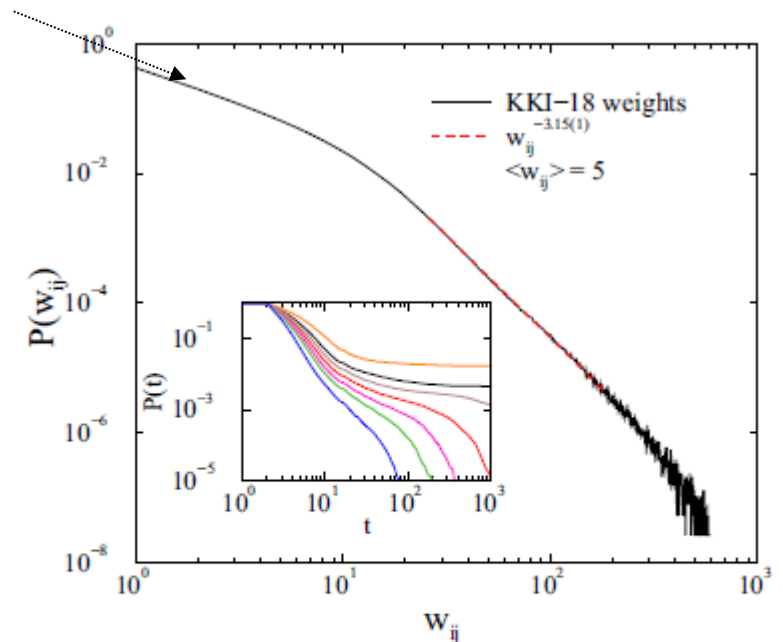


FIG. 1. Link weight probability density function of the KKI-18 OCP graph. Dashed line: a PL fit for intermediate w_{ij} 's. Inset: survival probability in the $K = 6$ threshold model near the transition point for $\lambda = 0.003$, $\nu = 0.3, 0.4, 0.45, 0.5, 0.55, 0.6, 0.7$ (top to bottom curves).

Threshold model simulations on an OCP graph

KKI-18 graph: 836733 nodes, 4×10^7 weighted, undirected edges

Cluster spreading simulations from randomly selected active nodes

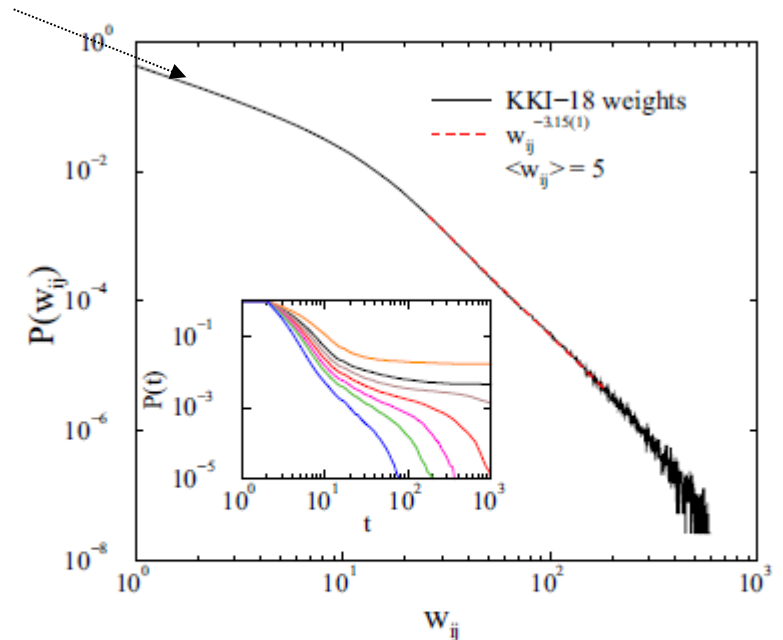


FIG. 1. Link weight probability density function of the KKI-18 OCP graph. Dashed line: a PL fit for intermediate w_{ij} 's. Inset: survival probability in the $K = 6$ threshold model near the transition point for $\lambda = 0.003$, $\nu = 0.3, 0.4, 0.45, 0.5, 0.55, 0.6, 0.7$ (top to bottom curves).

Threshold model simulations on an OCP graph

KKI-18 graph: 836733 nodes, 4×10^7 weighted, undirected edges

Cluster spreading simulations from randomly selected active nodes

Survival probability: $P(t) \propto t^{-\delta}$

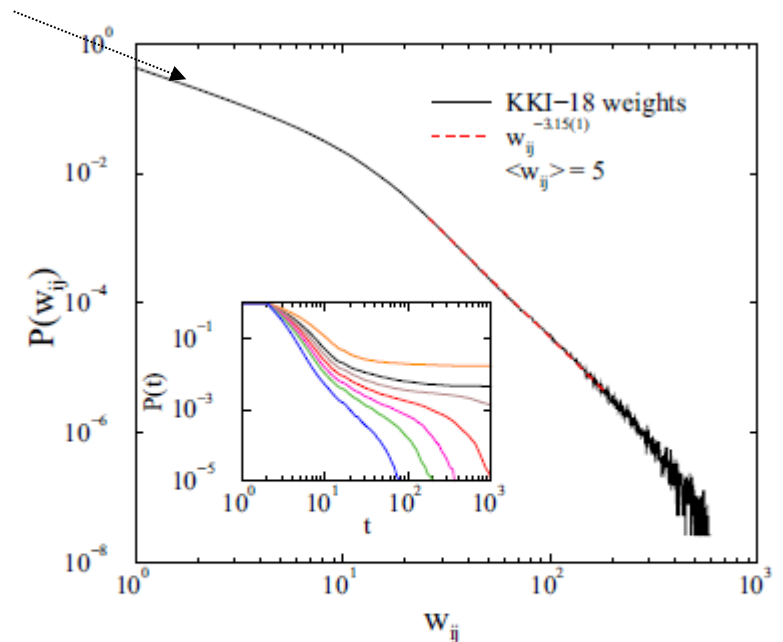


FIG. 1. Link weight probability density function of the KKI-18 OCP graph. Dashed line: a PL fit for intermediate w_{ij} 's. Inset: survival probability in the $K = 6$ threshold model near the transition point for $\lambda = 0.003$, $\nu = 0.3, 0.4, 0.45, 0.5, 0.55, 0.6, 0.7$ (top to bottom curves).

Threshold model simulations on an OCP graph

KKI-18 graph: 836733 nodes, 4×10^7 weighted, undirected edges

Cluster spreading simulations from randomly selected active nodes

Survival probability: $P(t) \propto t^{-\delta}$

Does not show critical region, but discontinuous phase transition

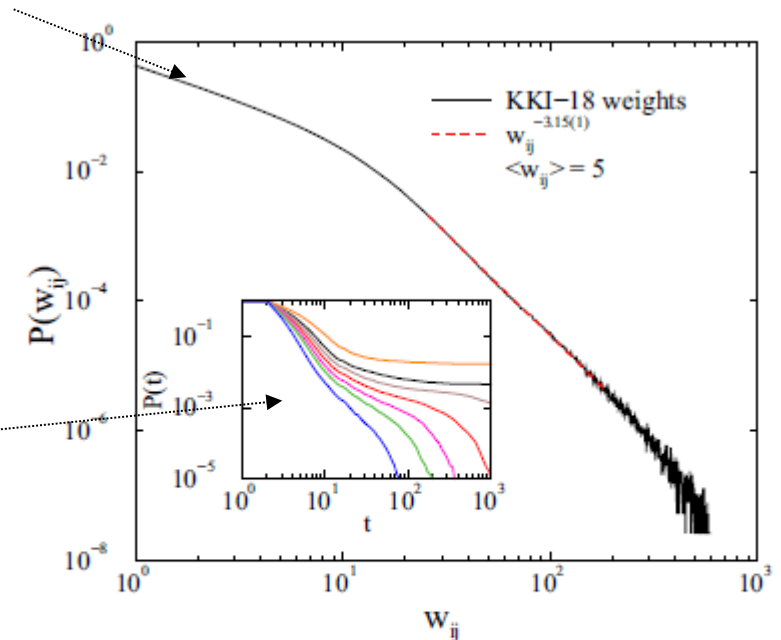


FIG. 1. Link weight probability density function of the KKI-18 OCP graph. Dashed line: a PL fit for intermediate w_{ij} 's. Inset: survival probability in the $K = 6$ threshold model near the transition point for $\lambda = 0.003$, $\nu = 0.3, 0.4, 0.45, 0.5, 0.55, 0.6, 0.7$ (top to bottom curves).

Threshold model simulations on an OCP graph

KKI-18 graph: 836733 nodes, 4×10^7 weighted, undirected edges

Cluster spreading simulations from randomly selected active nodes

Survival probability: $P(t) \propto t^{-\delta}$

Does not show critical region, but discontinuous phase transition

→ Inherent disorder of KKI-18 can't round the phase transition,
No PLs, critical point, Hub effects!

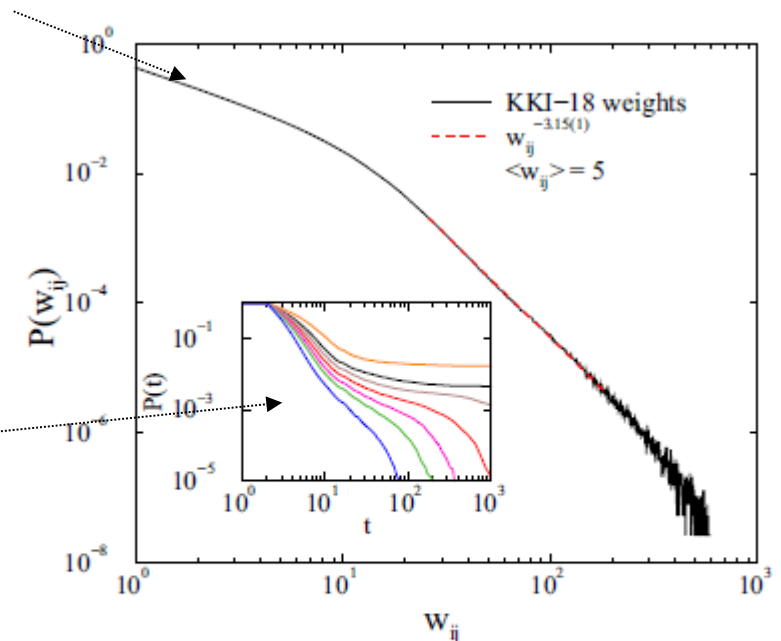


FIG. 1. Link weight probability density function of the KKI-18 OCP graph. Dashed line: a PL fit for intermediate w_{ij} 's. Inset: survival probability in the $K = 6$ threshold model near the transition point for $\lambda = 0.003$, $\nu = 0.3, 0.4, 0.45, 0.5, 0.55, 0.6, 0.7$ (top to bottom curves).

Threshold model simulations on an OCP graph

KKI-18 graph: 836733 nodes, 4×10^7 weighted, undirected edges

Cluster spreading simulations from randomly selected active nodes

Survival probability: $P(t) \propto t^{-\delta}$

Does not show critical region, but discontinuous phase transition

→ Inherent disorder of KKI-18 can't round the phase transition,

No PLs, critical point, Hub effects!

Relative Threshold model :

incoming weights normalized by the sum :
to model homogeneous sensitivity of nodes $w'_{i,j} = w_{i,j} / \sum_{j \in \text{neighb. of } i} w_{i,j}$.

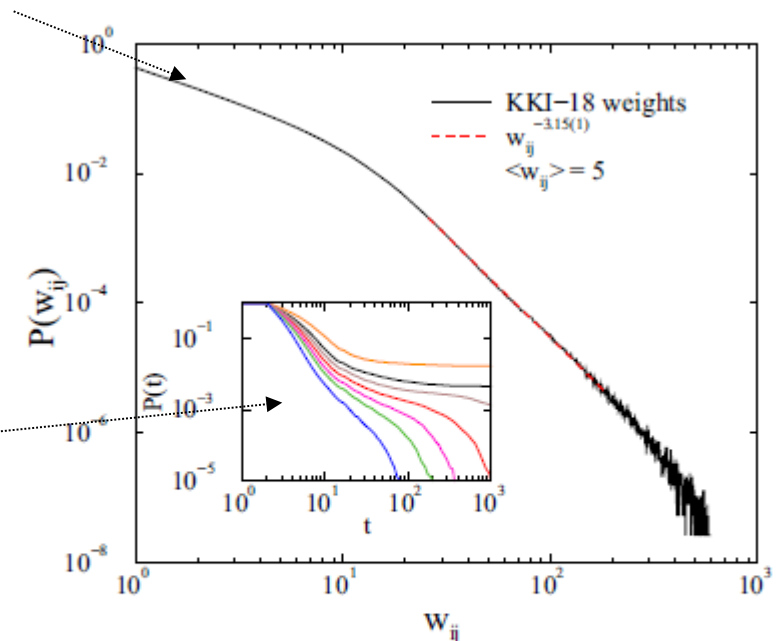


FIG. 1. Link weight probability density function of the KKI-18 OCP graph. Dashed line: a PL fit for intermediate w_{ij} 's. Inset: survival probability in the $K = 6$ threshold model near the transition point for $\lambda = 0.003, \nu = 0.3, 0.4, 0.45, 0.5, 0.55, 0.6, 0.7$ (top to bottom curves).

Threshold model simulations on an OCP graph

KKI-18 graph: 836733 nodes, 4×10^7 weighted, undirected edges

Cluster spreading simulations from randomly selected active nodes

Survival probability: $P(t) \propto t^{-\delta}$

Does not show critical region, but discontinuous phase transition

→ Inherent disorder of KKI-18 can't round the phase transition,

No PLs, critical point, Hub effects!

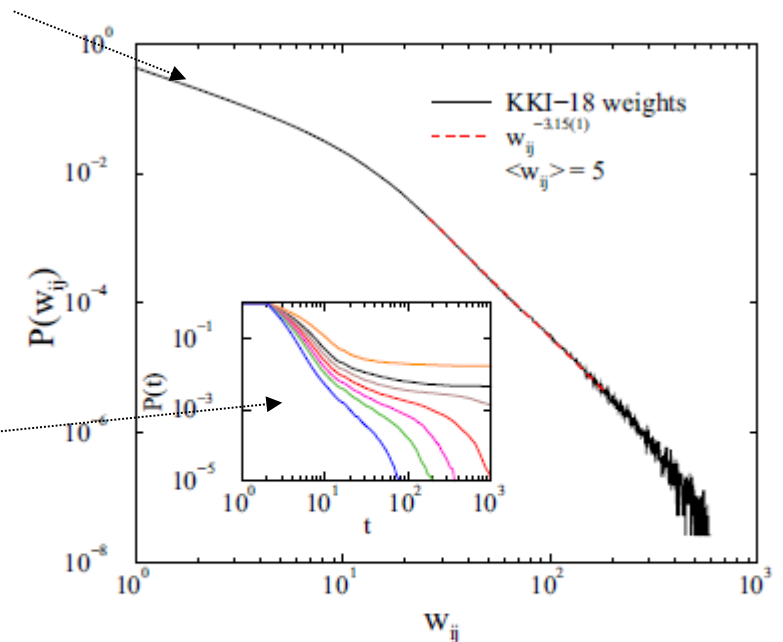


FIG. 1. Link weight probability density function of the KKI-18 OCP graph. Dashed line: a PL fit for intermediate w_{ij} 's. Inset: survival probability in the $K = 6$ threshold model near the transition point for $\lambda = 0.003, \nu = 0.3, 0.4, 0.45, 0.5, 0.55, 0.6, 0.7$ (top to bottom curves).

Relative Threshold model :

incoming weights normalized by the sum : $w'_{i,j} = w_{i,j} / \sum_{j \in \text{neighb. of } i} w_{i,j}$
to model homogeneous sensitivity of nodes

Inhibition: randomly selected weights are flipped to negative (quenched)

$$w'_{i,j} = -w_{i,j}$$

Slow PL dynamics, Griffiths effects

Slow PL dynamics, Griffiths effects

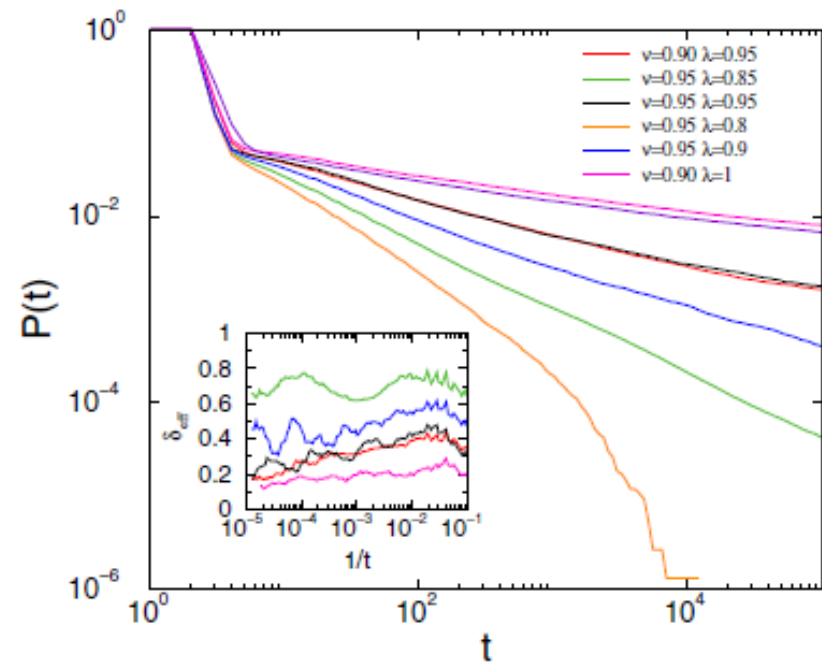


FIG. 4. The same as Fig. 2 in the case of the undirected graph. Inset: Local slopes of the curves.

Slow PL dynamics, Griffiths effects

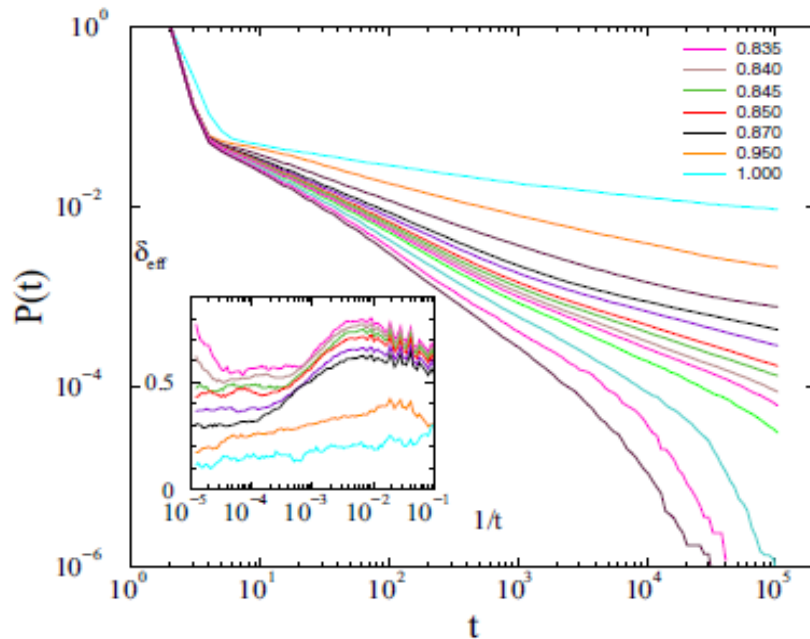


FIG. 2. Avalanche survival distribution of the relative threshold model with $K = 0.25$, for $\nu = 0.95$ and $\lambda = 0.8, 0.81, 0.82, 0.83, 0.835, 0.84, 0.845, 0.85, 0.86, 0.87, 0.9, 0.95, 1$ (bottom to top curves). Inset: Local slopes of the same from $\lambda = 0.835$ to $\lambda = 1$ (top to bottom curves). Griffiths effect manifests by slopes reaching a constant value as $1/t \rightarrow 0$.

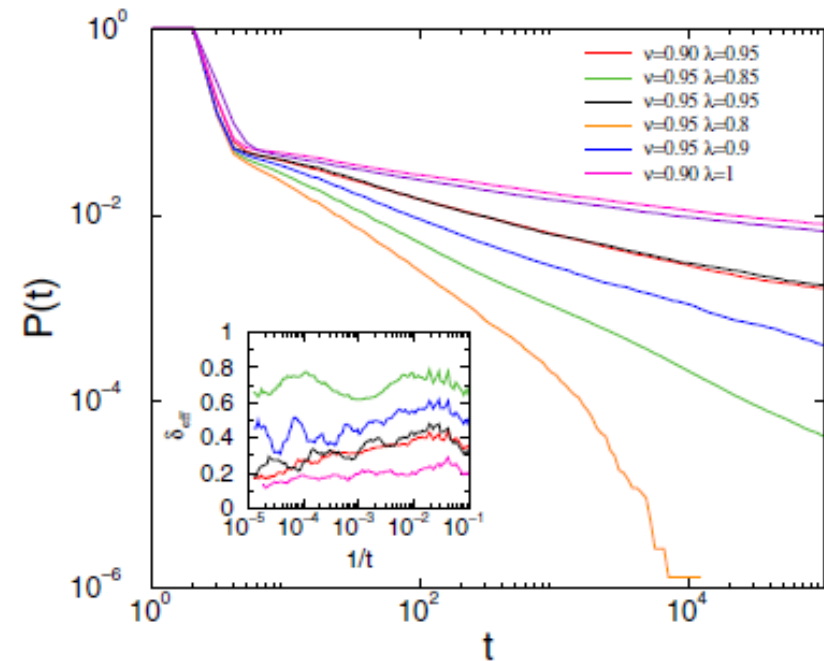


FIG. 4. The same as Fig. 2 in the case of the undirected graph. Inset: Local slopes of the curves.

- (a) 20% of links are turned directional, randomly
- (b) Unidirectional

Slow PL dynamics, Griffiths effects

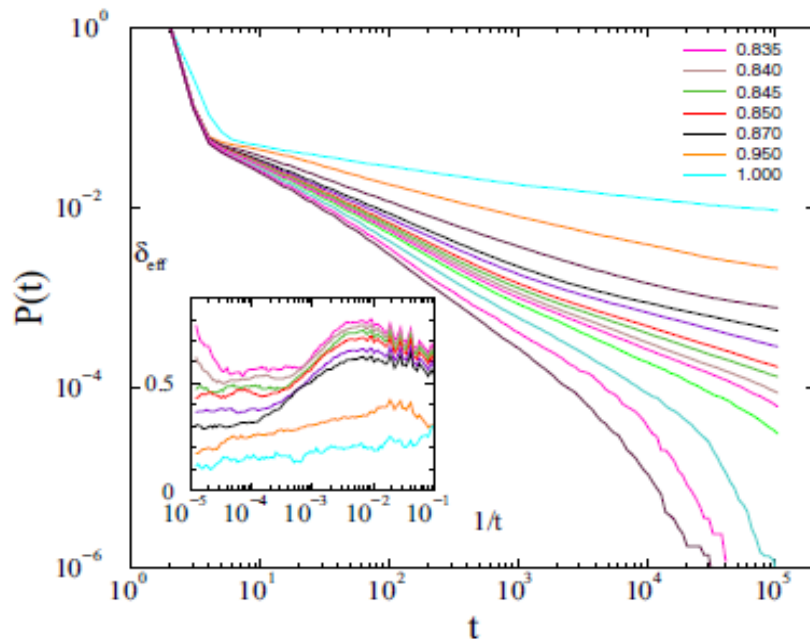


FIG. 2. Avalanche survival distribution of the relative threshold model with $K = 0.25$, for $\nu = 0.95$ and $\lambda = 0.8, 0.81, 0.82, 0.83, 0.835, 0.84, 0.845, 0.85, 0.86, 0.87, 0.9, 0.95, 1$ (bottom to top curves). Inset: Local slopes of the same from $\lambda = 0.835$ to $\lambda = 1$ (top to bottom curves). Griffiths effect manifests by slopes reaching a constant value as $1/t \rightarrow 0$.

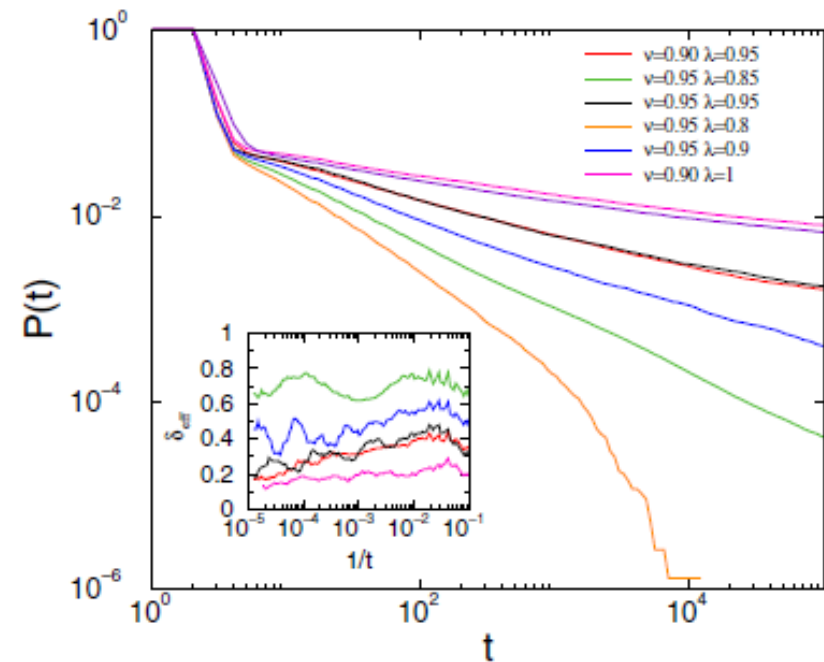


FIG. 4. The same as Fig. 2 in the case of the undirected graph. Inset: Local slopes of the curves.

(a) 20% of links are turned directional, randomly

(b) Unidirectional

No qualitative difference, but proves robustness (for more long links)

Avalanche size distribution compared to experiments

Avalanche size distribution compared to experiments

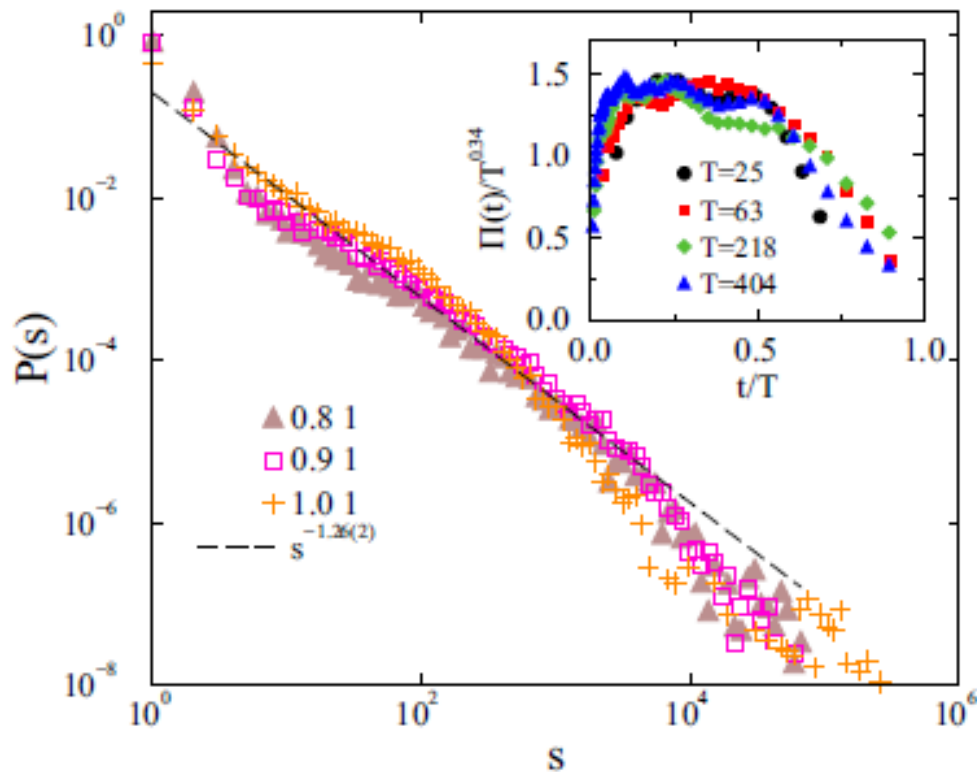


FIG. 3. Avalanche size distribution of the relative threshold model with $K = 0.25$, for $\nu = 1$ and $\lambda = 1, 0.9, 0.8$. Dashed line: PL fit to the $\lambda = 0.8$ case. Inset: Avalanche shape collapse for $T = 25, 63, 218, 404$ at $\lambda = 0.86$ and $\nu = 0.95$.

Avalanche size distribution compared to experiments

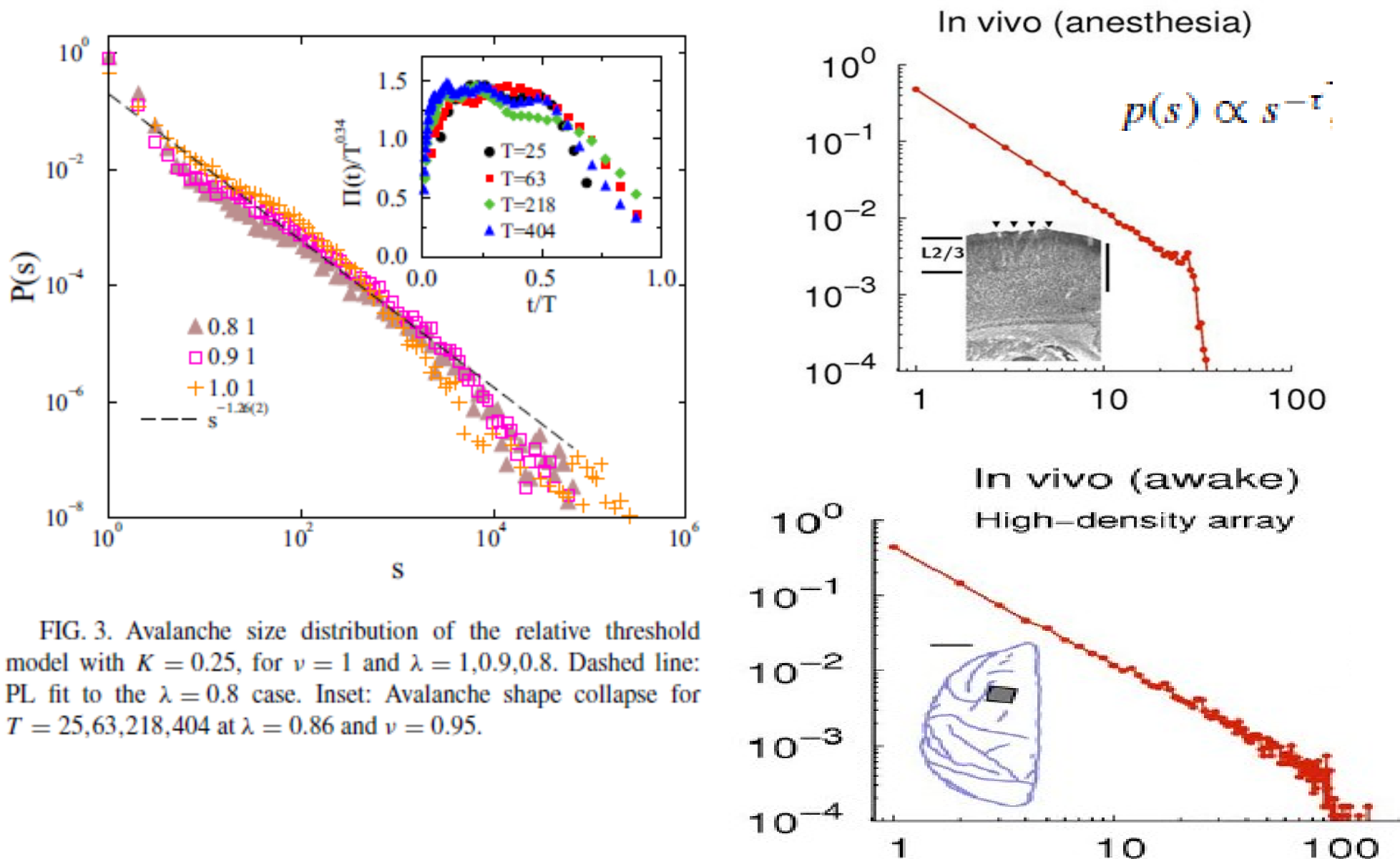


FIG. 3. Avalanche size distribution of the relative threshold model with $K = 0.25$, for $\nu = 1$ and $\lambda = 1, 0.9, 0.8$. Dashed line: PL fit to the $\lambda = 0.8$ case. Inset: Avalanche shape collapse for $T = 25, 63, 218, 404$ at $\lambda = 0.86$ and $\nu = 0.95$.

Avalanche size distribution compared to experiments

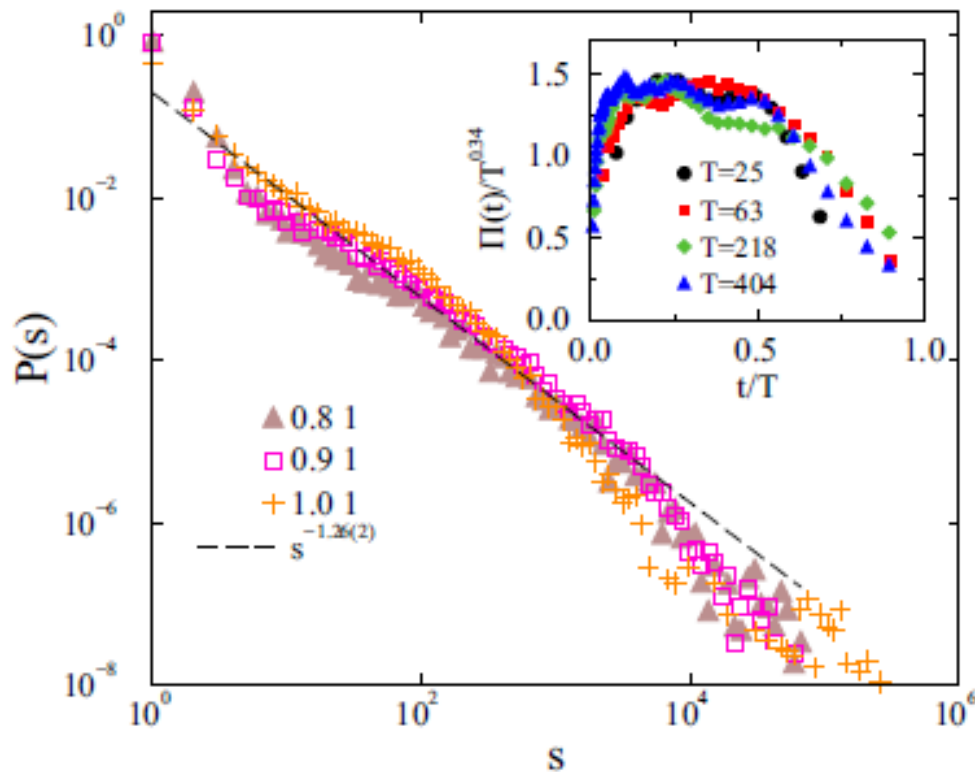
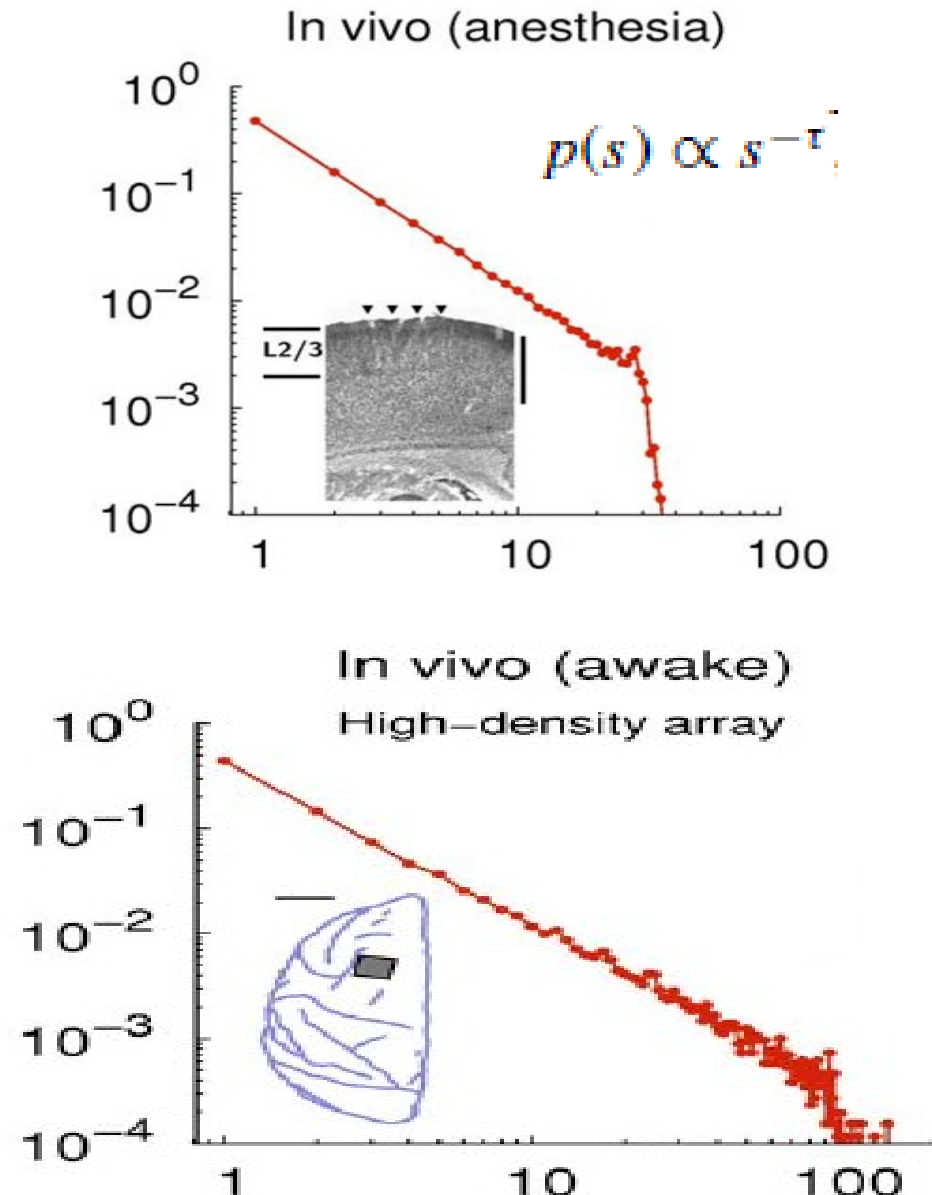


FIG. 3. Avalanche size distribution of the relative threshold model with $K = 0.25$, for $\nu = 1$ and $\lambda = 1, 0.9, 0.8$. Dashed line: PL fit to the $\lambda = 0.8$ case. Inset: Avalanche shape collapse for $T = 25, 63, 218, 404$ at $\lambda = 0.86$ and $\nu = 0.95$.

Scaling near experimental values in the Griffiths Phase ($\tau \sim 1.5$)



Robustness of Griffiths effects in homeostatic connectome threshold models

G. Ó. Phys. Rev. E 98 (2018) 042126

Robustness of Griffiths effects in homeostatic connectome threshold models

G. Ó. Phys. Rev. E 98 (2018) 042126

Addition of a third (refractive)
state does not destroy GP

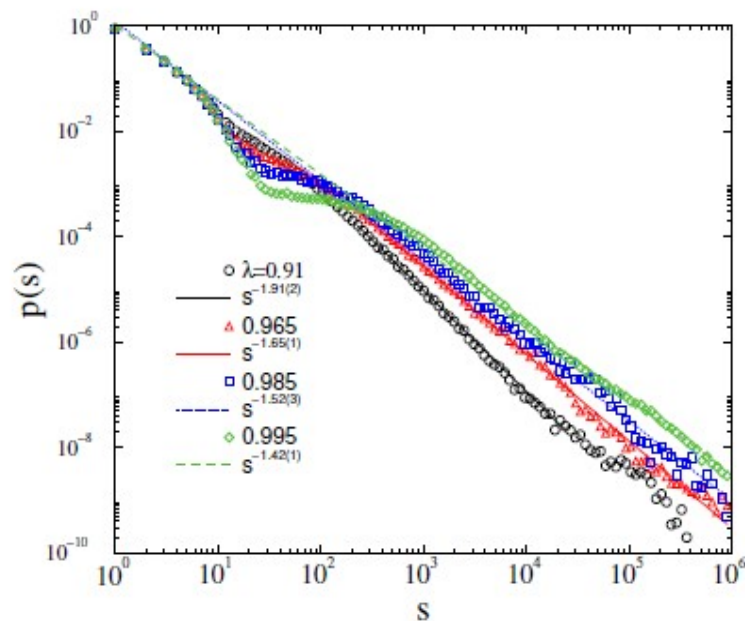


FIG. 3: Avalanche size distribution in the relative threshold model with refractory states, for $K = 0.2$, $\nu = 1$ and $\lambda = 0.91, 0.965, 0.985, 0.995$ (bottom to top symbols). Lines: PL fits for $10^2 < s < 10^5$, for these curves as shown by the legends.

Robustness of Griffiths effects in homeostatic connectome threshold models

G. Ó. Phys. Rev. E 98 (2018) 042126

Addition of a third (refractive) state does not destroy GP

Time dependent threshold model : GP shrinks, but survives for weak variations

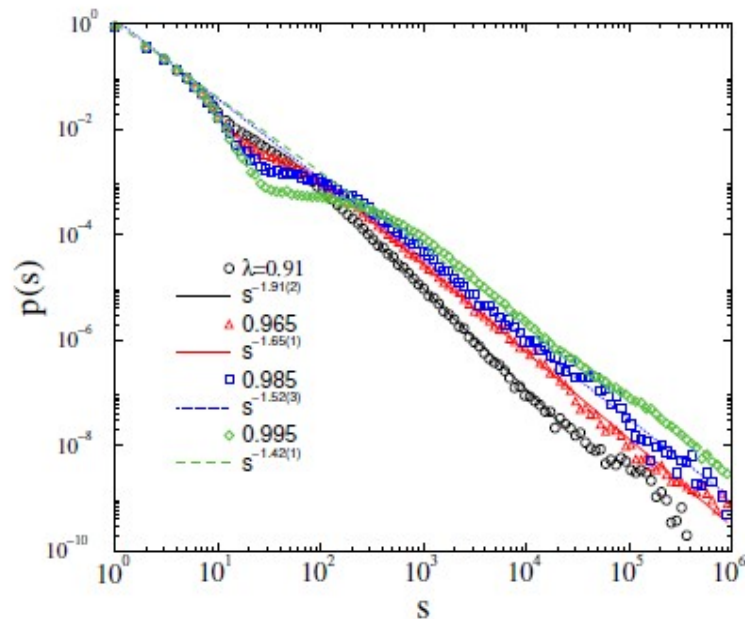


FIG. 3: Avalanche size distribution in the relative threshold model with refractory states, for $K = 0.2$, $\nu = 1$ and $\lambda = 0.91, 0.965, 0.985, 0.995$ (bottom to top symbols). Lines: PL fits for $10^2 < s < 10^5$, for these curves as shown by the legends.

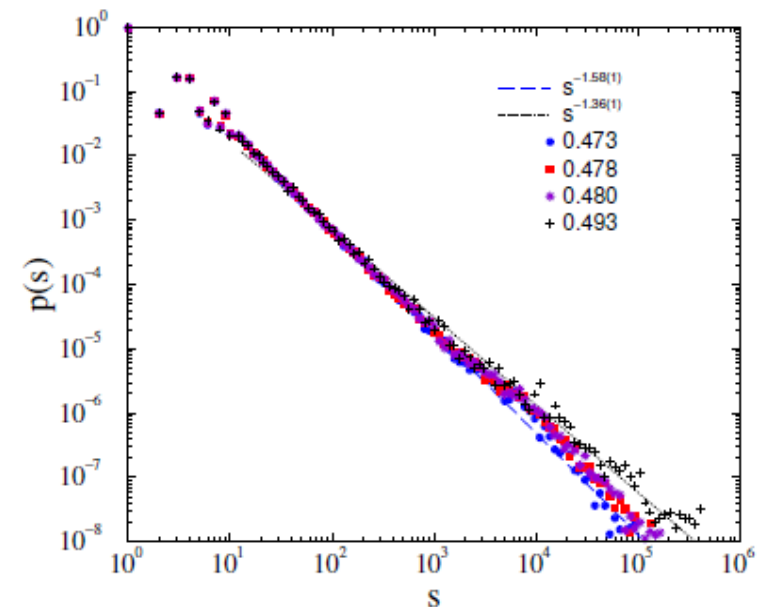
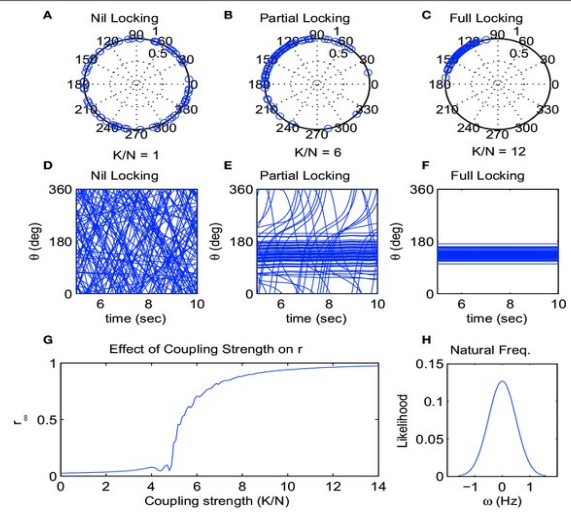
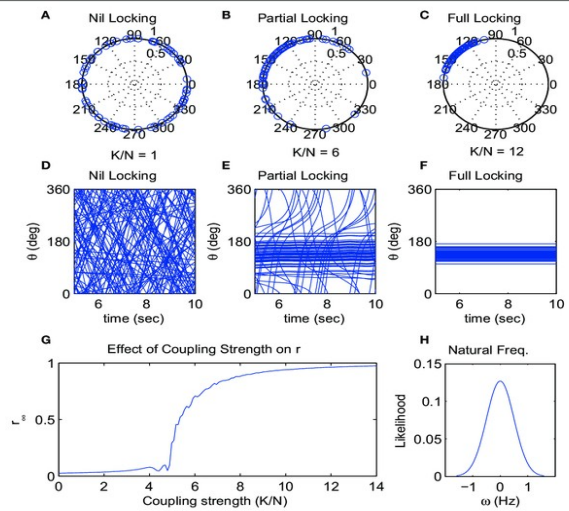


FIG. 10: Avalanche size distribution of the time dependent relative threshold model with 30% inhibitory links at $K = 0.1$, $\Delta K = 0.01$, $\nu = 0.95$ and $\lambda = 0.473, 0.478, 0.480, 0.493$ (bottom to top symbols) Dashed lines: PL fits for the tails of the $\lambda = 0.473$ and $\lambda = 0.493$ curves (bottom to top).

Kuramoto oscillator model (1975)

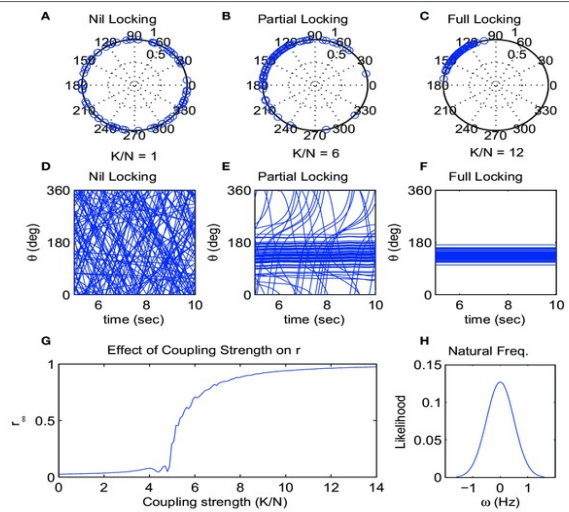


Kuramoto oscillator model (1975)



$$\dot{\theta}_i(t) = \omega_{i,0} + \frac{K}{k_i} \sum_j W_{ij} \sin[\theta_i(t) - \theta_j(t)]$$

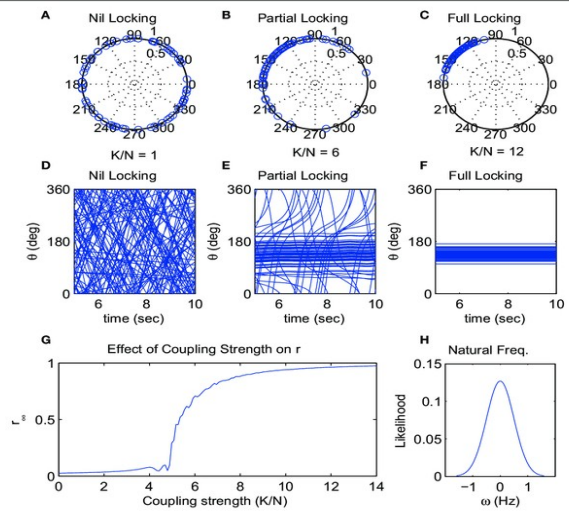
Kuramoto oscillator model (1975)



$$\dot{\theta}_i(t) = \omega_{i,0} + \frac{K}{k_i} \sum_j W_{ij} \sin[\theta_i(t) - \theta_j(t)]$$

phases $\theta_i(t)$

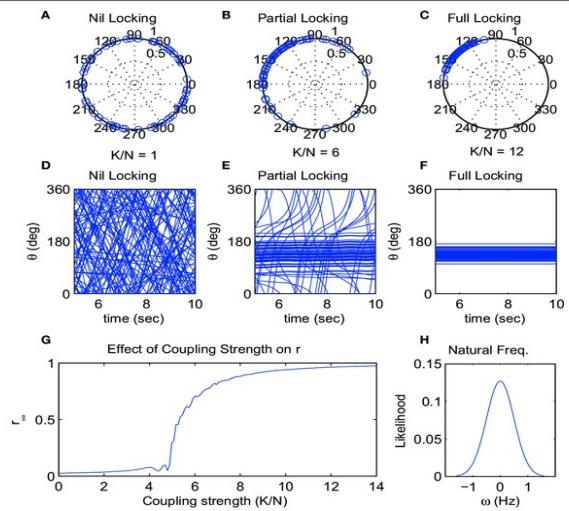
Kuramoto oscillator model (1975)



$$\dot{\theta}_i(t) = \omega_{i,0} + \frac{K}{k_i} \sum_j W_{ij} \sin[\theta_i(t) - \theta_j(t)]$$

phases $\theta_i(t)$ in-degrees k_i

Kuramoto oscillator model (1975)

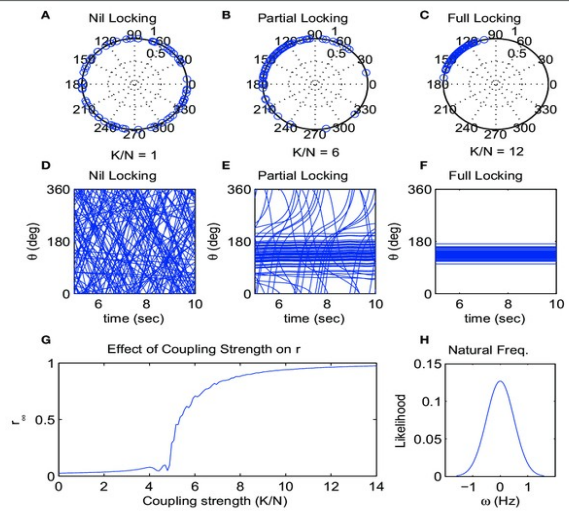


$$\dot{\theta}_i(t) = \omega_{i,0} + \frac{K}{k_i} \sum_j W_{ij} \sin[\theta_i(t) - \theta_j(t)]$$

phases $\theta_i(t)$ in-degrees k_i

global coupling K is the control parameter

Kuramoto oscillator model (1975)



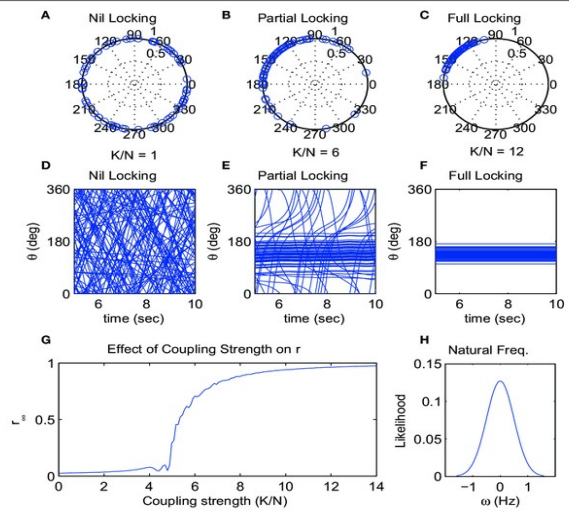
$$\dot{\theta}_i(t) = \omega_{i,0} + \frac{K}{k_i} \sum_j W_{ij} \sin[\theta_i(t) - \theta_j(t)]$$

phases $\theta_i(t)$ in-degrees k_i

global coupling K is the control parameter

weighted adjacency matrix W_{ij}

Kuramoto oscillator model (1975)



$$\dot{\theta}_i(t) = \omega_{i,0} + \frac{K}{k_i} \sum_j W_{ij} \sin[\theta_i(t) - \theta_j(t)]$$

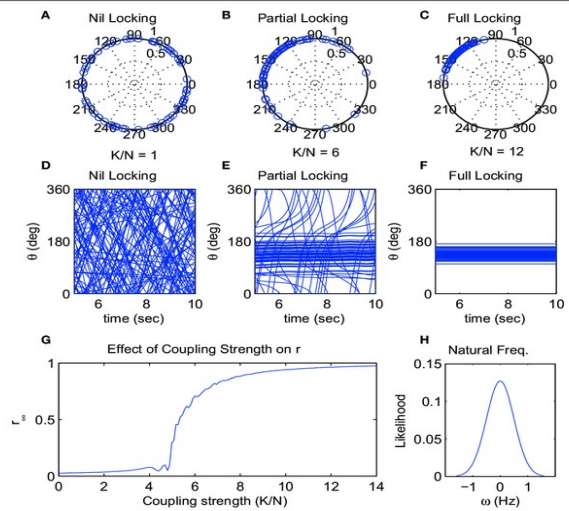
phases $\theta_i(t)$ in-degrees k_i

global coupling K is the control parameter

weighted adjacency matrix W_{ij}

$\omega_{i,0}$ is the intrinsic frequency of the i -th oscillator,

Kuramoto oscillator model (1975)



$$\dot{\theta}_i(t) = \omega_{i,0} + \frac{K}{k_i} \sum_j W_{ij} \sin[\theta_i(t) - \theta_j(t)]$$

phases $\theta_i(t)$ in-degrees k_i

global coupling K is the control parameter

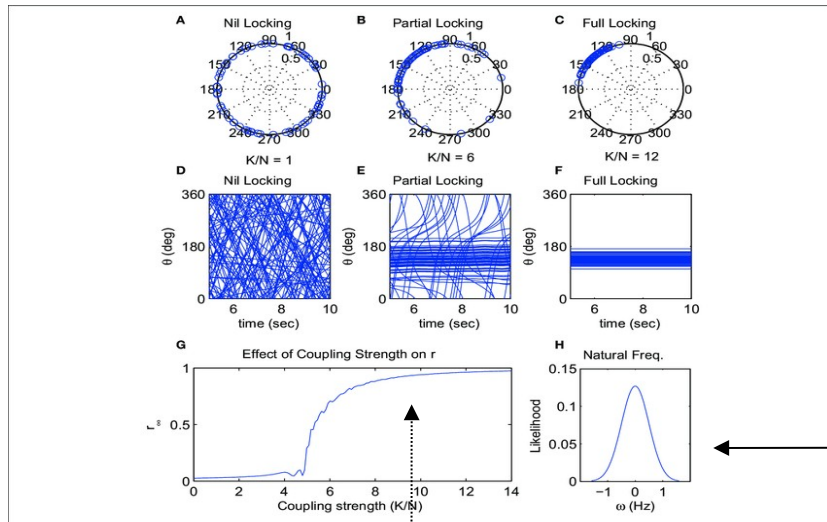
weighted adjacency matrix W_{ij}

$\omega_{i,0}$ is the intrinsic frequency of the i -th oscillator,

$$R(t) = \frac{1}{N} \left| \sum_{j=1}^N e^{i\theta_j(t)} \right|$$

Order parameter : average phase:

Kuramoto oscillator model (1975)



$$\dot{\theta}_i(t) = \omega_{i,0} + \frac{K}{k_i} \sum_j W_{ij} \sin[\theta_i(t) - \theta_j(t)]$$

phases $\theta_i(t)$ in-degrees k_i

global coupling K is the control parameter

weighted adjacency matrix W_{ij}

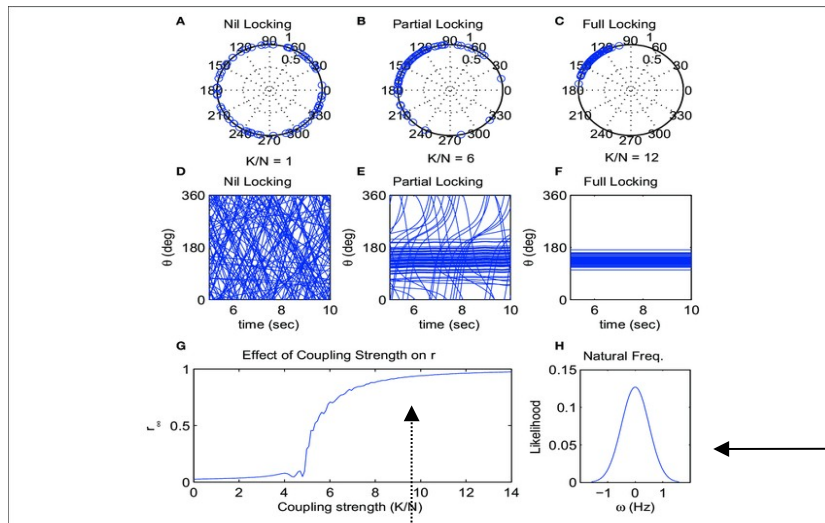
$\omega_{i,0}$ is the intrinsic frequency of the i -th oscillator,

$$R(t) = \frac{1}{N} \left| \sum_{j=1}^N e^{i\theta_j(t)} \right|$$

Order parameter : average phase:

Non-zero, above critical coupling strength $K > K_c$, tends to zero for $K \leq K_c$ as $R \propto (1/N)^{1/2}$
 or exhibits an initial growth: $R(t, N) = N^{-1/2} t^\eta f_\uparrow(t/N^z)$ for incoherent initial state

Kuramoto oscillator model (1975)



$$\dot{\theta}_i(t) = \omega_{i,0} + \frac{K}{k_i} \sum_j W_{ij} \sin[\theta_i(t) - \theta_j(t)]$$

phases $\theta_i(t)$ in-degrees k_i

global coupling K is the control parameter

weighted adjacency matrix W_{ij}

$\omega_{i,0}$ is the intrinsic frequency of the i -th oscillator,

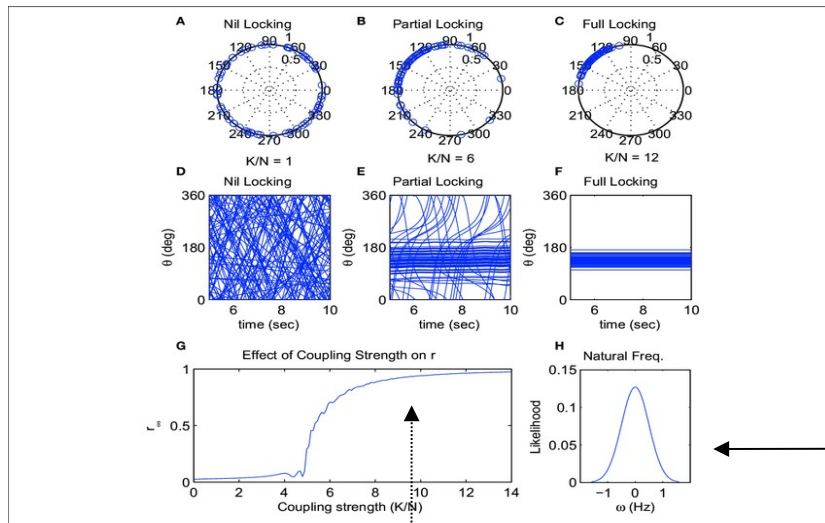
$$R(t) = \frac{1}{N} \left| \sum_{j=1}^N e^{i\theta_j(t)} \right|$$

Order parameter : average phase:

Non-zero, above critical coupling strength $K > K_c$, tends to zero for $K \leq K_c$ as $R \propto (1/N)^{1/2}$
 or exhibits an initial growth: $R(t, N) = N^{-1/2} t^\eta f_\uparrow(t/N^2)$ for incoherent initial state

Critical synchronization transition for $D > 4$ spatial dimensions,
 which is mean-field like: i.e. $D \rightarrow \infty$ (full graph)

Kuramoto oscillator model (1975)



$$\dot{\theta}_i(t) = \omega_{i,0} + \frac{K}{k_i} \sum_j W_{ij} \sin[\theta_i(t) - \theta_j(t)]$$

phases $\theta_i(t)$ in-degrees k_i

global coupling K is the control parameter

weighted adjacency matrix W_{ij}

$\omega_{i,0}$ is the intrinsic frequency of the i -th oscillator,

$$R(t) = \frac{1}{N} \left| \sum_{j=1}^N e^{i\theta_j(t)} \right|$$

Order parameter : average phase:

Non-zero, above critical coupling strength $K > K_c$, tends to zero for $K \leq K_c$ as $R \propto (1/N)^{1/2}$

or exhibits an initial growth: $R(t, N) = N^{-1/2} t^\eta f_\uparrow(t/N^2)$ for incoherent initial state

Critical synchronization transition for $D > 4$ spatial dimensions, which is mean-field like: i.e. $D \rightarrow \infty$ (full graph)

The dynamical behavior suffers very strong corrections to scaling and *chaoticity*

We use this "toy" synchronization model assuming universality,

Numerical integration of the model

Numerical integration of the model

Global synchronization measures:

Numerical integration of the model

Global synchronization measures:

$$r(t) \exp i\theta(t) = 1/N \sum_j \exp [i\theta_j(t)]$$

Numerical integration of the model

Global synchronization measures:

$$r(t) \exp i\theta(t) = 1/N \sum_j \exp [i\theta_j(t)]$$

$$R(t) = \langle r(t) \rangle$$

Numerical integration of the model

Global synchronization measures:

$$r(t) \exp i\theta(t) = 1/N \sum_j \exp [i\theta_j(t)]$$

$$R(t) = \langle r(t) \rangle$$

$$\Omega(t) = \frac{1}{N} \sum_{j=1}^N (\bar{\omega}(t) - \omega_j^2(t))$$

Numerical integration of the model

Global synchronization measures:

$$r(t) \exp i\theta(t) = 1/N \sum_j \exp [i\theta_j(t)]$$

$$R(t) = \langle r(t) \rangle$$

$$\Omega(t) = \frac{1}{N} \sum_{j=1}^N (\bar{\omega}(t) - \omega_j^2(t))$$

Local synchronization measures:

Numerical integration of the model

Global synchronization measures:

$$r(t) \exp i\theta(t) = 1/N \sum_j \exp [i\theta_j(t)]$$

$$R(t) = \langle r(t) \rangle$$

$$\Omega(t) = \frac{1}{N} \sum_{j=1}^N (\bar{\omega}(t) - \omega_j^2(t))$$

Local synchronization measures:

$$R_i(t) = \frac{1}{N_{i.\text{neigh}}} \left| \sum_j^{N_{i.\text{neigh}}} A_{ij} e^{i\theta_j(t)} \right|$$

Numerical integration of the model

Global synchronization measures:

$$r(t) \exp i\theta(t) = 1/N \sum_j \exp [i\theta_j(t)]$$

$$R(t) = \langle r(t) \rangle$$

$$\Omega(t) = \frac{1}{N} \sum_{j=1}^N (\bar{\omega}(t) - \omega_j^2(t))$$

Local synchronization measures:

$$R_i(t) = \frac{1}{N_{i.\text{neigh}}} \left| \sum_j^{N_{i.\text{neigh}}} A_{ij} e^{i\theta_j(t)} \right|$$

$$\Omega_i(t) = \frac{1}{N_{i.\text{neigh}}} \left| \sum_j^{N_{i.\text{neigh}}} (\bar{\omega}(t) - \omega_j(t))^2 \right|$$

Numerical integration of the model

Global synchronization measures:

$$r(t) \exp i\theta(t) = 1/N \sum_j \exp [i\theta_j(t)]$$

$$R(t) = \langle r(t) \rangle$$

$$\Omega(t) = \frac{1}{N} \sum_{j=1}^N (\bar{\omega}(t) - \omega_j^2(t))$$

Local synchronization measures:

$$R_i(t) = \frac{1}{N_{i.\text{neigh}}} \left| \sum_j^{N_{i.\text{neigh}}} A_{ij} e^{i\theta_j(t)} \right| \quad \Omega_i(t) = \frac{1}{N_{i.\text{neigh}}} \left| \sum_j^{N_{i.\text{neigh}}} (\bar{\omega}(t) - \omega_j(t))^2 \right|$$

Hurst (phase) and beta exponent analysis of local order parameters

Numerical integration of the model

Global synchronization measures:

$$r(t) \exp i\theta(t) = 1/N \sum_j \exp [i\theta_j(t)]$$

$$R(t) = \langle r(t) \rangle$$

$$\Omega(t) = \frac{1}{N} \sum_{j=1}^N (\bar{\omega}(t) - \omega_j^2(t))$$

Local synchronization measures:

$$R_i(t) = \frac{1}{N_{i.\text{neigh}}} \left| \sum_j^{N_{i.\text{neigh}}} A_{ij} e^{i\theta_j(t)} \right| \quad \Omega_i(t) = \frac{1}{N_{i.\text{neigh}}} \left| \sum_j^{N_{i.\text{neigh}}} (\bar{\omega}(t) - \omega_j(t))^2 \right|$$

Hurst (phase) and beta exponent analysis of local order parameters

$$\mathbb{E} \left[\frac{Z(n)}{S(n)} \right] = Cn^H,$$

Numerical integration of the model

Global synchronization measures:

$$r(t) \exp i\theta(t) = 1/N \sum_j \exp [i\theta_j(t)]$$

$$R(t) = \langle r(t) \rangle$$

$$\Omega(t) = \frac{1}{N} \sum_{j=1}^N (\bar{\omega}(t) - \omega_j^2(t))$$

Local synchronization measures:

$$R_i(t) = \frac{1}{N_{i.\text{neigh}}} \left| \sum_j^{N_{i.\text{neigh}}} A_{ij} e^{i\theta_j(t)} \right| \quad \Omega_i(t) = \frac{1}{N_{i.\text{neigh}}} \left| \sum_j^{N_{i.\text{neigh}}} (\bar{\omega}(t) - \omega_j(t))^2 \right|$$

Hurst (phase) and beta exponent analysis of local order parameters

$$\mathbb{E} \left[\frac{Z(n)}{S(n)} \right] = Cn^H$$

$$S(f) = \left| \sum_{j=0}^N \Omega_j(t) e^{-2\pi i f_j / N} \right|^2 \approx 1/f^\beta$$

Numerical integration of the model

Global synchronization measures:

$$r(t) \exp i\theta(t) = 1/N \sum_j \exp [i\theta_j(t)]$$

$$R(t) = \langle r(t) \rangle$$

$$\Omega(t) = \frac{1}{N} \sum_{j=1}^N (\bar{\omega}(t) - \omega_j^2(t))$$

Local synchronization measures:

$$R_i(t) = \frac{1}{N_{i.\text{neigh}}} \left| \sum_j^{N_{i.\text{neigh}}} A_{ij} e^{i\theta_j(t)} \right| \quad \Omega_i(t) = \frac{1}{N_{i.\text{neigh}}} \left| \sum_j^{N_{i.\text{neigh}}} (\bar{\omega}(t) - \omega_j(t))^2 \right|$$

Hurst (phase) and beta exponent analysis of local order parameters

$$\mathbb{E} \left[\frac{Z(n)}{S(n)} \right] = Cn^H$$

$$S(f) = \left| \sum_{j=0}^N \Omega_j(t) e^{-2\pi i f_j / N} \right|^2 \approx 1/f^\beta$$

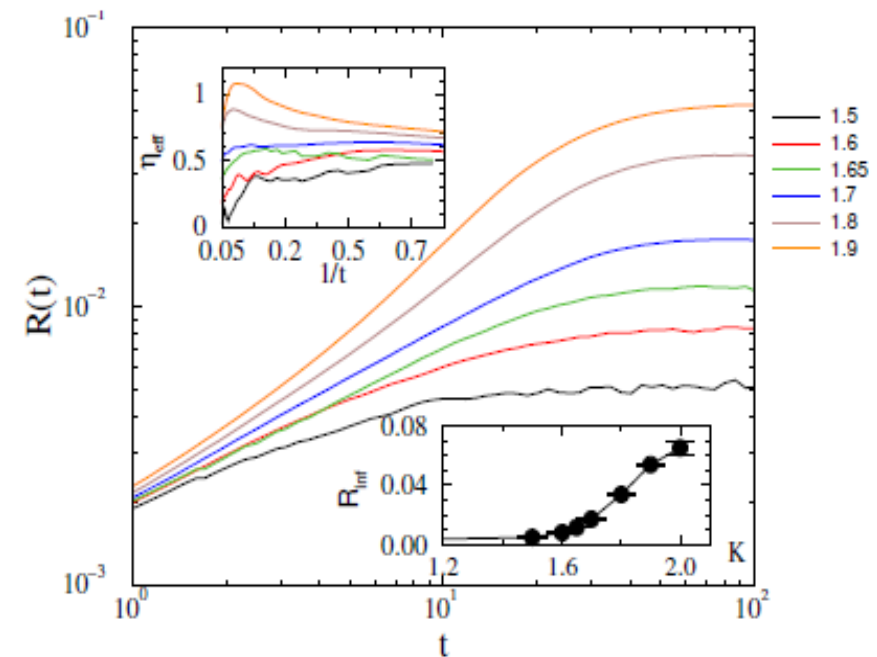
Numerical ODE solution of large set of equations via adaptive

Bulirsch-Stoer stepper, implemented on HPC GPU-s

Kuramoto solution for the *KKI-18* graph with
N = 836 733 nodes and 41 523 931 weighted edges

Kuramoto solution for the *KKI-18* graph with $N= 836\ 733$ nodes and $41\ 523\ 931$ weighted edges

The synchronization transition point determined by growth as before



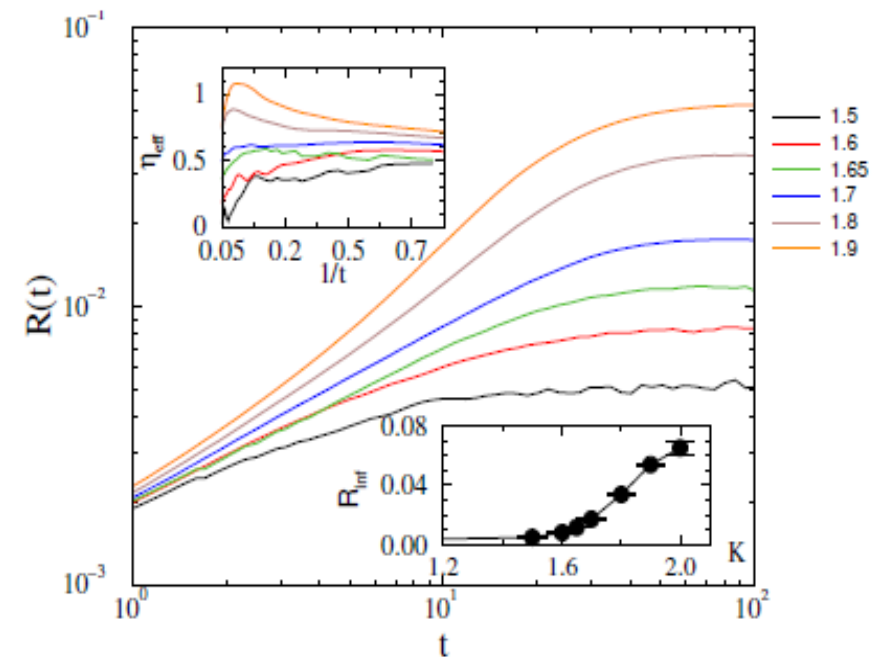
Kuramoto solution for the *KKI-18* graph with $N = 836\,733$ nodes and $41\,523\,931$ weighted edges

The synchronization transition point

determined by growth as before

KKI-18 has $D = 3.05 < 4 \rightarrow$

No real phase transition, crossover



Kuramoto solution for the *KKI-18* graph with $N = 836\,733$ nodes and $41\,523\,931$ weighted edges

The synchronization transition point

determined by growth as before

KKI-18 has $D = 3.05 < 4 \rightarrow$

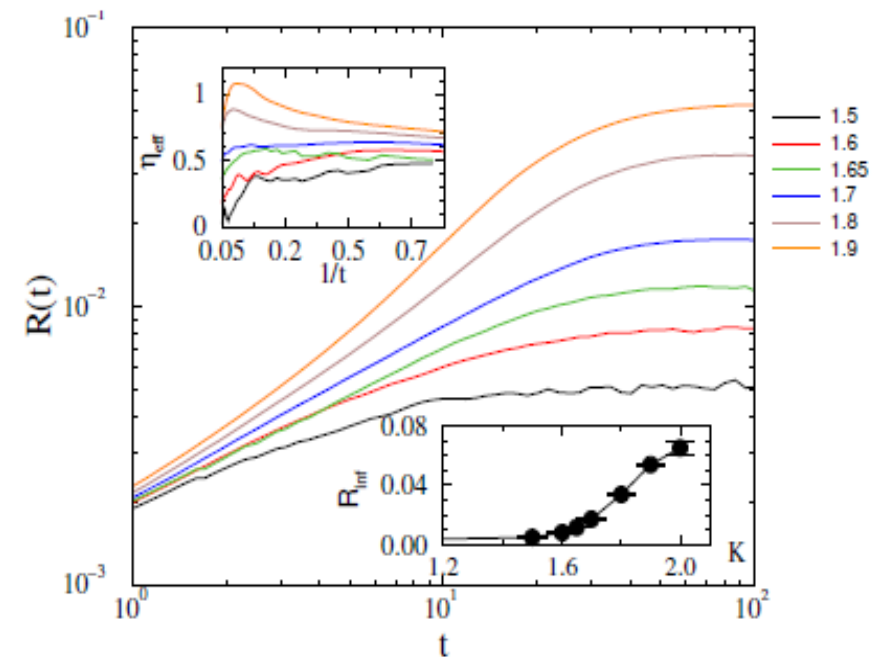
No real phase transition, crossover

Due to the fat-tailed link weight

distribution, incoming weight

normalization is applied:

$$W'_{i,j} = W_{i,j} / \sum_{j \in \text{neighb. of } i} W_{i,j}$$



Kuramoto solution for the *KKI-18* graph with $N= 836\ 733$ nodes and $41\ 523\ 931$ weighted edges

The synchronization transition point

determined by growth as before

KKI-18 has $D = 3.05 < 4 \rightarrow$

No real phase transition, crossover

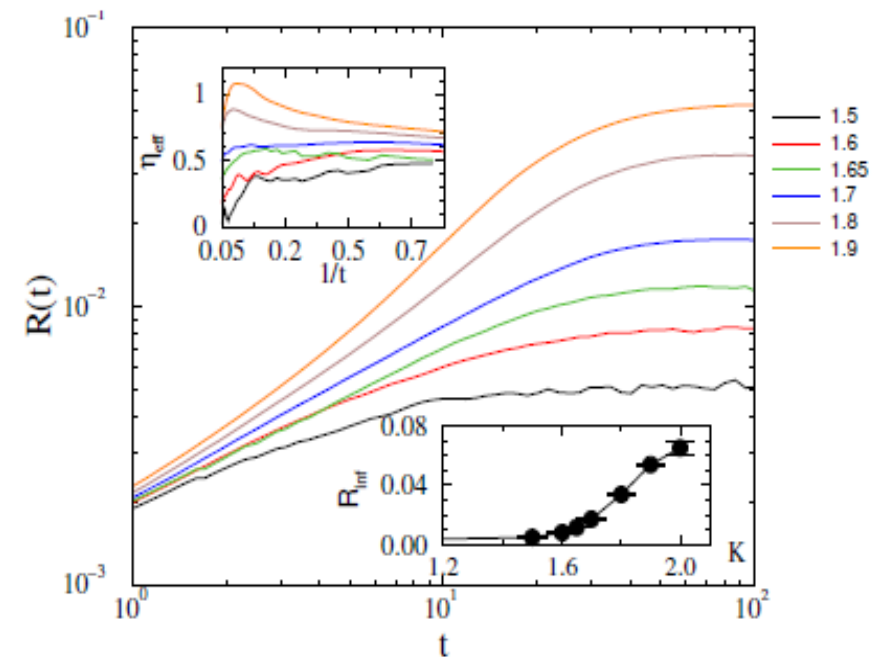
Due to the fat-tailed link weight

distribution, incoming weight

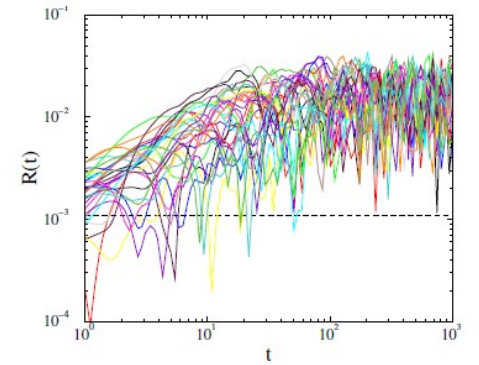
normalization is applied:

$$W'_{i,j} = W_{i,j} / \sum_{j \in \text{neighb. of } i} W_{i,j}$$

$K_c = 1.7$ and growth exponent: $\eta = 0.6(1)$

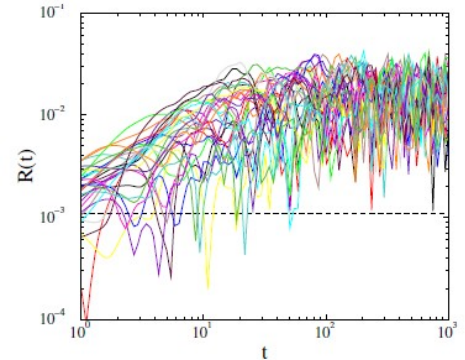


Duration distribution for the KKI-18 graph



Duration distribution for the KKI-18 graph

Measure characteristic times t_x of first
dip below: $R_c = (1/N)^{1/2}$

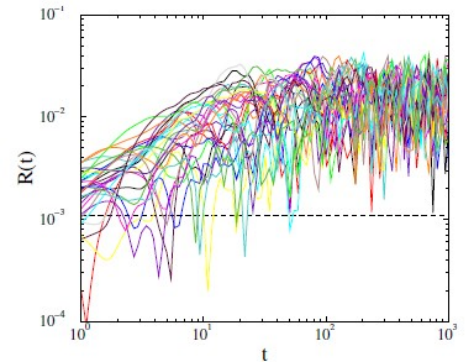


Duration distribution for the KKI-18 graph

Measure characteristic times t_x of first

dip below: $R_c = (1/N)^{1/2}$

average over: *10.000* independent ω_i
realizations



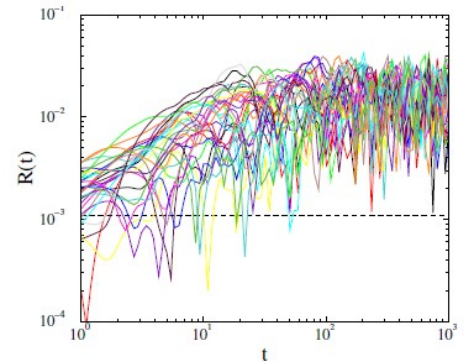
Duration distribution for the KKI-18 graph

Measure characteristic times t_x of first

dip below: $R_c = (1/N)^{1/2}$

average over: 10.000 independent ω_i
realizations

Histogramming of t_x at the critical point



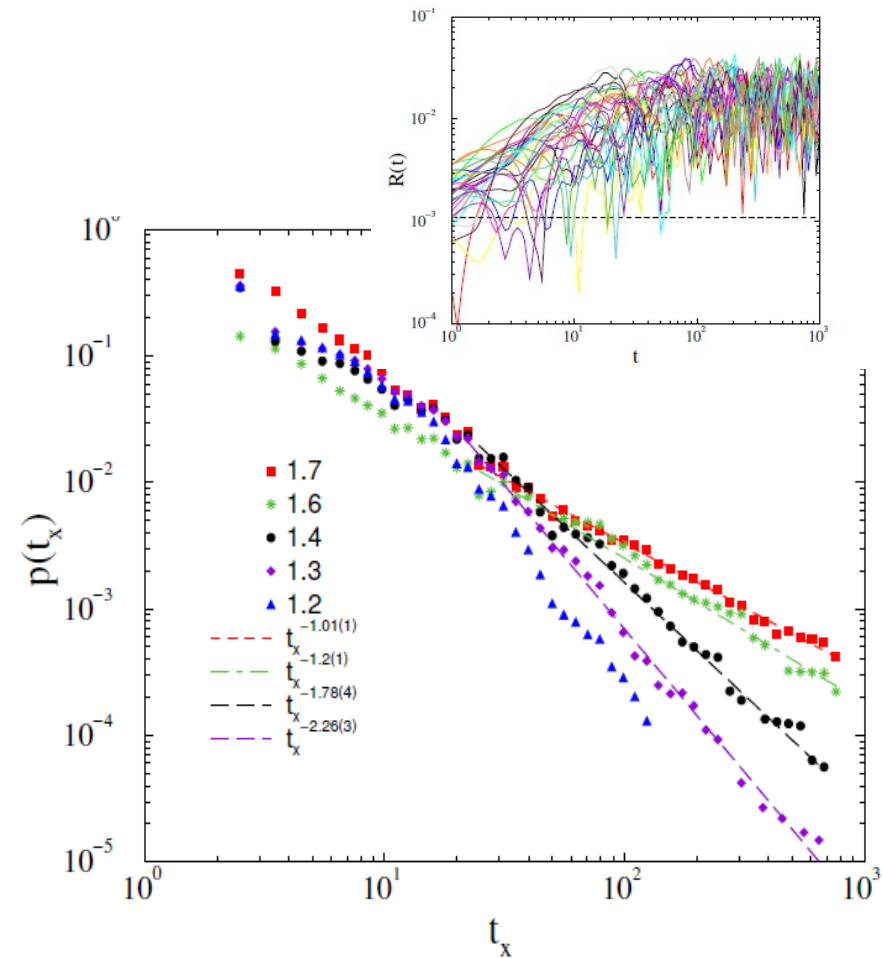
Duration distribution for the KKI-18 graph

Measure characteristic times t_x of first

dip below: $R_c = (1/N)^{1/2}$

average over: 10.000 independent ω_i
realizations

Histogramming of t_x at the critical point



Duration distribution for the KKI-18 graph

Measure characteristic times t_x of first

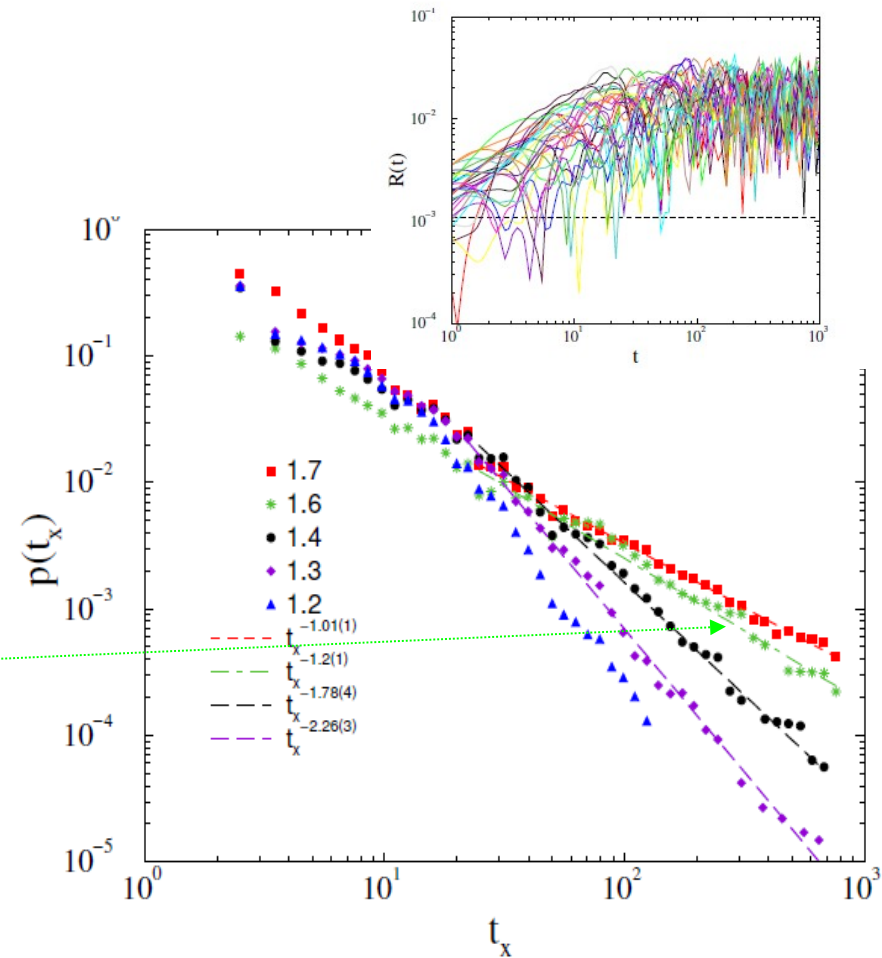
dip below: $R_c = (1/N)^{1/2}$

average over: 10.000 independent ω_i
realizations

Histogramming of t_x at the critical point

Critical exponent: $\tau_t = 1.2$ (1)

obtained by fitting for the PL tails



Duration distribution for the KKI-18 graph

Measure characteristic times t_x of first dip below: $R_c = (1/N)^{1/2}$

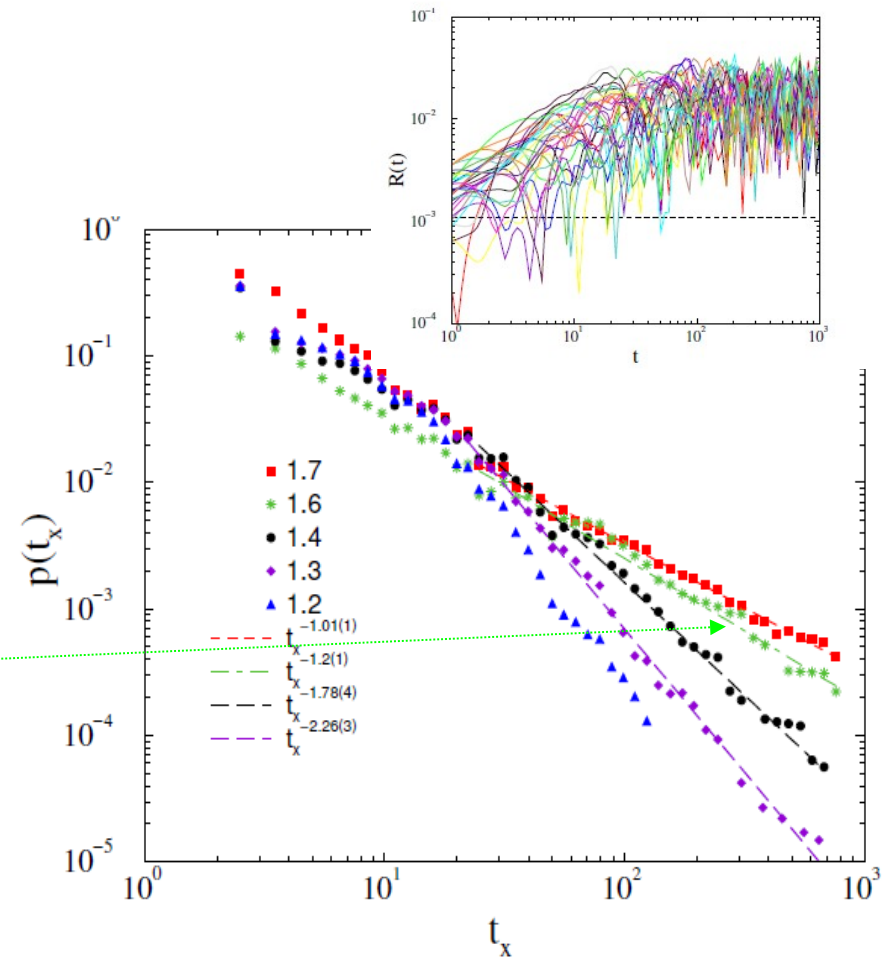
average over: 10.000 independent ω_i realizations

Histogramming of t_x at the critical point

Critical exponent: $\tau_t = 1.2$ (1)

obtained by fitting for the PL tails

Below the transition point : $K < 1.6$
non-universal power laws in the range
of experiments of activity durations :
 $1.5 < \tau_t < 2.4$ (LRTC *Palva et al 2013*)



Inhibitory (negative) links compared to experiments

Inhibitions: 5% of links: $w_{ij} \rightarrow -w_{ij}$ randomly

Inhibitory (negative) links compared to experiments

Inhibitions: 5% of links: $w_{ij} \rightarrow -w_{ij}$ randomly

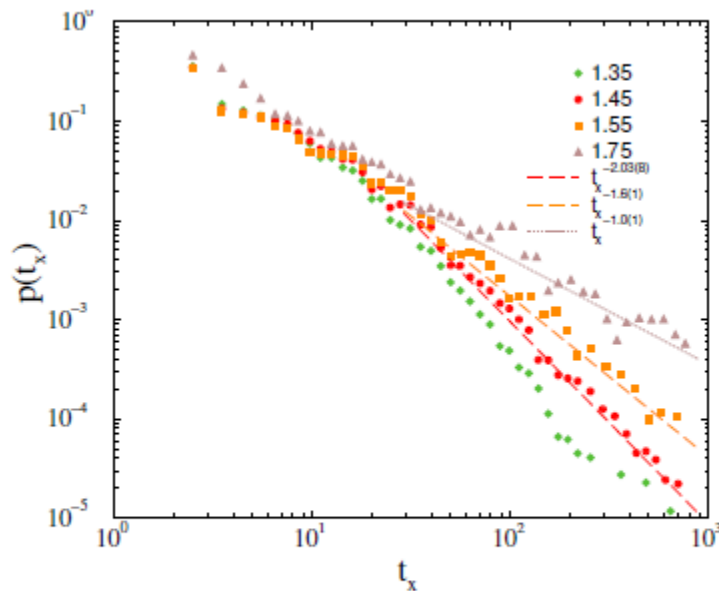


Figure 9. Duration distribution of t_x on the *KKI-18-I* model in case of 5% inhibitory node assumption for $K = 1.35$ (+), $K = 1.45$ (bullets), 1.55 (boxes), 1.75 (triangles). The dashed line shows PL fits to the tail region: $t_x > 20$.

Inhibitory (negative) links compared to experiments

Inhibitions: 5% of links: $w_{ij} \rightarrow -w_{ij}$ randomly

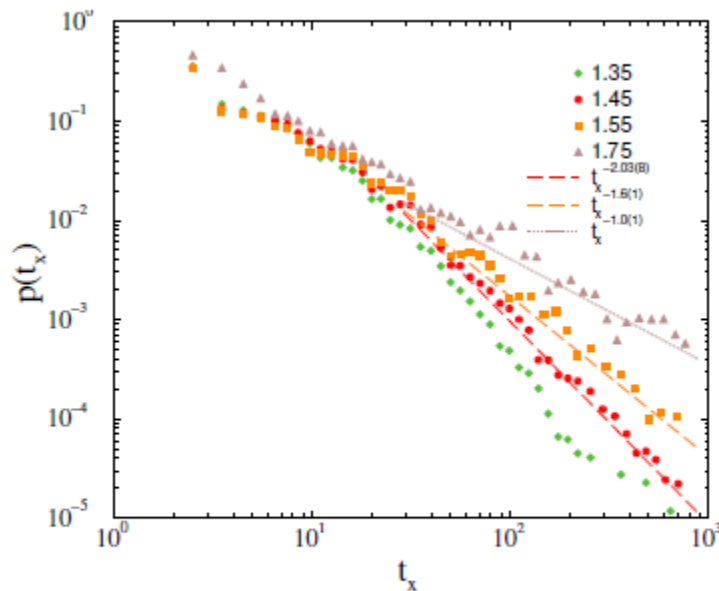


Figure 9. Duration distribution of t_x on the *KKI-18-I* model in case of 5% inhibitory node assumption for $K = 1.35$ (+), $K = 1.45$ (bullets), 1.55 (boxes), 1.75 (triangles). The dashed line shows PL fits to the tail region: $t_x > 20$.

$K_c = 1.7(1)$ and $\eta = 0.6(1)$ remains the same. Sub-critically:

Duration scaling exponent within experimental range: $1.5 < \tau_t < 2.4$
J.M. Palva et al PNAS 110 (2013) 3585

Invariance of Kuramoto with respect to the ω_i distribution

$$\dot{\theta}_i(t) = \omega_{i,0} + \frac{K}{k_i} \sum_j W_{ij} \sin[\theta_i(t) - \theta_j(t)]$$

Invariance of Kuramoto with respect to the ω_i distribution

Brain experiments: $\omega_i > 0$

$$\dot{\theta}_i(t) = \omega_{i,0} + \frac{K}{k_i} \sum_j W_{ij} \sin[\theta_i(t) - \theta_j(t)]$$

Invariance of Kuramoto with respect to the ω_i distribution

Brain experiments: $\omega_i > 0$

distributions are narrow: $\sigma_i \sim 0.02$

$$\dot{\theta}_i(t) = \omega_{i,0} + \frac{K}{k_i} \sum_j W_{ij} \sin[\theta_i(t) - \theta_j(t)]$$

Invariance of Kuramoto with respect to the ω_i distribution

Brain experiments: $\omega_i > 0$

distributions are narrow: $\sigma_i \sim 0.02$

and have mean value: $\langle \omega_i \rangle \sim 0.05$

$$\dot{\theta}_i(t) = \omega_{i,0} + \frac{K}{k_i} \sum_j W_{ij} \sin[\theta_i(t) - \theta_j(t)]$$

Invariance of Kuramoto with respect to the ω_i distribution

Brain experiments: $\omega_i > 0$

distributions are narrow: $\sigma_i \sim 0.02$

and have mean value: $\langle \omega_i \rangle \sim 0.05$

$$\dot{\theta}_i(t) = \omega_{i,0} + \frac{K}{k_i} \sum_j W_{ij} \sin[\theta_i(t) - \theta_j(t)]$$

$\langle \omega_i \rangle \neq 0$ can be gauged out by a rotating coordinate system

Invariance of Kuramoto with respect to the ω_i distribution

Brain experiments: $\omega_i > 0$

distributions are narrow: $\sigma_i \sim 0.02$

and have mean value: $\langle \omega_i \rangle \sim 0.05$

$$\dot{\theta}_i(t) = \omega_{i,0} + \frac{K}{k_i} \sum_j W_{ij} \sin[\theta_i(t) - \theta_j(t)]$$

$\langle \omega_i \rangle \neq 0$ can be gauged out by a rotating coordinate system

Rescaling of ω_i as : $\omega_i \rightarrow a\omega_i'$ $t \rightarrow (1/a)t'$ $K \rightarrow aK'$

Invariance of Kuramoto with respect to the ω_i distribution

Brain experiments: $\omega_i > 0$

distributions are narrow: $\sigma_i \sim 0.02$

and have mean value: $\langle \omega_i \rangle \sim 0.05$

$$\dot{\theta}_i(t) = \omega_{i,0} + \frac{K}{k_i} \sum_j W_{ij} \sin[\theta_i(t) - \theta_j(t)]$$

$\langle \omega_i \rangle \neq 0$ can be gauged out by a rotating coordinate system

Rescaling of ω_i as : $\omega_i \rightarrow a\omega_i'$ $t \rightarrow (1/a)t'$ $K \rightarrow aK'$

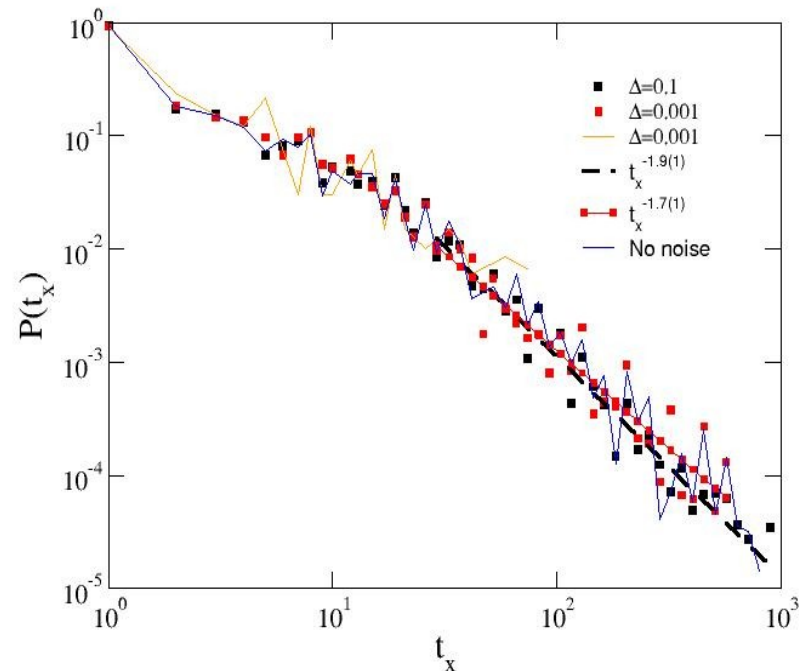
The results can be transformed for later times and weaker couplings

The effect of additive stochastic noise

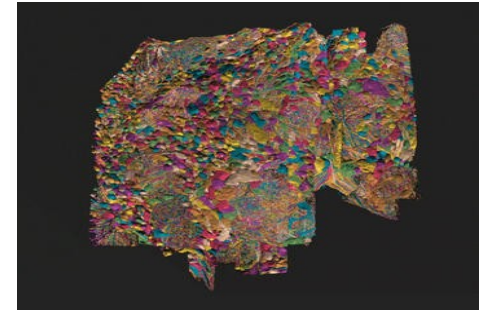
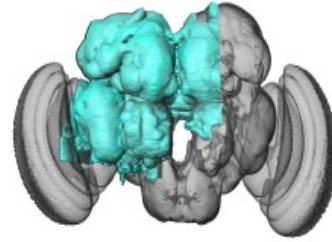
Gaussian distributed annealed noise is added:

$$\dot{\theta}_i(t) = \omega_{i,0} + \frac{K}{k_i} \sum_j W_{ij} \sin[\theta_j(t) - \theta_i(t)] + s\xi(i)$$

Negligible effect:

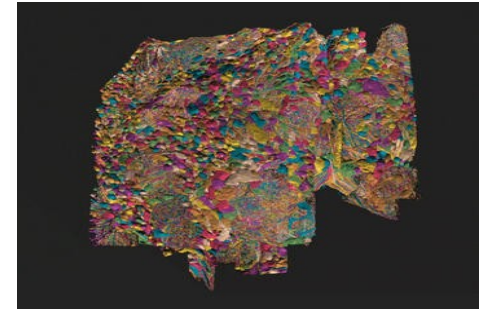
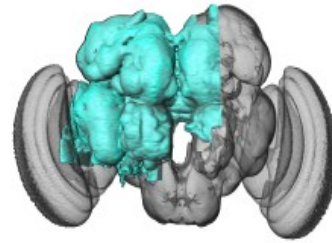


Comparison with the fruit-fly connectome results



A_{ij}

Comparison with the fruit-fly connectome results

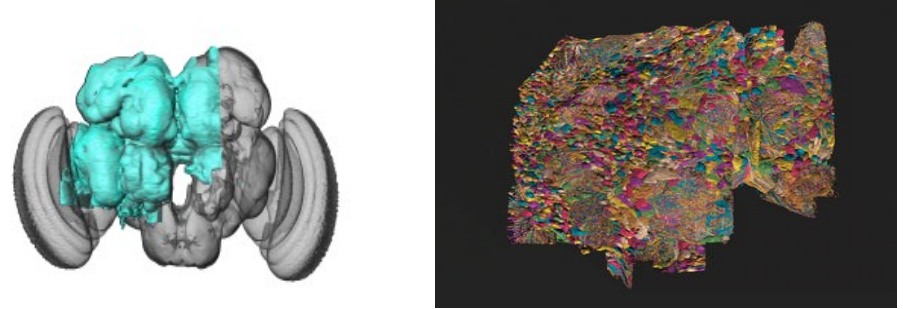
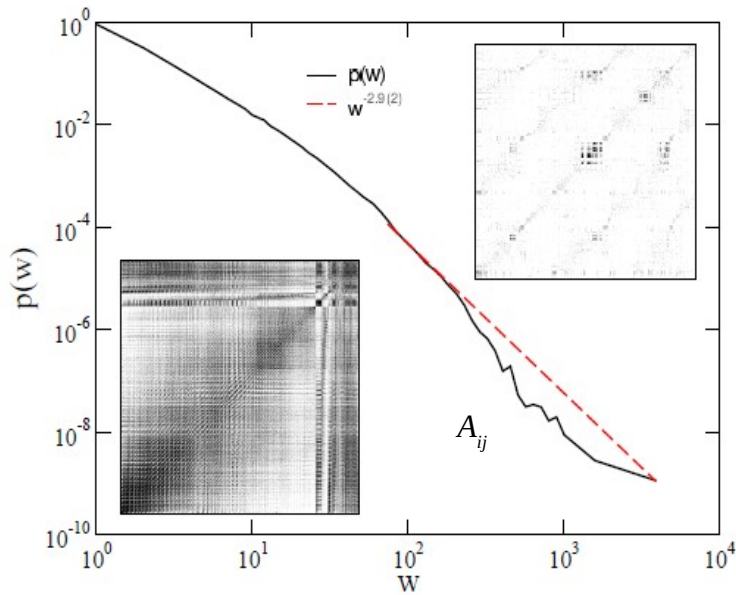


A_{ij}

Fruit-fly connectome is the largest exactly known neural network:

$$N = 21.615, L = 3.410.247$$

Comparison with the fruit-fly connectome results

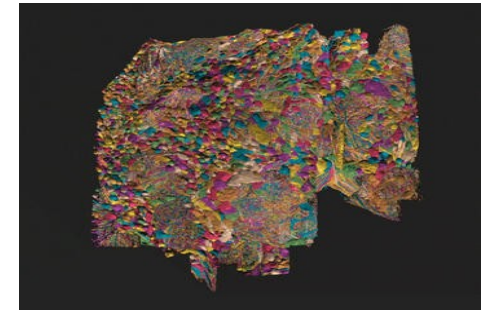
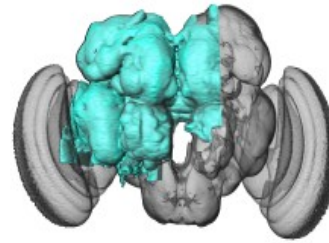
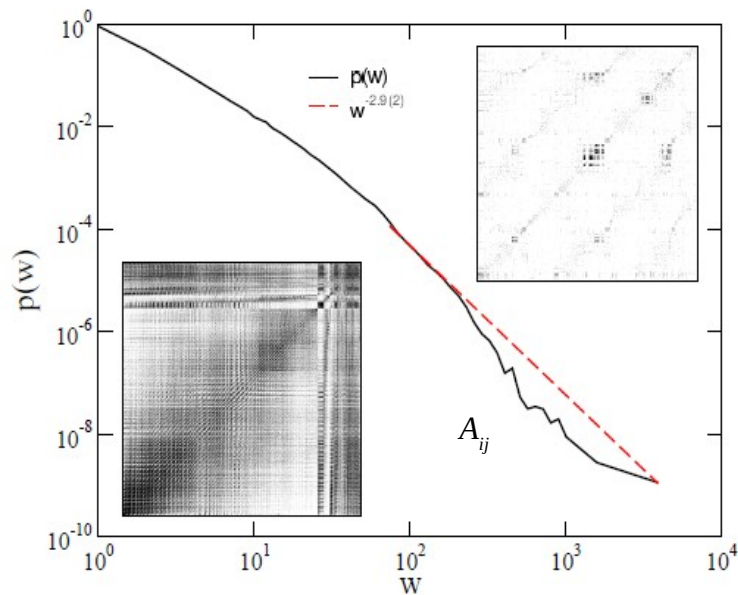


Fruit-fly connectome is the largest exactly known neural network:

$$N = 21.615, L = 3.410.247$$

Similar to random Erdős-Rényi (ER) graph, but power-law tailed connection weights

Comparison with the fruit-fly connectome results



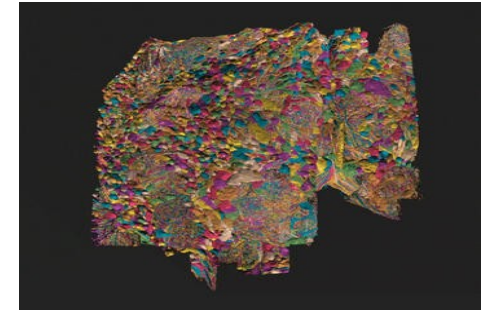
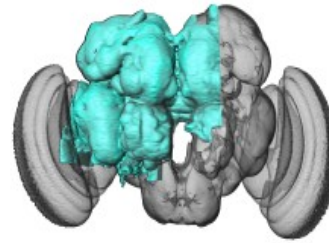
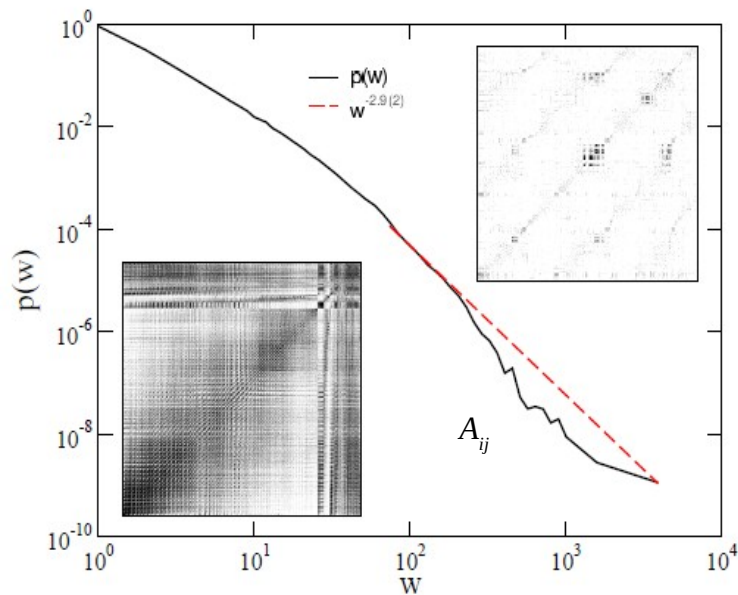
Fruit-fly connectome is the largest exactly known neural network:

$$N = 21.615, L = 3.410.247$$

Similar to random Erdős-Rényi (ER) graph, but power-law tailed connection weights

Weakly modular: $Q_{FF} \ll Q_{KKI-18}$

Comparison with the fruit-fly connectome results



Fruit-fly connectome is the largest exactly known neural network:

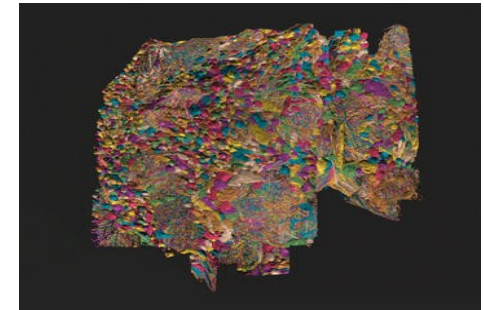
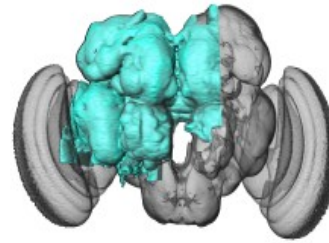
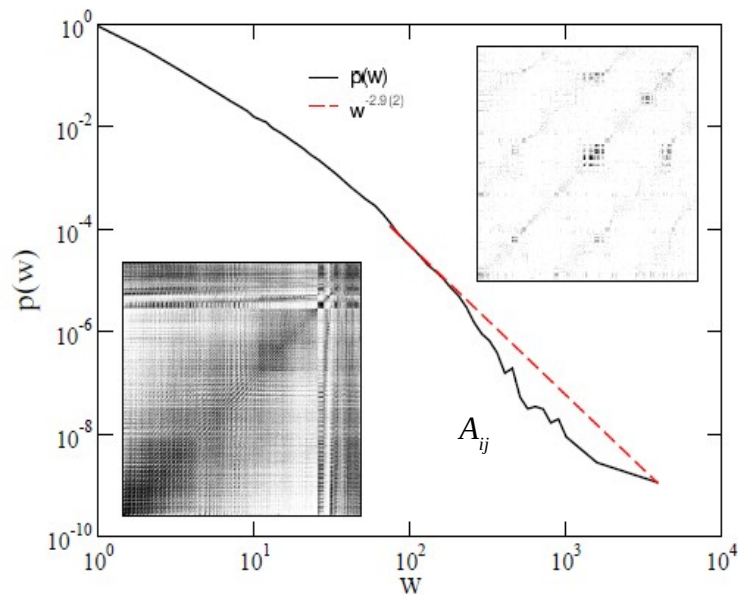
$$N = 21.615, L = 3.410.247$$

Similar to random Erdős-Rényi (ER) graph, but power-law tailed connection weights

Weakly modular: $Q_{FF} \ll Q_{KKI-18}$

Synchronization transition via $R(t)$
 local slopes : $\eta = -d \ln R / d \ln t$

Comparison with the fruit-fly connectome results



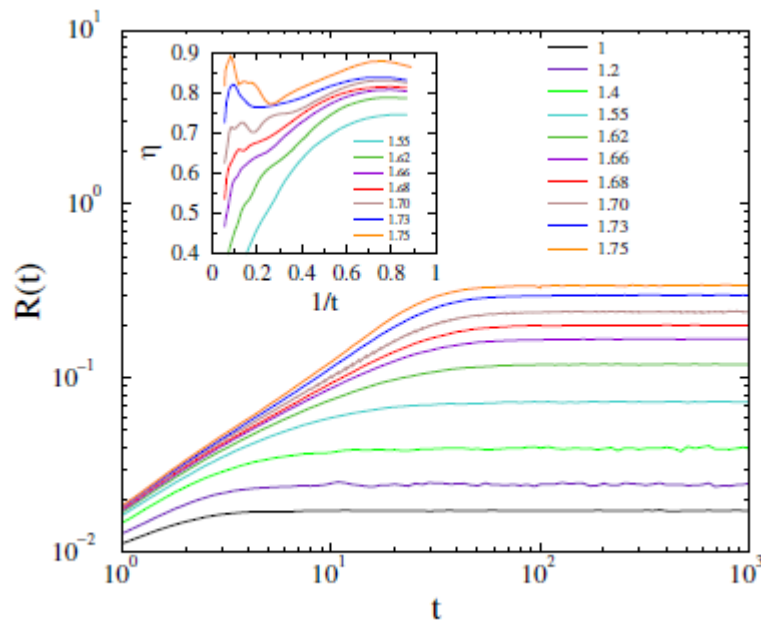
Fruit-fly connectome is the largest exactly known neural network:

$$N = 21.615, L = 3.410.247$$

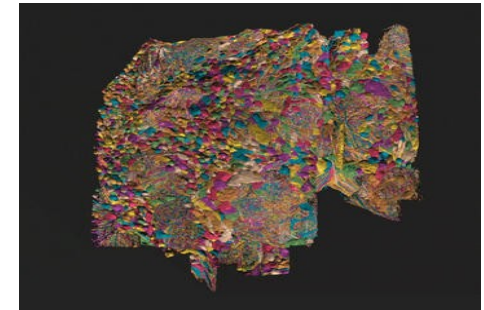
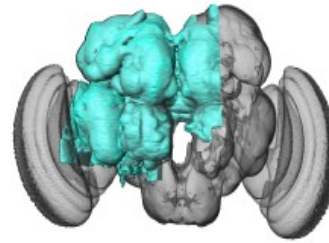
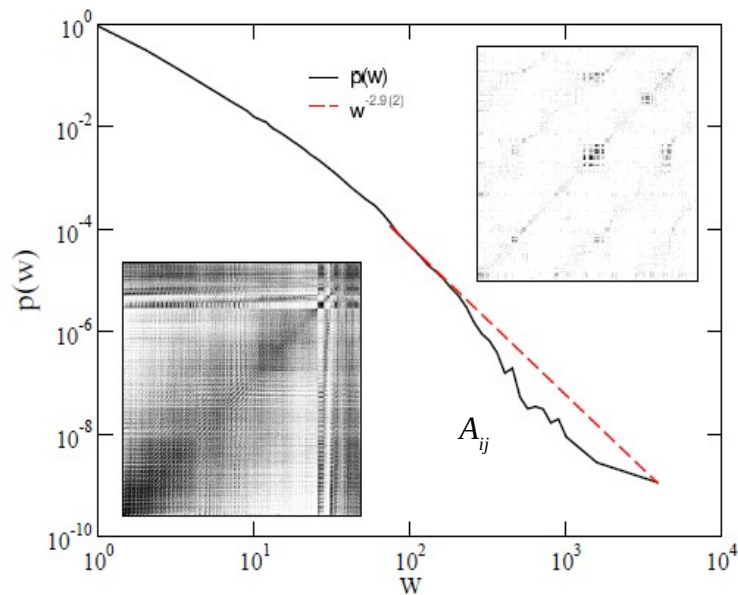
Similar to random Erdős-Rényi (ER) graph, but power-law tailed connection weights

Weakly modular: $Q_{FF} \ll Q_{KKI-18}$

Synchronizatiion transition via $R(t)$
local slopes : $\eta = -d \ln R / d \ln t$



Comparison with the fruit-fly connectome results



Fruit-fly connectome is the largest exactly known neural network:

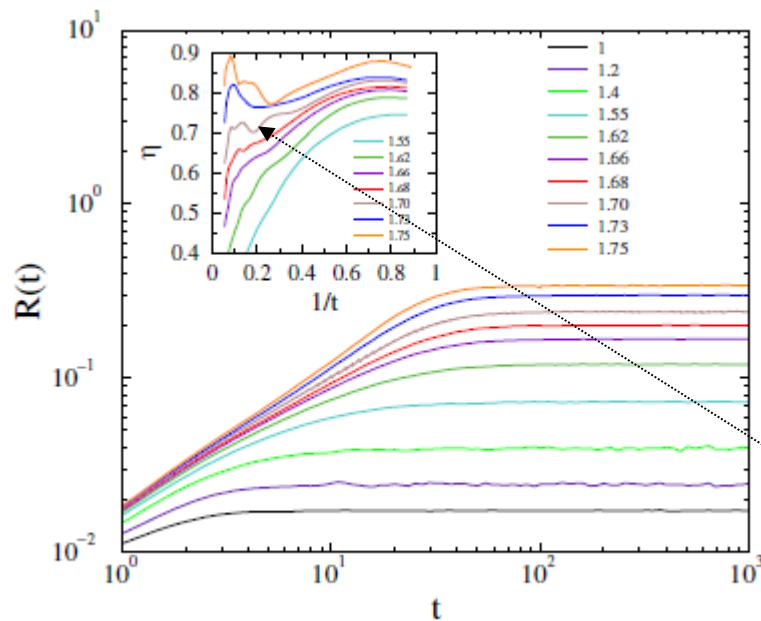
$$N = 21.615, L = 3.410.247$$

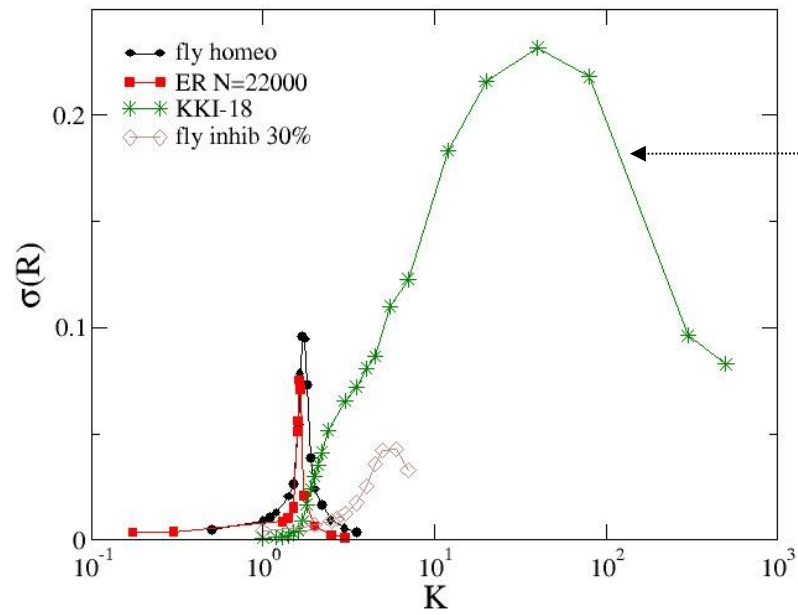
Similar to random Erdős-Rényi (ER) graph, but power-law tailed connection weights

Weakly modular: $Q_{FF} \ll Q_{KKI-18}$

Synchronization transition via $R(t)$
local slopes : $\eta = -d \ln R / d \ln t$

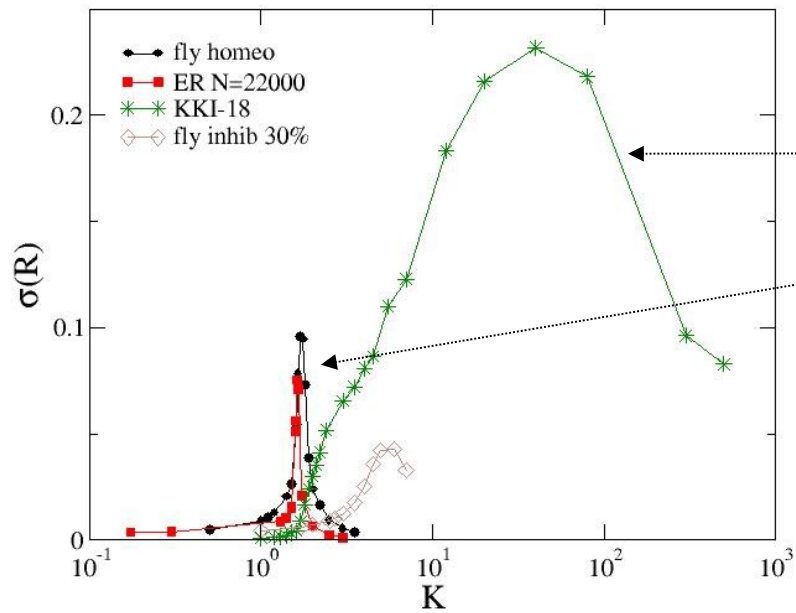
$K_c = 1.60(1)$ (inflexion curve)
Characterized by mean-field growth
Exponent $\eta = 0.7(1)$





Fluctuations of R show

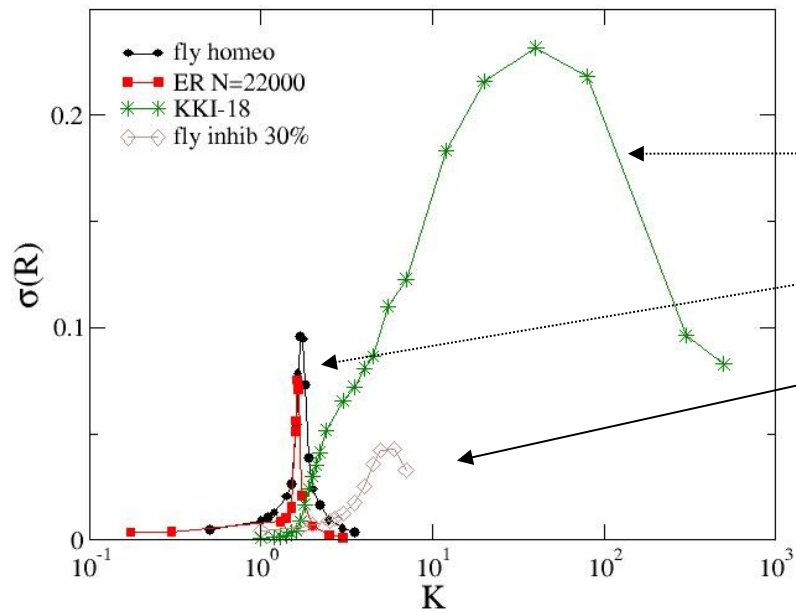
extended transition for KKI-18



Fluctuations of R show

extended transition for KKI-18

For FF ~ ER like distro

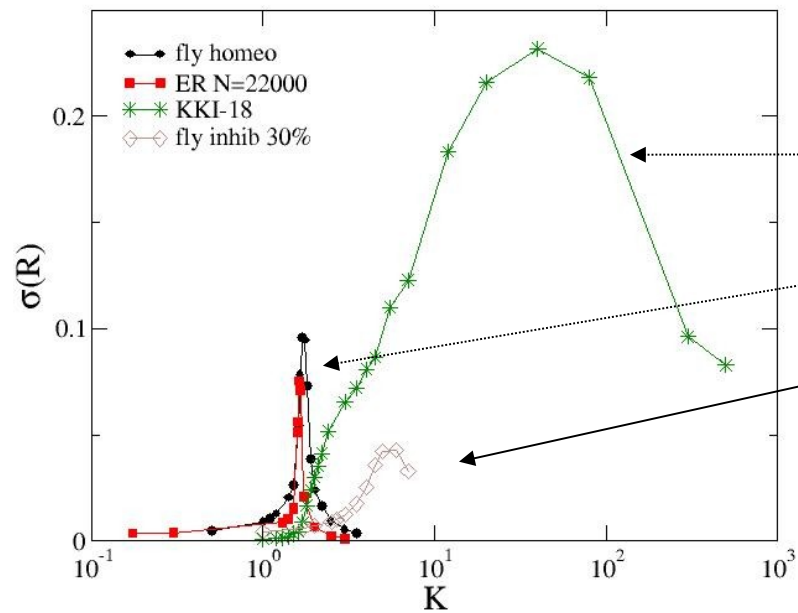


Fluctuations of R show

extended transition for KKI-18

For FF ~ ER like distro

With random inhibitors: wider range



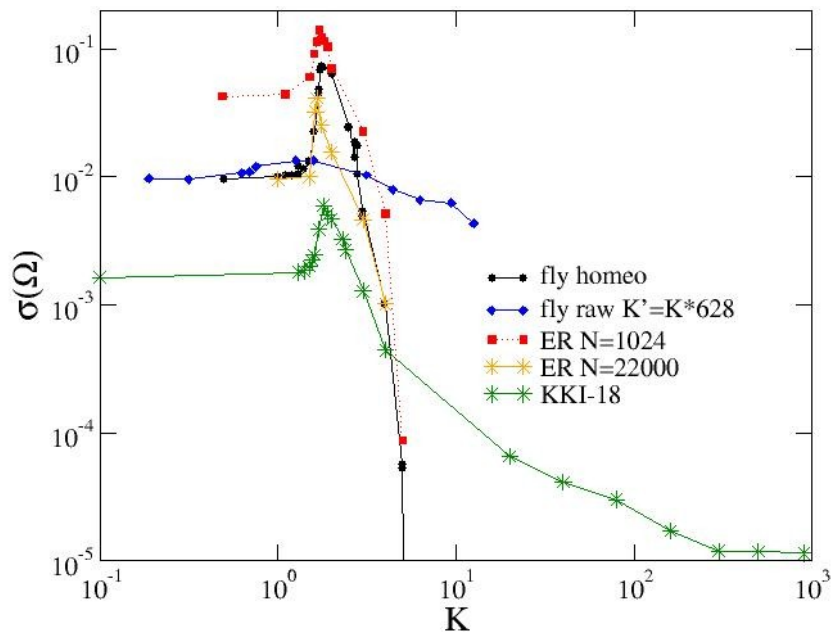
Fluctuations of R show

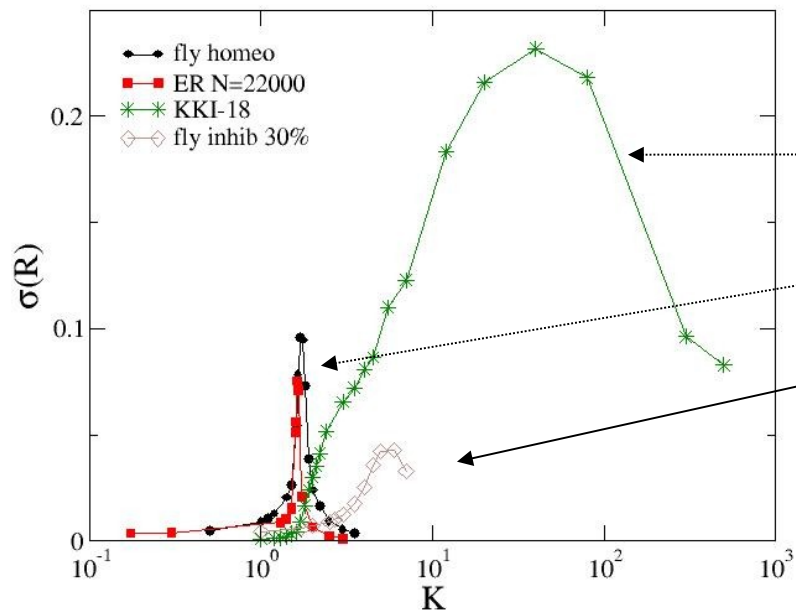
extended transition for KKI-18

For FF ~ ER like distro

With random inhibitors: wider range

The same is true for fluctuations of Ω





Fluctuations of R show

extended transition for KKI-18

For FF ~ ER like distro

With random inhibitors: wider range

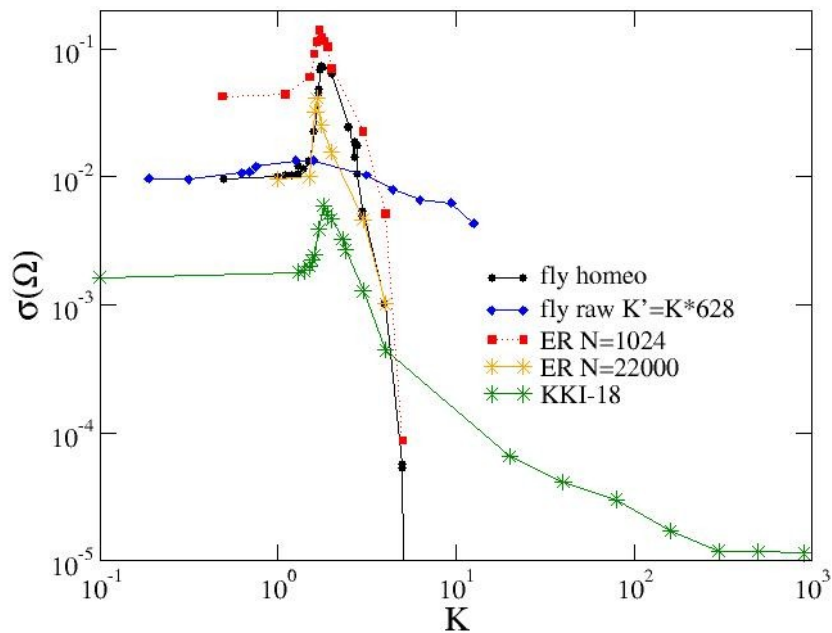
The same is true for fluctuations of Ω

HMN structure of KKI-18 is responsible

for the extended critical region

and Griffiths Phase of humans

As compared to the fly connectome



Synchronization transitions on connectome graphs with periodic external force (task state)

Synchronization transitions on connectome graphs with periodic external force (task state)

Shinomoto-Kuramoto oscillator model synchronization transition:

θ_i : angle, K : global coupling

Synchronization transitions on connectome graphs with periodic external force (task state)

Shinomoto-Kuramoto oscillator model synchronization transition:

$$\dot{\theta}_j(t) = \omega_j^0 + K \sum_k W_{jk} \sin[\theta_k(t) - \theta_j(t)] + F \sin(\theta_j(t)) + \epsilon \eta_j(t) .$$

θ_i : angle, K : global coupling
 F : external force, η_i : noise

Synchronization transitions on connectome graphs with periodic external force (task state)

Shinomoto-Kuramoto oscillator model synchronization transition:

$$\dot{\theta}_j(t) = \omega_j^0 + K \sum_k W_{jk} \sin[\theta_k(t) - \theta_j(t)] + F \sin(\theta_j(t)) + \epsilon \eta_j(t) .$$

θ_i : angle, K : global coupling
 F : external force, η_i : noise

Quenched heterogeneity in self-frequencies and network topology

Synchronization transitions on connectome graphs with periodic external force (task state)

Shinomoto-Kuramoto oscillator model synchronization transition:

$$\dot{\theta}_j(t) = \omega_j^0 + K \sum_k W_{jk} \sin[\theta_k(t) - \theta_j(t)] + F \sin(\theta_j(t)) + \epsilon \eta_j(t) .$$

θ_i : angle, K : global coupling
 F : external force, η_i : noise

Quenched heterogeneity in self-frequencies and network topology

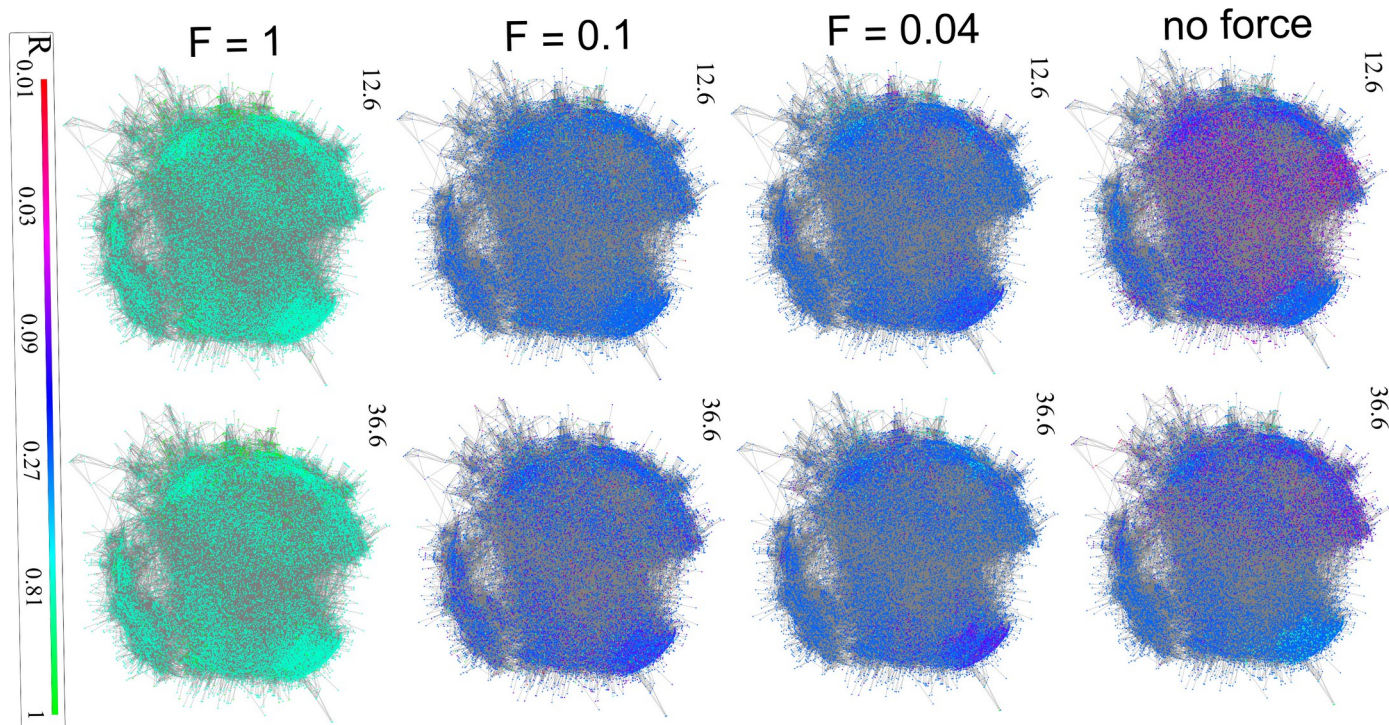
Synchronization transitions on connectome graphs with periodic external force (task state)

Shinomoto-Kuramoto oscillator model synchronization transition:

$$\dot{\theta}_j(t) = \omega_j^0 + K \sum_k W_{jk} \sin[\theta_k(t) - \theta_j(t)] + F \sin(\theta_j(t)) + \epsilon \eta_j(t) .$$

θ_i : angle, K : global coupling
 F : external force, η_i : noise

Quenched heterogeneity in self-frequencies and network topology



Force induced synchronization

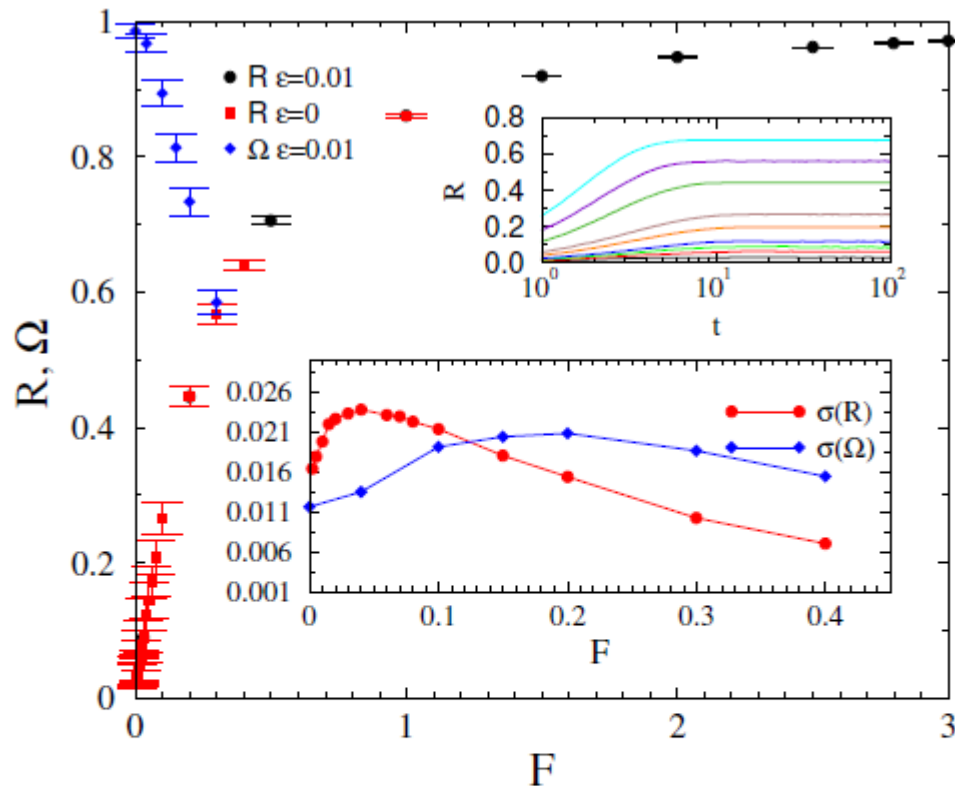


FIG. 1: Order parameter dependence on F for the fruit-fly connectome for the noisy (black bullet) and the noiseless (red boxes) cases at $K = 1.3$. The blue diamonds show the steady-state Ω values with noise. Lower inset: Variances of R and Ω for the noisy case. Upper inset: Time dependence of the noisy $R(t)$, for $F = 0, 0.02, 0.03, 0.04, 0.07, 0.1, 0.2, 0.3, 0.4$ (bottom to top curves).

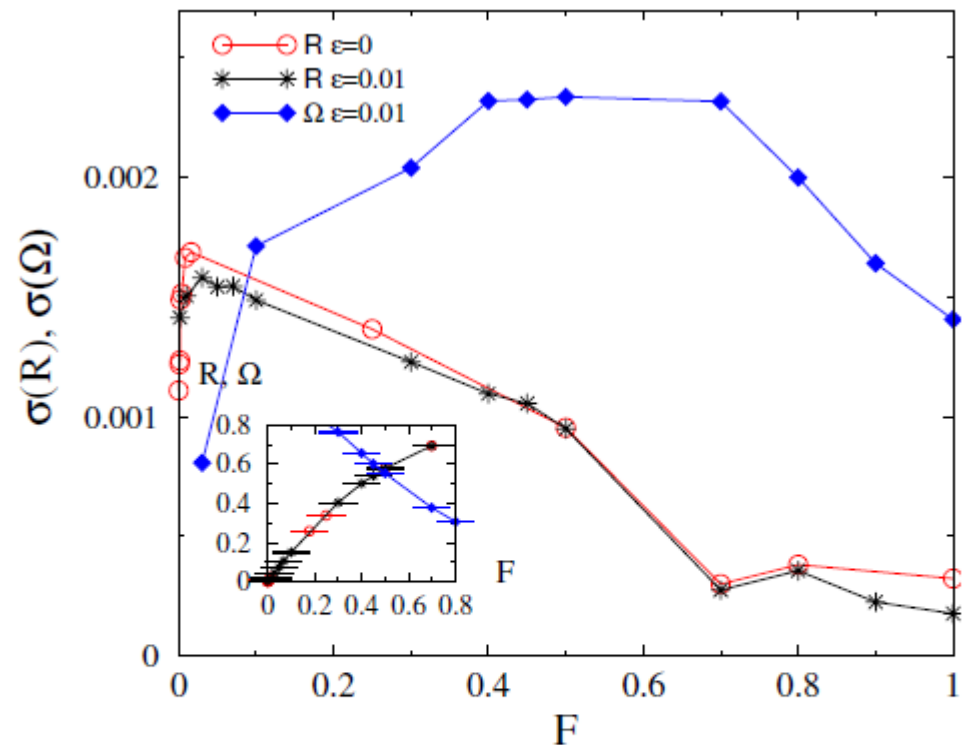
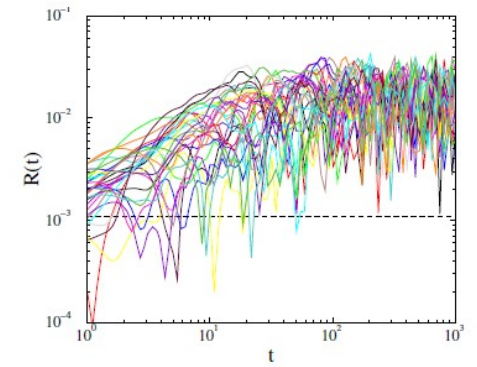


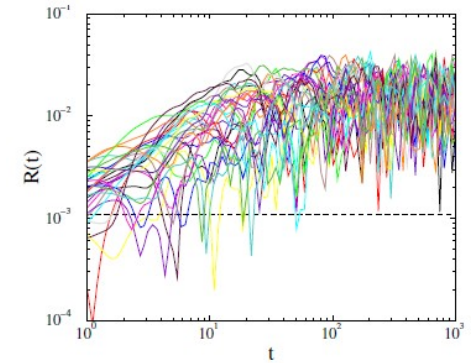
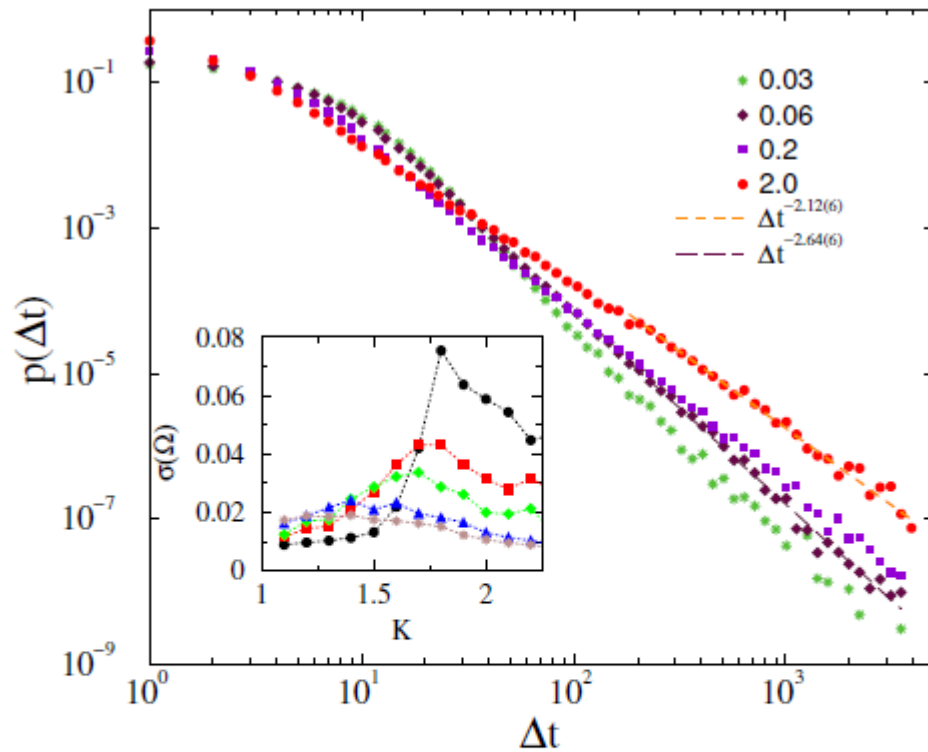
FIG. 3: Fluctuations of R and Ω as the function of F for the KKI-18, for the noisy and the noiseless cases at $K = 1$. Inset: Order parameter R for the noisy and noiseless cases as well as Ω , denoted by the same symbols as in the main figure.

Characteristic time exponent τ_t results

Characteristic time exponent τ_t results



Characteristic time exponent τ_t results



The $p(t_x)$ distros exhibit power-law near the synchronization transition point $F \sim 0.1$ for $K=1.3$ characterized by the exponent: 2

FIG. 4: Avalanche duration distributions on the fruit-fly connectome for different forces, shown by the legends and at $K = 1.3$, $\epsilon = 0.01$. Dashed lines are PL fits for $\Delta t > 100$. The inset shows the steady state $\sigma(\Omega)$ as the function of K , for excitation values $F = 0.001, 0.0667, 0.1, 0.2, 0.3$ (top to bottom).

Characteristic time exponent τ_t results

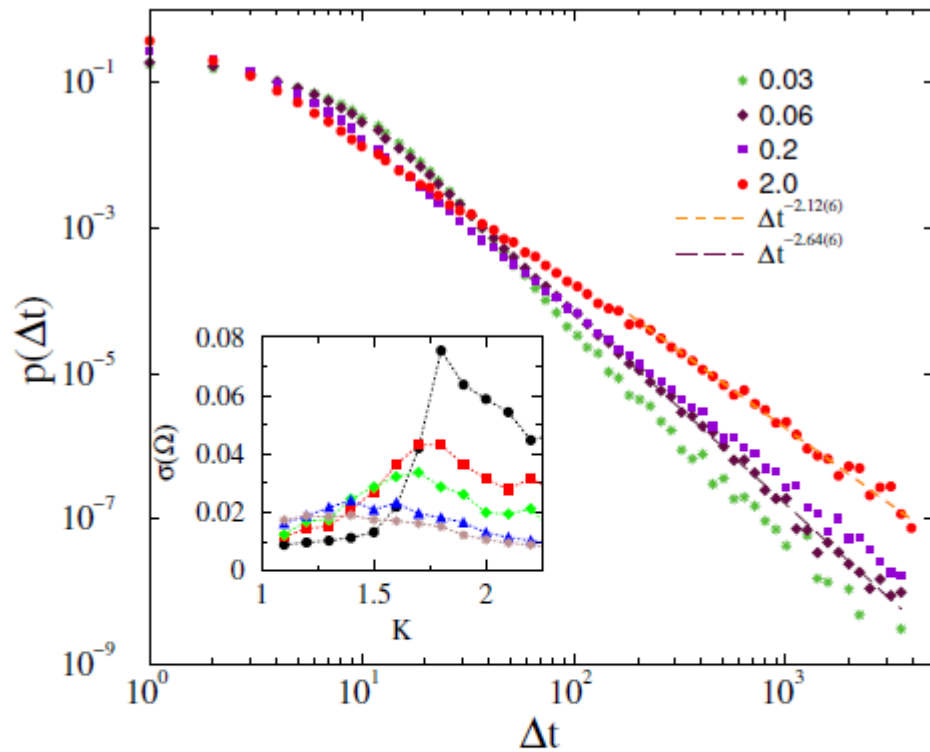
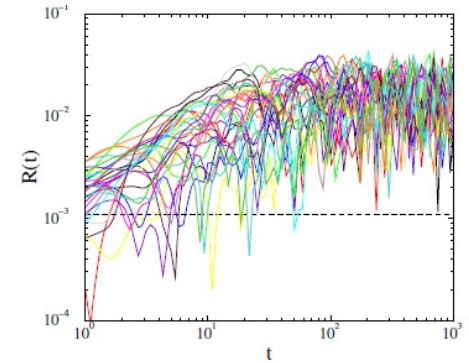
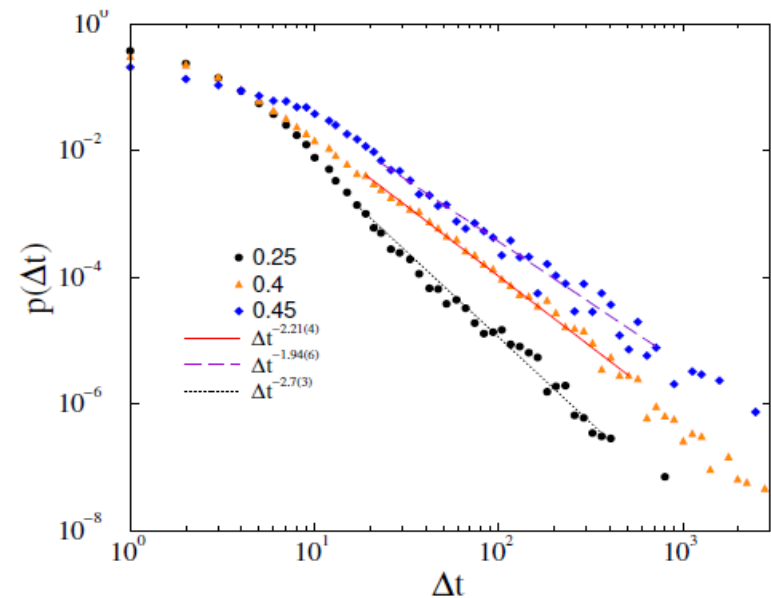


FIG. 4: Avalanche duration distributions on the fruit-fly connectome for different forces, shown by the legends and at $K = 1.3$, $\epsilon = 0.01$. Dashed lines are PL fits for $\Delta t > 100$. The inset shows the steady state $\sigma(\Omega)$ as the function of K , for excitation values $F = 0.001, 0.0667, 0.1, 0.2, 0.3$ (top to bottom).



The $p(t_x)$ distros exhibit power-law near the synchronization transition point $F \sim 0.1$ for $K=1.3$ characterized by the exponent: 2

Similarly as in case of the KKI-18:



Hurst and beta exponent analysis

Hurst and beta exponent analysis

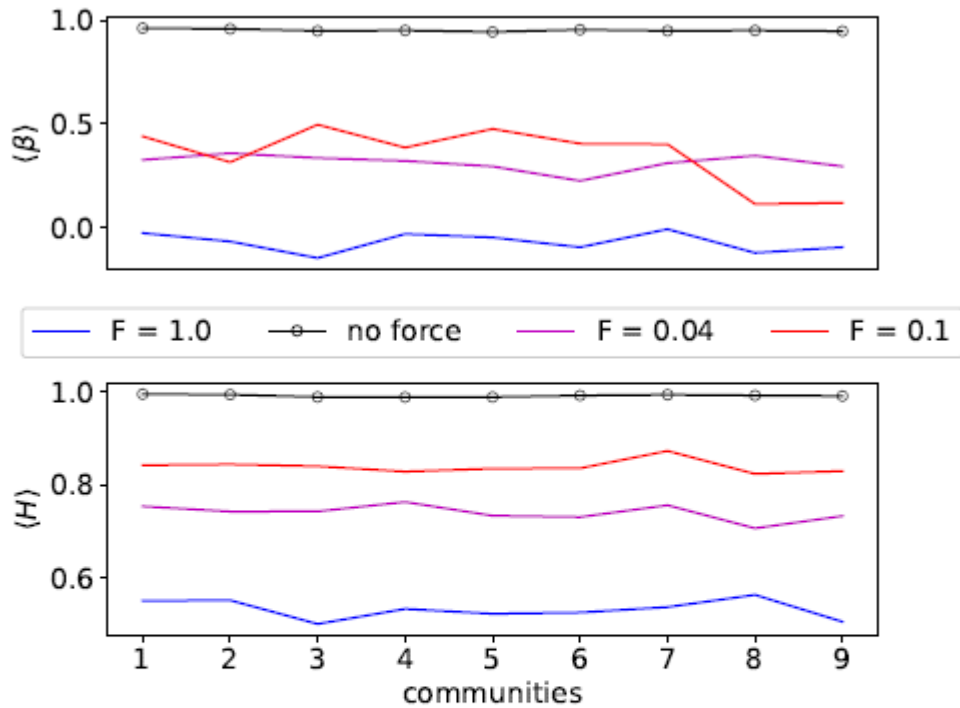


FIG. 8: Hurst and beta exponents of all fruit-fly connectome communities. In the forceless case at the critical Hopf transition coupling, the H exponent is the largest for every community. With forces these values drop for each community. This shows a resemblance with the rest and non-rest studies of different brain areas in [63], showing $\langle H \rangle \approx 1.0$ at resting state and $\langle H \rangle \approx 0.7$ at task driven states.

Hurst and beta exponent analysis

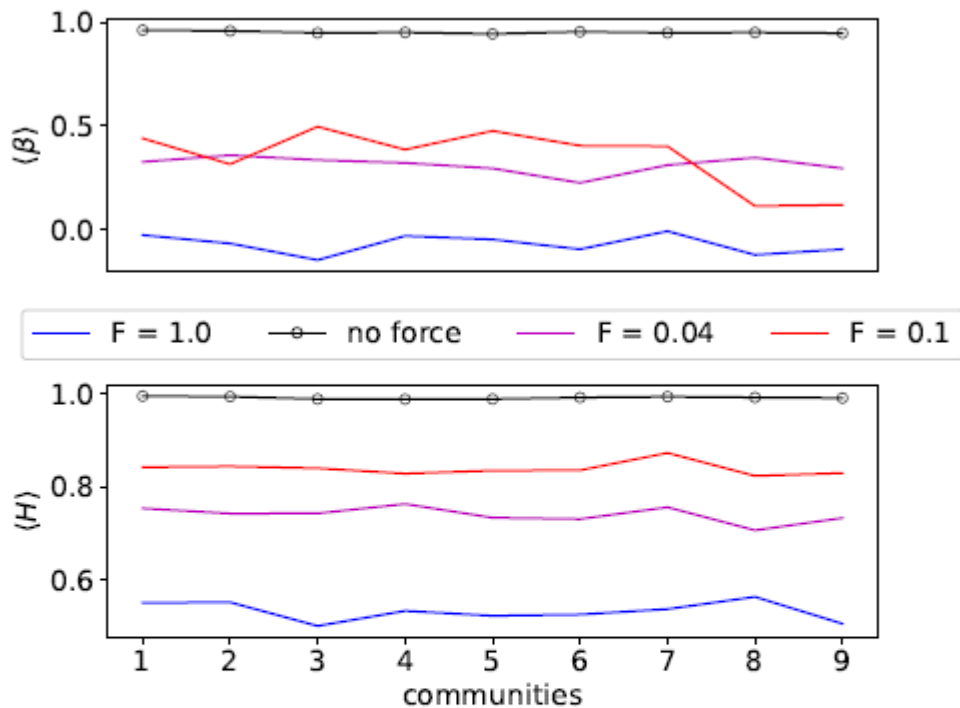


FIG. 8: Hurst and beta exponents of all fruit-fly connectome communities. In the forceless case at the critical Hopf transition coupling, the H exponent is the largest for every community. With forces these values drop for each community. This shows a resemblance with the rest and non-rest studies of different brain areas in [63], showing $\langle H \rangle \approx 1.0$ at resting state and $\langle H \rangle \approx 0.7$ at task driven states.

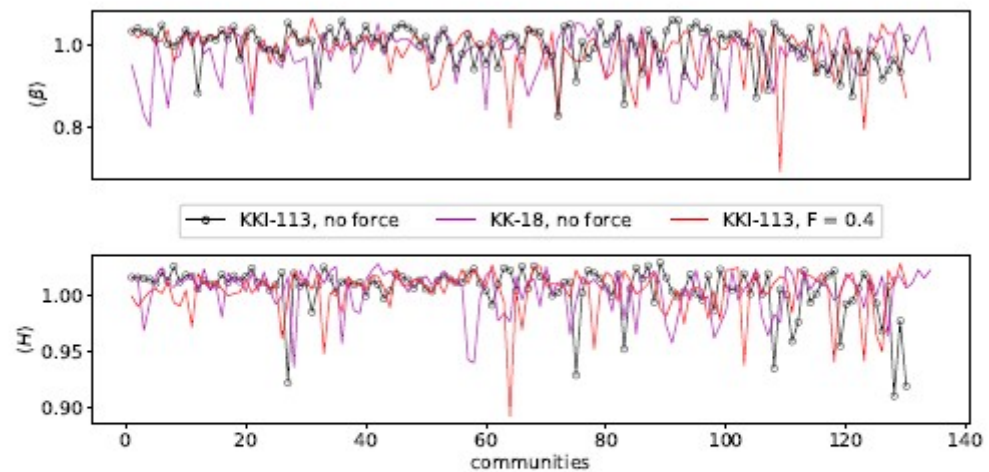


FIG. 9: Hurst and β exponents of all human connectomes' communities. KKI-113 is presented with and without force terms and KK-18 without the force terms.

Hurst and beta exponent analysis

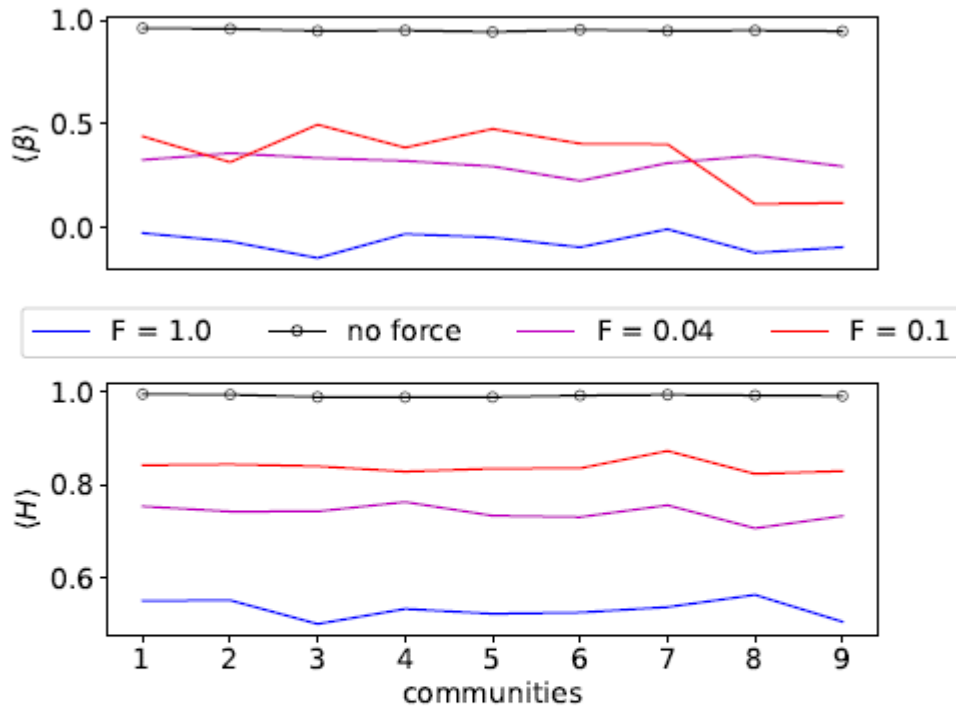


FIG. 8: Hurst and beta exponents of all fruit-fly connectome communities. In the forceless case at the critical Hopf transition coupling, the H exponent is the largest for every community. With forces these values drop for each community. This shows a resemblance with the rest and non-rest studies of different brain areas in [63], showing $\langle H \rangle \approx 1.0$ at resting state and $\langle H \rangle \approx 0.7$ at task driven states.

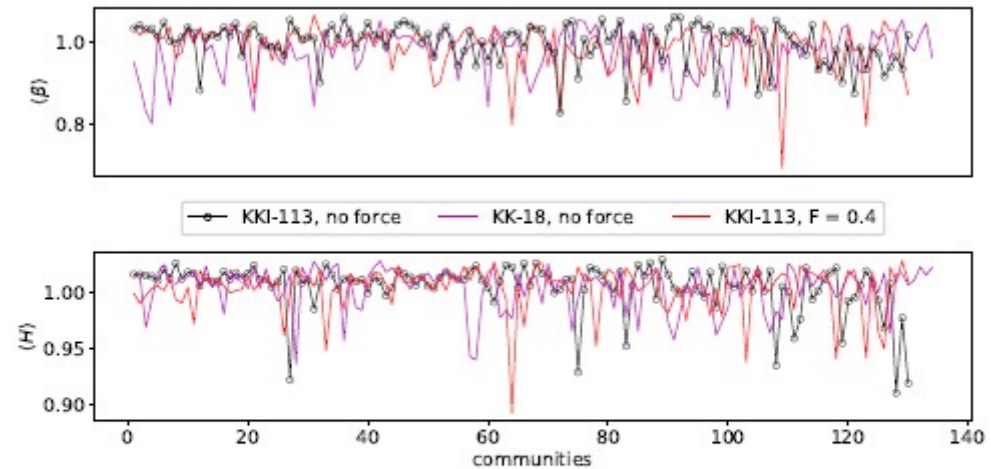
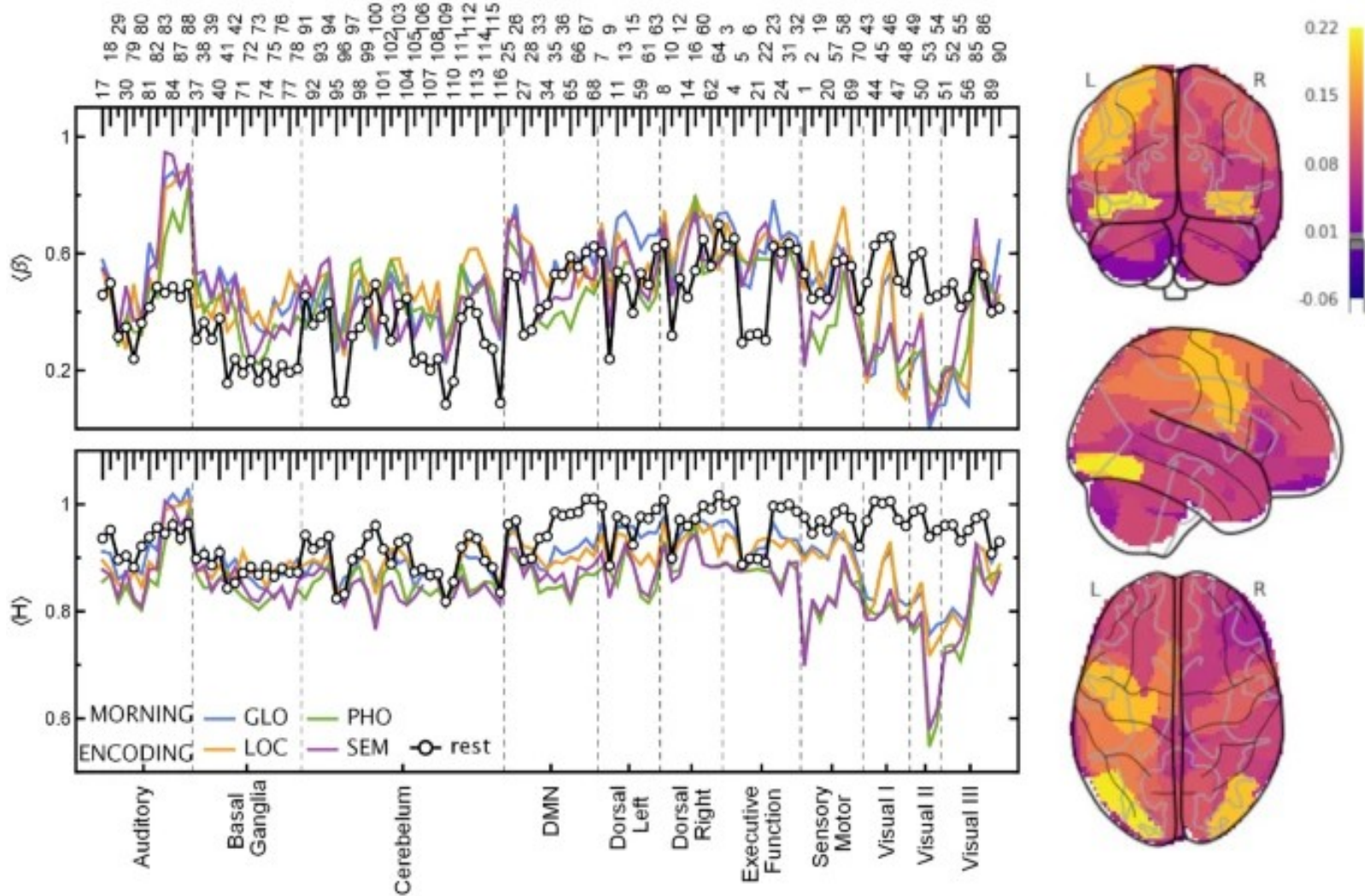


FIG. 9: Hurst and β exponents of all human connectomes' communities. KKI-113 is presented with and without force terms and KK-18 without the force terms.

Community dependent synch.
Quasi-criticality, like in fMRI
experiments: *Ochab et al,*
Sci. Rep. 12, 17866 (2022).

FMRI experiments



Task ↔ rest state operation

Conclusions

Conclusions

Heterogeneity effects on the scaling can be investigated on **large connectomes** and random small-world graphs for comparison

Conclusions

Heterogeneity effects on the scaling can be investigated on **large connectomes** and random small-world graphs for comparison

This enables to distinguish from finite size and rounding effects

Conclusions

Heterogeneity effects on the scaling can be investigated on **large connectomes** and random small-world graphs for comparison

This enables to distinguish from finite size and rounding effects

Large human graphs show: ~ degree distribution universality, finite dimensionality and small-worldness

Conclusions

Heterogeneity effects on the scaling can be investigated on **large connectomes** and random small-world graphs for comparison

This enables to distinguish from finite size and rounding effects

Large human graphs show: ~ degree distribution universality, finite dimensionality and small-worldness

In homeostatic threshold models dynamical critical behavior in the **GP**

Conclusions

Heterogeneity effects on the scaling can be investigated on **large connectomes** and random small-world graphs for comparison

This enables to distinguish from finite size and rounding effects

Large human graphs show: ~ degree distribution universality, finite dimensionality and small-worldness

In homeostatic threshold models dynamical critical behavior in the **GP**

Conclusions

Heterogeneity effects on the scaling can be investigated on **large connectomes** and random small-world graphs for comparison

This enables to distinguish from finite size and rounding effects

Large human graphs show: ~ degree distribution universality, finite dimensionality and small-worldness

In homeostatic threshold models dynamical critical behavior in the **GP**

Running Kuramoto model on **KKI-18** : crossover to synchronization

Conclusions

Heterogeneity effects on the scaling can be investigated on **large connectomes** and random small-world graphs for comparison

This enables to distinguish from finite size and rounding effects

Large human graphs show: ~ degree distribution universality, finite dimensionality and small-worldness

In homeostatic threshold models dynamical critical behavior in the **GP**

Running Kuramoto model on **KKI-18** : crossover to synchronization

Below the transition point **GP** like synchronization dynamics

Conclusions

Heterogeneity effects on the scaling can be investigated on **large connectomes** and random small-world graphs for comparison

This enables to distinguish from finite size and rounding effects

Large human graphs show: ~ degree distribution universality, finite dimensionality and small-worldness

In homeostatic threshold models dynamical critical behavior in the **GP**

Running Kuramoto model on **KKI-18** : crossover to synchronization

Below the transition point **GP** like synchronization dynamics

Durations, with exponents agreeing in vivo LRTC experiments for humans due to HMN and $d \sim 3.1 < 4$

Conclusions

Heterogeneity effects on the scaling can be investigated on **large connectomes** and random small-world graphs for comparison

This enables to distinguish from finite size and rounding effects

Large human graphs show: ~ **degree distribution universality, finite dimensionality and small-worldness**

In homeostatic threshold models dynamical critical behavior in the **GP**

Running Kuramoto model on **KKI-18** : crossover to synchronization

Below the transition point **GP** like synchronization dynamics

Durations, with exponents agreeing in vivo LRTC experiments for humans due to HMN and $d \sim 3.1 < 4$

Fruitfly: mean-field behavior ($d > 4$) and narrow fluctuation region

Conclusions

Heterogeneity effects on the scaling can be investigated on **large connectomes** and random small-world graphs for comparison

This enables to distinguish from finite size and rounding effects

Large human graphs show: ~ **degree distribution universality, finite dimensionality and small-worldness**

In homeostatic threshold models dynamical critical behavior in the **GP**

Running Kuramoto model on **KKI-18** : crossover to synchronization

Below the transition point **GP** like synchronization dynamics

Durations, with exponents agreeing in vivo LRTC experiments for humans due to HMN and $d \sim 3.1 < 4$

Fruitfly: mean-field behavior ($d > 4$) and narrow fluctuation region

Invariance with respect to frequency distributions

Conclusions

Heterogeneity effects on the scaling can be investigated on **large connectomes** and random small-world graphs for comparison

This enables to distinguish from finite size and rounding effects

Large human graphs show: ~ degree distribution universality, finite dimensionality and small-worldness

In homeostatic threshold models dynamical critical behavior in the **GP**

Running Kuramoto model on **KKI-18** : crossover to synchronization

Below the transition point **GP** like synchronization dynamics

Durations, with exponents agreeing in vivo LRTC experiments for humans due to HMN and $d \sim 3.1 < 4$

Fruitfly: mean-field behavior ($d > 4$) and narrow fluctuation region

Invariance with respect to frequency distributions

Insensitivity for the additive Gaussian noise

Conclusions

Heterogeneity effects on the scaling can be investigated on **large connectomes** and random small-world graphs for comparison

This enables to distinguish from finite size and rounding effects

Large human graphs show: ~ degree distribution universality, finite dimensionality and small-worldness

In homeostatic threshold models dynamical critical behavior in the **GP**

Running Kuramoto model on **KKI-18** : crossover to synchronization

Below the transition point **GP** like synchronization dynamics

Durations, with exponents agreeing in vivo LRTC experiments for humans due to HMN and $d \sim 3.1 < 4$

Fruitfly: mean-field behavior ($d > 4$) and narrow fluctuation region

Invariance with respect to frequency distributions

Insensitivity for the additive Gaussian noise

Conclusions

Heterogeneity effects on the scaling can be investigated on **large connectomes** and random small-world graphs for comparison

This enables to distinguish from finite size and rounding effects

Large human graphs show: ~ degree distribution universality, finite dimensionality and small-worldness

In homeostatic threshold models dynamical critical behavior in the **GP**

Running Kuramoto model on **KKI-18** : crossover to synchronization

Below the transition point **GP** like synchronization dynamics

Durations, with exponents agreeing in vivo LRTC experiments for humans due to HMN and $d \sim 3.1 < 4$

Fruitfly: mean-field behavior ($d > 4$) and narrow fluctuation region

Invariance with respect to frequency distributions

Insensitivity for the additive Gaussian noise

Periodic force induces synchronization and higher fluctuations

Force enhances long-range correlations, i.e. in the task phase operation of brain with respect to resting state

Summary

Summary

Thank you for your attention !

Recent publications:

Summary

Thank you for your attention !

Recent publications:

*Géza Ódor, Istvan Papp, Shengfeng Deng and Jeffrey Kelling :
Synchronization transitions on connectome graphs with external force
Front. Phys. 11 (2023) 1150246.*

*Géza Ódor, Gustavo Deco and Jeffrey Kelling
Differences in the critical dynamics underlying the human and fruit-fly connectome
Phys. Rev. Res. 4 (2022) 023057.*

Summary

Thank you for your attention !

Recent publications:

*Géza Ódor, Istvan Papp, Shengfeng Deng and Jeffrey Kelling :
Synchronization transitions on connectome graphs with external force
Front. Phys. 11 (2023) 1150246.*

*Géza Ódor, Gustavo Deco and Jeffrey Kelling
Differences in the critical dynamics underlying the human and fruit-fly connectome
Phys. Rev. Res. 4 (2022) 023057.*